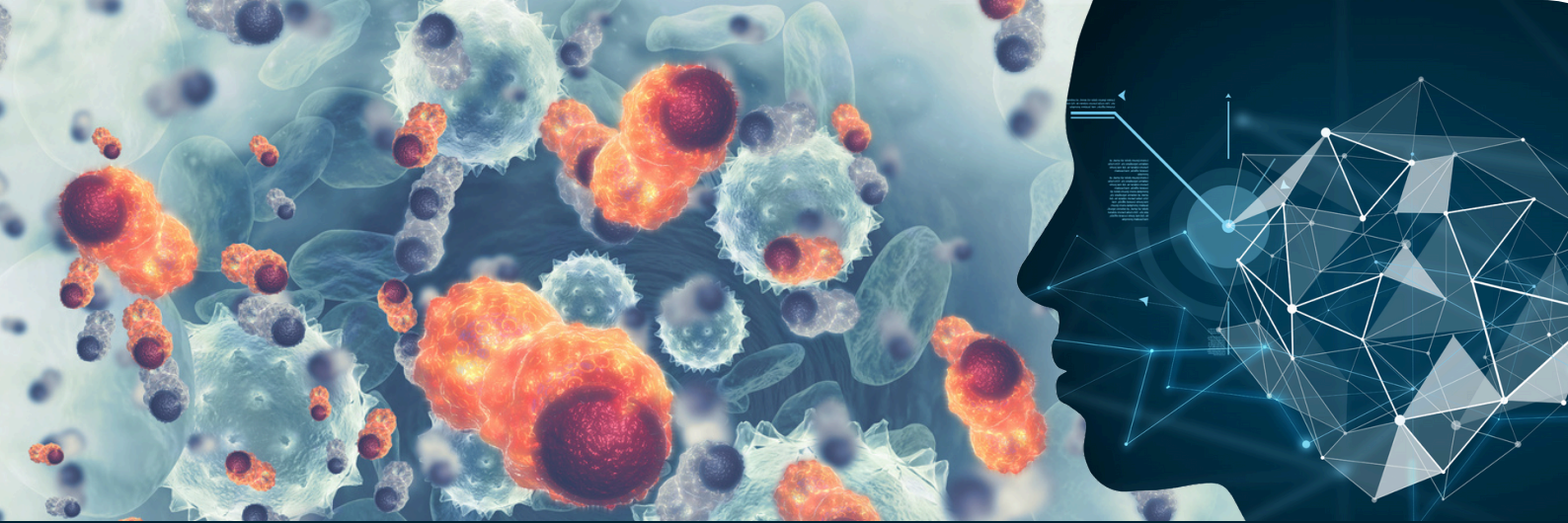




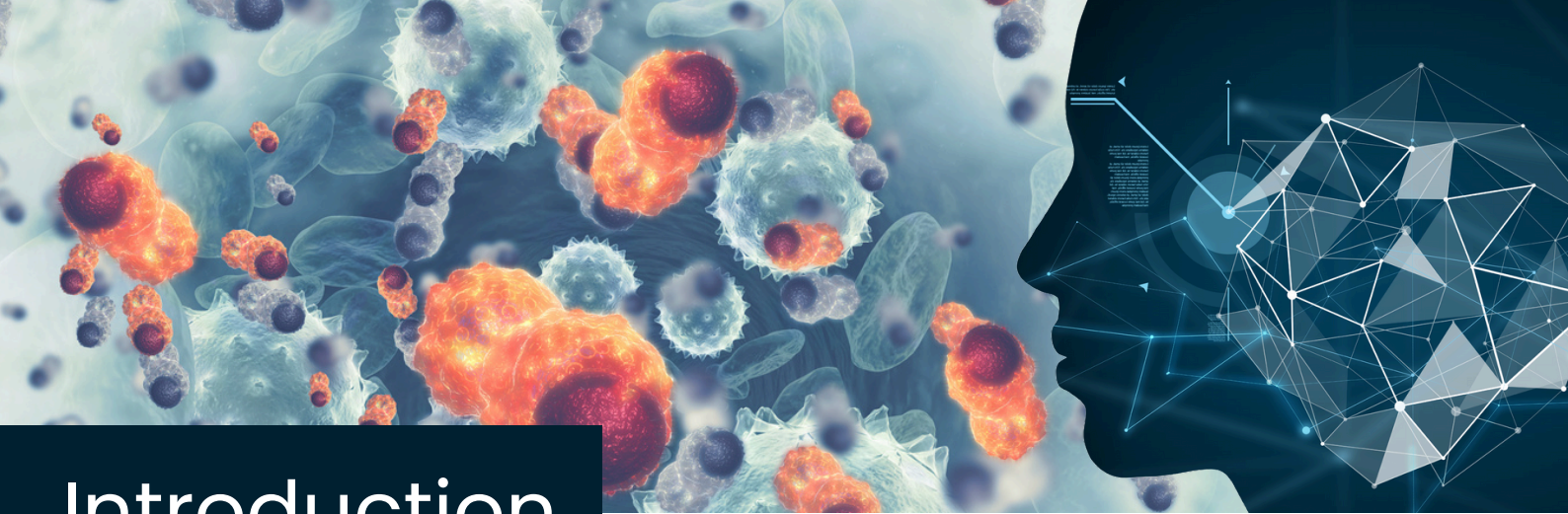
Simplifying the future: AI and machine learning in live-cell image analysis



Simplifying the future: AI and machine learning in live-cell image analysis

CONTENTS

- **Introduction**
- **Report:** MSCProfiler: A single cell image processing workflow to investigate mesenchymal stem cell heterogeneity
- **Application Note:** AI-driven label-free quantification of cell viability using live-cell analysis
- **Research Article:** High-resolution visualization and assessment of basal and OXPPOS-induced mitophagy in H9c2 cardiomyoblasts
- **Research Article:** Image analysis workflows to reveal the spatial organization of cell nuclei and chromosomes
- **Application Note:** Cell-based phenotypic screening with Incucyte® Live-Cell Analysis Systems



Introduction

Live-cell imaging is a key technique in cell biology, offering insights essential to our understanding of disease and the development of therapeutics. However, analyzing and interpreting acquired data can prove difficult due to its complexity and multidimensionality.

The recent focus on integrating live-cell imaging and machine learning tools has been an exciting step in streamlining the analysis workflow. Artificial Intelligence (AI)-driven methods are able to recognize patterns in data that cannot be identified by the human eye, enabling interrogation of complex data quickly and objectively to make it more accessible for researchers to interpret.

In this eBook, we highlight how AI and machine learning have been implemented to make live-cell image analysis more efficient for quantifying cell viability, investigating mesenchymal stem cell heterogeneity and assessing subcellular features.



Beatrice Bowlby
Digital Editor
BioTechniques
Beatrice.Bowlby@tandf.co.uk

MSCProfiler: a single cell image processing workflow to investigate mesenchymal stem cell heterogeneity

Ayona Gupta¹ , Safia Kousar Shaik², Lakshmi Balasubramanian³ & Uttara Chakraborty*¹ 

¹Manipal Institute of Regenerative Medicine, Bengaluru, Manipal Academy of Higher Education, Manipal, Karnataka, 576104, India; ²Delft University of Technology, Delft, The Netherlands; ³SaviTix Technology Consultancy, Bengaluru, India; *Author for correspondence: uttara.chakraborty@manipal.edu

BioTechniques 75: 195–209 (November 2023) 10.2144/btn-2023-0048

First draft submitted: 18 June 2023; Accepted for publication: 28 September 2023; Published online: 2 November 2023

ABSTRACT

Single cell cytometry has demonstrated plausible immuno-heterogeneity of mesenchymal stem cells (MSCs) owing to their multivariate stromal origin. To contribute successfully to next-generation stem cell therapeutics, a deeper understanding of their cellular morphology and immunophenotype is important. In this study, the authors describe MSCProfiler, an image analysis pipeline developed using CellProfiler software. This workflow can extract geometrical and texture features such as shape, size, eccentricity and entropy, along with intensity values of the surface markers from multiple single cell images obtained using imaging flow cytometry. This screening pipeline can be used to analyze geometrical and texture features of all types of MSCs across different passages hallmarked by enhanced feature extraction potential from brightfield and fluorescent images of the cells.

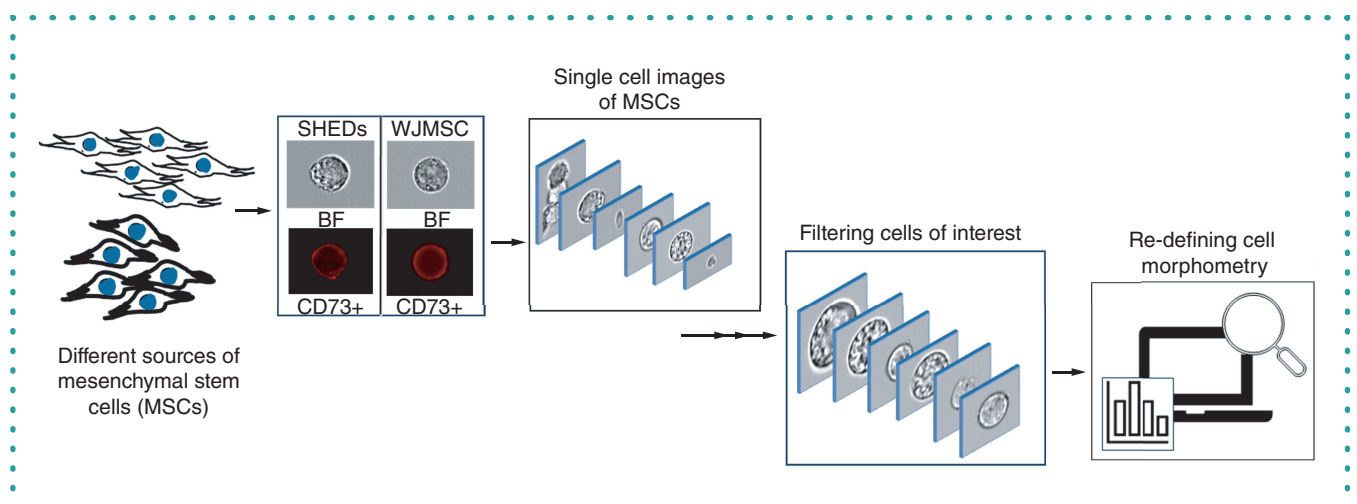
METHOD SUMMARY

This study describes the development of an enhanced image feature extraction approach to analyze single cell image data of mesenchymal stem cells (MSCs). MSCProfiler, an automated image analysis pipeline, was developed using CellProfiler software to analyze geometrical and morphological/texture features and fluorescence intensities of biomarkers in MSCs across passages and tissue sources. Compared to existing image analysis tools, this workflow is devoid of human bias and is marked by the efficiency with which it filters out nontarget images and extracts features from brightfield and fluorescent images of cells.

TWEETABLE ABSTRACT

Mesenchymal stem cells are known for their cellular heterogeneity, which requires deeper understanding to contribute stem cell therapeutics. MSCProfiler is an automated, single-cell image-processing workflow that sheds light on MSC heterogeneity.

GRAPHICAL ABSTRACT



KEYWORDS:

biomarkers • CellProfiler • image data analysis • imaging flow cytometry • immuno-heterogeneity • mesenchymal stem cells • single cell cytometry • software

At the forefront of cell-based therapies are mesenchymal stem cells (MSCs), with over 1000 registered clinical studies under way [1]. These are adult tissue-derived multipotent stem cells, which can be isolated from almost all postnatal organs and tissues [2]. They have a variety of pleiotropic functions such as antiapoptosis, angiogenesis, antifibrosis and chemo-attractive properties, making them a useful tool for a wide variety of therapeutic applications [1,3,4]. An important metric to qualify MSCs as beneficial therapeutic agents is the determination of their safety and risks, if any [4]. Consequently, culturing and studying these cells become important. However, one of the hurdles faced in the translation of *in vitro* MSC studies is that many of the properties that are studied, especially expression of surface proteins, arise because of the artificial culture environment [5]. Expression of surface markers such as CD90, CD73, CD105 and CD44, which are routinely used for MSC characterization, are limited to only being expressed *in vitro* and not *in situ*. A major challenge in the translation of MSCs to clinical application is the inherent heterogeneity of MSCs, which influences its properties of immunomodulation and regeneration [3]. The heterogeneity, arising due to isolation, culture and expansion, warrants an extensive study on various MSC subtypes and their categorization [3,6].

To understand this heterogeneity, a cell-by-cell approach as opposed to conducting studies at a population level would be more advantageous in revealing important and unique properties of various cell types [7]. In this context, single cell analysis platforms such as imaging flow cytometry (IFC) can prove to be a powerful tool. An amalgamation of high-throughput cytometry and microscopy, IFC allows extraction of traditional flow cytometric data and images of each event from fluorescent, brightfield (BF) and laser side scatter/darkfield (DF) channels [8]. The potential of this technology has mostly allowed the exploration of nuclear translocation [9], autophagy [10,11] and detection of DNA damage [12–14]. However, unraveling the immuno-heterogeneity of cells using this technology is still under way. The high-throughput nature of this technology allows the collection of enormous amounts of data from a single cell, which can be used to answer questions of cellular heterogeneity [8] and holds immense potential for data mining and creating well-trained neural networks. However, a large amount of information remains underutilized to a great extent due to the lack of data analysis tools that can extract meaningful information from the images [9].

In this study, we have used the Amnis ImageStream image cytometer which is one of the widely used IFC instruments. Data analysis on Amnis platforms can be done using their proprietary software IDEAS or with analysis tools such as FCS Express (DeNovo Software). Apart from having the advantage of performing traditional flow cytometry data analysis, the IDEAS platform also provides users with 'wizards', which provide assay-specific analysis templates for feature finder, enabling sequential analysis without many complications (<https://cytekbio.com/pages/imagestream>). In addition, specific areas or regions of the cell image can be defined using a 'mask' (defined set of pixels in the region of interest) that contain features such as creating nuclear masks or cell surface marker-specific masks. It is also possible to create the masks on IDEAS based on user-defined criteria. This can be done by using the mask manager, which has 13 available functions to create the new mask. However, use of this analytical software is primarily dependent on the experience of the user and therefore brings in bias. This can especially be challenging when understanding immuno-heterogeneity, which can lead to missing out on potentially important features if one does not actively look for them.

The recent trend in the incorporation of machine learning (ML) or artificial intelligence in biology has resulted in the advancement of data analysis approaches [15]. Use of virtual or label-free staining of cells [16,17], use of BF information alone to extract quantitative features of cells [16] and use of ML to analyze IFC data for diagnostics [18] have all introduced a new paradigm. However, some of these methods might require an in-depth knowledge of deep-learning techniques, neural networks or programming languages [19]. In this study, the authors used a user-friendly, freely available software, CellProfiler (available at <https://cellprofiler.org/>), to create a pipeline that can be used to analyze most of the commonly available image file formats [20].

Here the authors introduce MSCProfiler, a completely automated workflow, to analyze IFC data from different human MSCs such as the stem cells of human exfoliated deciduous teeth (SHEDs) and Wharton's jelly-derived MSCs (WJMSCs). The authors developed the entire workflow using the SHEDs and tested the robustness of the same using WJMSCs. SHEDs were stained with antibodies that recognize surface antigens of these cells, prescribed as minimal criteria for identification of MSCs by the International Society for Cell & Gene Therapy (ISCT) [21]. The authors included two surface markers in their studies: CD44/homing cell adhesion molecule and CD73/ecto-5'-nucleotidase. Conventionally, with routine flow cytometry-based characterization of MSCs, bivariate plots of CD44 and CD73 should represent $\geq 95\%$ double-positive population (refer to Supplementary Figure 1) to suffice the criteria of MSCs as per ISCT guidelines and should express $\leq 2\%$ hematopoietic marker CD45 [21]. In the authors' panel, they used the above markers and included SYTOX Green as a live/dead discriminator. Live cells exclude SYTOX Green from their membranes, whereas the nucleus of dying/dead cells whose membrane integrity has been compromised take up the dye [22]. The authors focused on the extraction of feature information from individual BF and/or fluorescent images acquired on the Amnis ImageStream Mk II instrument. This workflow can identify images of live singlets based on the exact boundary of single cells from doublets or aggregates and compute the geometrical parameters such as

Table 1. Sample preparation guide.

Tube	Reagent mix	Total volume of antibody added (3 μ l each antibody per 1×10^6 cells)	Total volume of cells added	Total volume of staining buffer added	Final volume
1	CD44 + CD73 + CD45 + SYTOX Green	9 μ l	50 μ l	41 μ l	100 μ l
2	CD44 (single color control)	3 μ l		47 μ l	
3	CD73 (single color control)	3 μ l		47 μ l	
4	CD45 (single color control)	3 μ l		47 μ l	
5	SYTOX Green (single color control)	Nil.		50 μ l	

area, aspect ratio, eccentricity, compactness and even texture features such as, inverse difference moment and entropy. The intensity of CD44 and CD73 antigens were also extracted from the fluorescent channel images and their surface distribution pattern was observed.

Materials & methods

Cell culture

Individual cell cultures of SHEDs at passage 9 (P9) and 12 (P12) and WJMSCs at P6 were maintained for this study. Each cell type were seeded in 100 mm culture dishes at a density of 5000 per cm^2 and grown in KnockOut Dulbecco's modified Eagle medium (Gibco) media supplemented with 10% fetal bovine serum (Gibco), $1 \times$ Pen-Strep (Gibco) and $1 \times$ glutamine (Gibco) and grown at 37°C (humidity conditions) until they reached 90–95% confluency with media changes every 24 or 48 h as required. Cells were then washed once with plain basal media without any supplements and trypsinization was done by adding 0.25% trypsin-EDTA (Gibco) followed by incubation at 37°C for 10 min until all the cells had detached from the culture dish. Trypsin-EDTA was neutralized with basal media and the cells were collected and centrifuged at 1200 r.p.m. for 6 min to obtain the cell pellet.

Preparation of cell suspension for immunostaining

The cell pellet was resuspended in 1 ml media, and the cell count was determined. Cells were then washed twice with staining buffer (2% fetal bovine serum in phosphate-buffered saline). Two percent fetal bovine serum helps to sustain viable cells while in suspension post-trypsinization. A cell suspension of 1×10^6 cells per 50 μ l suspension contributed to 100 μ l of reaction volume when mixed with antibodies and staining buffer. The amount of antibody added to every tube is described in Table 1.

Antibodies & immunostaining

Live SHEDs were simultaneously stained for three surface antigens with an antibody cocktail consisting of CD44, CD73 and CD45. The list of antibody–fluorochrome conjugates are provided in Supplementary Table 1. Cells were incubated for 30 min, washed twice with staining buffer and finally resuspended in 100 μ l of staining buffer. Prior to data acquisition, SYTOX Green ($1 \times$) was added to Tubes 1 and 5 (Table 1) and incubated at 37°C for 15 min. SYTOX Green is a nucleic acid stain/dye which helps discriminate between live and dead cells.

To address the biggest concern of spectral spillage in a multicolor immunophenotyping experiment, we prepared the right controls for compensation. The single color controls for every antibody used including the DNA binding dye were prepared. Using the compensation algorithm, the noBF files were generated while acquiring the single color tubes. Cells were stained for all the single color compensation controls. Since MSCs would not express CD45, cells from peripheral blood were used as single color controls. For the viability dye, SYTOX Green, compensation control was prepared by giving heat shock treatment to MSCs at 70°C for 5 min followed by incubation on ice. Table 1 summarized the reaction mix per tube, using 1×10^6 cells/ml cell density.

Acquisition on the Amnis ImageStream Mk II

Cells were acquired on the IFC platform Amnis ImageStream Mk II equipped with one charged couple device (CCD) camera (six channels/detectors) using INSPIRE acquisition software, briefly described in Figure 1A. The detection channels available for use in the instrument based on the fluorochrome conjugates were V450 (Channel 1, 435–505 nm), SYTOX Green (Channel 2, 505–560 nm), phycoerythrin (PE; Channel 3, 560–595 nm), BF images (Channel 4, 595–642 nm), Peridinin Chlorophyll Protein-Cyanine 5.5 (PerCP-Cy5.5) (Channel 5, 642–745 nm), and DF images/ side scatter (Channel 6, 745–780 nm). The instrument configuration and panel design are provided in Supplementary Table 2. Unstained cells were first run to set the baseline correction by adjusting the laser powers such that no autofluorescence could be detected. Lasers were set at 10 mW for 405 nm laser (Channel 1 excitation) and 10 mW for 488 nm laser (Channel 2, 3 and 5 excitation). Sample tubes containing all four colors were run and $\geq 1,00,000$ events were acquired. All the single color tubes were run with the BF and DF parameters turned off and were automatically saved with 'noBF' mentioned in their file names. These files were later used to set up the compensation matrix postacquisition. All raw data files were saved in raw image file (.rif) format.

Setting up compensation on IDEAS

As opposed to conventional flow cytometry which relies on voltage gain of individual photomultiplier tubes to collect a signal generated from antibody fluorochrome conjugate, the detectors available on the Amnis ImageStream Mk II are charged couple devices. They

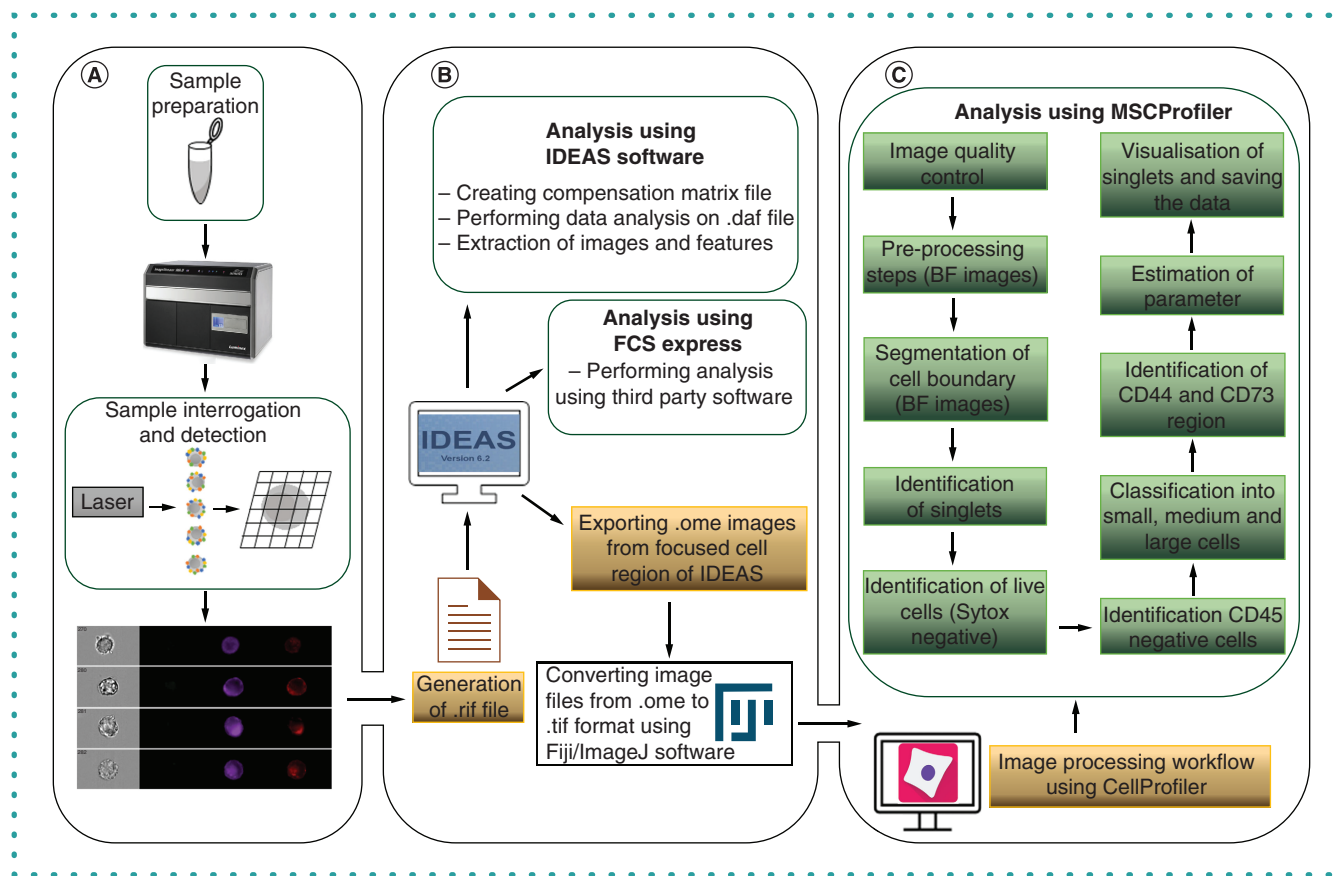


Figure 1. Supervised versus automated data analytical tools. (A) Sample preparation and acquisition on the imaging flow cytometer using INSPIRE software, which generated the single cell images of each cell in flow. (B) Supervised analytical software IDEAS v6.2 was used to create a compensation matrix and .daf and .cif files to analyze the acquired data and view the cell images. Data analysis software such as FCS Express v6 was used to analyze the cytometry data. (C) MSCProfiler analytical automated pipeline. Images exported from IDEAS were converted to .tif format and later uploaded on MSCProfiler and run through the workflow to extract information from the single cell images and identify cells of interest.

have a higher quantum efficiency than photomultiplier tubes, which make them ideal detectors to collect dim fluorescence signals, a prerequisite for good imaging. On this instrument, a pixel-based compensation is performed postacquisition using IDEAS software. The 'noBF' files of each color acquired in .rif format were loaded onto IDEAS software to create a compensation matrix to correct the spectral spillage of fluorochromes in respective channels. Once the compensation matrix was set up, they were saved in compensation matrix (.ctm) file format.

IFC data analysis

The IFC data have two components – first, the flow cytometric data conventionally represented by dot plots and, second, the individual images of each dot on the plot. As a comparative study, the IFC data were analyzed using both IDEAS and FCS Express software. The data analysis was performed using the proprietary software IDEAS v6.2 (Amnis Corp., WA, USA). Following hierarchical gating, the population of interest was first identified, after which the image data analysis began. Every cell was demarcated with a number and was visible on the screen/image gallery. 'noBF' files were used to set up the compensation matrix. The .rif and .ctm files were then used to create the data analysis file (.daf) and compensated image file (.cif). The downstream analysis was performed using the .daf files. Following a hierarchical gating strategy, first the focused cells were identified by plotting a histogram of normalized frequency versus gradient root mean square value of Channel 4 (BF). This was followed by single cell identification (selected apart from the aggregates/debris) gated from the aspect ratio of Channel 4 versus area of Channel 4. The next plot was to identify live cells (negative for SYTOX) from the Channel 6 (DF) versus Channel 2 plot, followed by CD45 negative cells from the Channel 6 (DF) versus Channel 3 (CD45) plot (exclusion gating strategy), and finally populations positive for both CD44 and CD73 were identified from a bivariate plot between Channel 1 (CD44) and Channel 5 (CD73).

Analysis using FCS Express

The .daf file was read by FCS Express v6 (Research Use Only), flow cytometry data analysis software. It was ensured that both the .daf file and the .cif file for each sample tube were available in the same analysis folder. Using a gating strategy similar to that described in the preceding section, singlets were identified first, followed by live cells. The CD45 negative cells were first identified and gated onto the next plot to show the CD44 and CD73 double positive cells. This software validated the gating strategy applied to the populations before proceeding with single cell image data analysis. A flowchart of the steps involved in supervised analysis platforms are shown in Figure 1B.

Preparing images for CellProfiler analysis

The individual images from Channels 1, 2, 3, 4 and 5 were selected from Export .tif images under the Tools option on IDEAS. The images come with an open microscopy environment (.ome) extension, which were converted to .tiff using Fiji/ImageJ software in an automated fashion using an in-house-built macro (Supplementary Information). These individual images were used in the image processing workflow as described in the later sections, to extract the single cellular features. The workflow was developed using CellProfiler software to analyze the single cell images of MSCs.

MSCProfiler workflow

The individual .tiff images of all the channels were then loaded into the MSCProfiler pipeline through the input modules (features that perform specific tasks). Using the NamesAndTypes module, each channel image was categorized in a way that a singlet set consisted of information on a single cell/event consisting of BF and fluorescent channel images. The automated pipeline was described by broadly classifying them into 11 steps based on the purpose they serve. Individual cell information (i.e., information from all five channels) was processed through all the modules of each component to identify and extract various features such as geometric, texture and intensity values, described in Figure 1C. To begin with, the total number of cells analyzed was 54,356 (SHEDs P9), which were selected from the 'focused' cell gate on the IDEAS software. Therefore, a total of 271,780 images, collected from all five channels, were run on MSCProfiler. All 271,780 images were not run through the workflow at one time. The total set was divided into 24 groups, each containing approximately 10,000 images. In order to evaluate the strength of the workflow, roughly 13,000 and 10,000 each of WJMSC (P6) and SHEDs (P12), respectively, were analyzed as well. The steps in the MSCProfiler workflow are as follows:

1. Quality control of images – the MeasureImageIntensity and FlagImage modules were used to discard images that did not contain any cellular information. The MeasureImageIntensity module calculated the intensity measurements of the images based on which the boundary conditions were set in the FlagImage module to discard the poor-quality images. Only BF (Channel 4) images were used for this quality check to estimate if the image had any cellular information or not. Those BF images whose total image intensity was in the range of 5500–7900 pixels and whose total image area was in the range of 9000–13,000 pixels were best fit to proceed. The images that did not satisfy the criteria were discarded/flagged from the analysis.
2. Preprocessing steps – the unflagged image set was then used for further analysis. To identify the cellular region, BF images were used. Each of the BF images were preprocessed using four modules: ImageMath, Smooth, RescaleIntensity and EnhanceEdges. The ImageMath module was used for subtraction of the foreground from the background of the BF images. The Smooth module applied the Gaussian filter on the BF images to blur the pixels outside the cell and highlight the pixels inside the cell. The RescaleIntensity module found the minimum and maximum intensity values across the entire BF image and rescaled every pixel, so that the minimum intensity value was zero and the maximum intensity value was one. The EnhanceEdges module made use of the Sobel filter method to highlight the edges of the cell identified in the BF image.
3. Segmentation of cell boundary – the preprocessed BF images resulting from the above-mentioned steps were used to identify the cell boundary. This section of the workflow involved four modules. First, the threshold module was used to identify the pixels of interest based on the gray scale signal using Otsu thresholding, a method based on the signal variances between the foreground and the background. Second, the Morph module removed the identified pixels from the background of the segmented image. Third, the IdentifyPrimaryObjects module identified cell boundary. Finally, the ExpandOrShrinkObjects module was added to get a more accurate cellular boundary. The BF images that contained one cell per image proceeded for further processing, while those that contained more than one cell per image were discarded by the FlagImage module.
4. Identification of singlets – this section of the workflow contained three modules, which were used to identify only the singlet MSCs and remove the images that contained more than one cell. The MeasureObjectSizeShape module calculated geometrical features, such as Area, FormFactor, Compactness and Eccentricity, of the cell identified from the BF image. A boundary condition was set up on the Area, FormFactor and Eccentricity measurements in the FilterObjects module to obtain the singlets. Eccentricity describes the deviation of a shape/object is from circularity, for a circle it is equal to 0. Compactness gives an idea whether an object has holes (or missing pixels) in it or is a close bound figure; a circle has a compactness of 1. Aspect ratio (minimum ferret diameter/maximum ferret diameter) defines how elongated an object is; for a perfectly circular object, it is equal to 1. For the identified cell to be a singlet, its Area was set in the range of 150–4500 pixels, its FormFactor lay in the range of 0.75–1.0 pixels and its Eccentricity value was in the range of 0.0–0.7 pixels. If the identified cell did not meet this criterion, the BF image was considered a nonsinglet and was discarded.

- by the FlagImage module. The ranges specified in individual modules were set by first taking a set of 50–100 cell images that had a mix of target and nontarget cells and were measured during the pipeline building steps.
5. Identification of live singlets – this part of the workflow confirmed an identified singlet as a live or a dead cell based on the appropriate marker using the following five modules: RescaleIntensity, MeasureObjectIntensity, FilterObjects, MeasureImageIntensity and FlagImage modules. These modules sequentially called for the SYTOX channel images (Channel 2) of the identified singlet. For a singlet to be a live singlet, the mean intensity value of the SYTOX channel was set to 0 pixels. Therefore, such cells with no signal in the SYTOX channel were the live cells. Detection of signal/intensity from the SYTOX channel marked the cell as a dead cell and hence it was discarded.
 6. Identification of CD45 negative population – this section of the workflow checked that the MSCs were negative for CD45 expression (tagged to PE) as one of the first criteria to identify them. The RescaleIntensity, MeasureObjectIntensity, FilterObjects, MeasureImageIntensity and FlagImage modules were again sequentially called for the PE channel (Channel 3) images of the identified live singlets to confirm that the cells were PE negative. The mean intensity values of the images from PE channel was set in the range 0–0.002 pixels.
 7. Classification of singlets into large, medium and small MSCs – the identified singlets of MSCs were categorized as small, medium and large cells based on their area and this was performed using the FilterObjects module. The small, medium and large MSC singlet classification was based on the area criteria set within the ranges of 2200–3000, 3001–4000 and 4001–4500 pixels, respectively.
 8. Identifying CD44 and CD73 surface marker regions – the region of expression of CD44 (Channel 1) and CD73 (Channel 5) was identified using the Identify Primary Object module based on the minimum cross entropy thresholding method.
 9. Estimation of parameters – various parametric features were calculated for the identified singlets based on the geometry, texture and intensity measurements. The modules included MeasureTexture and MeasureGranularity. Using the BF images, a bunch of features such as area, eccentricity, compactness, entropy and granularity were calculated. Using the identified CD44 and CD73 regions, the total intensity of both the markers were also measured. Texture Features such as inverse difference moment and entropy value were also calculated. Inverse difference moment gave a measure of the homogeneity within a defined region. Entropy value indicated the randomness within the structure.
 10. Visualization of singlets – the OverlayOutline module gave the outline of the cell and outline of the CD44 and CD73 markers on the BF image of the cell. These images were saved as .png files with the help of the SaveImages module.
 11. Saving data – in the last section of the workflow, the data of all the calculated values were saved as separate .csv files with the help of the ExportToSpreadsheet module. The data of the geometrical features of the singlets were also saved as a .properties file by the ExportToDatabase module. This .properties file can be used in the future for analysis and classification of the MSCs using the ML approach.

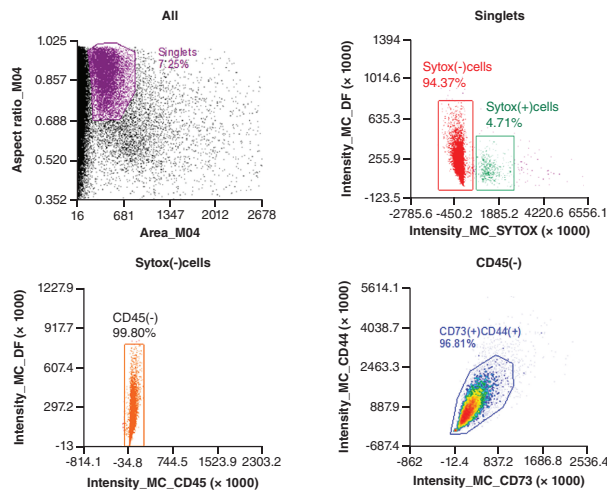
Results & discussion

Conventional flow cytometry-based analysis versus imaging cytometry analysis

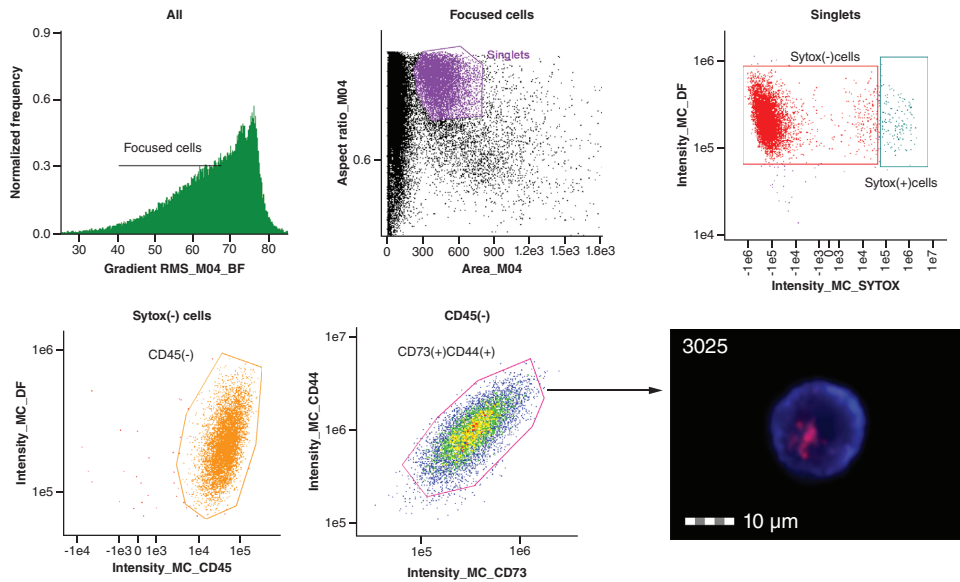
The workflows illustrated in the Figure 1, compared supervised analytical tools with the authors' automated data analysis workflow, MSCProfiler. To understand the robustness of this workflow, they used MSCs from two sources and three different passages: WJMSCs (early passage P6) and SHEDs (later passages P9 and P12). The MSCs in all three passages showed dual expression of the cell surface markers, CD44 and CD73. However, the authors observed distinct populations losing expression of these surface markers toward the later passages (Supplementary Figure 1). The IFC results were analyzed on FCS Express software following the gating strategy as shown in Figure 2A. The next set of analysis following similar flow cytometric logic, as shown in Figure 2B, was performed using IDEAS. The FCS Express analysis revealed that out of 142,171 (the total acquired events) the number of singlets was 10,314, out of which 9733 were live cells (i.e., negative for SYTOX Green), 9714 were CD45 negative and 9404 cells were double positive for both CD44 and CD73, shown in Figure 2A. Similarly, using IDEAS software, out of 142,171 total events, 54,356 were focused cells. From the focused cells, 7900 cells were identified as singlets and 7700 were live cells. Finally, the number of cells positive for both CD44 and CD73 was found to be 7579, as seen in Figure 2B. The gate statistics and the percentages for both the software (FCS express and IDEAS) have been summarized in a tabular format in Figure 2C. The sequential output of IDEAS gating strategy is described in Figure 3A. The visual confirmation of every acquired event during the analysis stage, through the image gallery of IDEAS, served to bolster the gating strategy on the platform. For example, from the image gallery the live cells were confirmed by distinguishing from the images of the cells that had taken up SYTOX Green in Channel 2 for as shown in Figure 3A.

In Figure 4, single cell images as seen in the IDEAS image gallery are shown. In Figure 4A, the width of each cell was also calculated from the BF channel image (top right corner of each image). It displays the image gallery of different sized cells based on their BF information in Figure 4A. The authors observed that the cells could be categorized into three groups based on their cell width ranging between 16–20 μm (small), 20–26 μm (medium) and ≥ 27 μm (large). In Figure 4B, the CD44 and CD73 double positive expressors are shown. A lack of signal can be seen from the SYTOX and CD45 channels. In addition, to understand the dual expression pattern of the two surface markers CD44 and CD73, the corresponding channel images represented by blue and red, respectively, showed co-expression by using the masking feature of IDEAS software. Similar classification was observed in the image gallery of another passage of the SHEDs (P12) and from a different source of MSCs such as the WJMSCs (Figure 4C).

(A) FCS express gating strategy



(B) IDEAS gating strategy



(C) Statistics

Gate	Number of events		% of gated cells	
	FCS express	IDEAS	FCS express	IDEAS
All events:	142,171	142,171	100	100
Focused:	—	54,356	—	38.2
Singlets:	10,314	7900	7.25	5.56
Sytox (-):	9733	7700	6.85	5.54
Sytox (+):	486	142	0.34	0.1
CD45 (-):	9714	7665	6.83	5.39
CD44+CD73+:	9404	7525	6.61	5.29

Figure 2. A comparison between the software FCS Express and IDEAS with regard to the gating strategies used. (A) FCS Express gating strategy shows a hierarchical approach to identifying target cells, which first starts with gating singlets, followed by identification of live cells (negative for SYTOX Green, followed by exclusion gating of CD45 negative cells and then identification of double-positive populations of CD73 and CD44 expressing cells. Gate hierarchy and statistics are indicated in the figure. (B) IDEAS gating strategy followed a similar sequential gating strategy that first identified focused cells, followed by the identification of singlets. Here the same gating hierarchy was followed to identify the double positive expressors (CD44⁺ CD73⁺ mesenchymal stem cells). A representative image of a single live stem cells of human exfoliated deciduous teeth (SHED; cell no. 3025) from the image gallery on the Amnis ImageStream shows the double expressor of CD44 and CD73. (C) The statistics of the different populations analyzed by these supervised platforms have been tabulated.

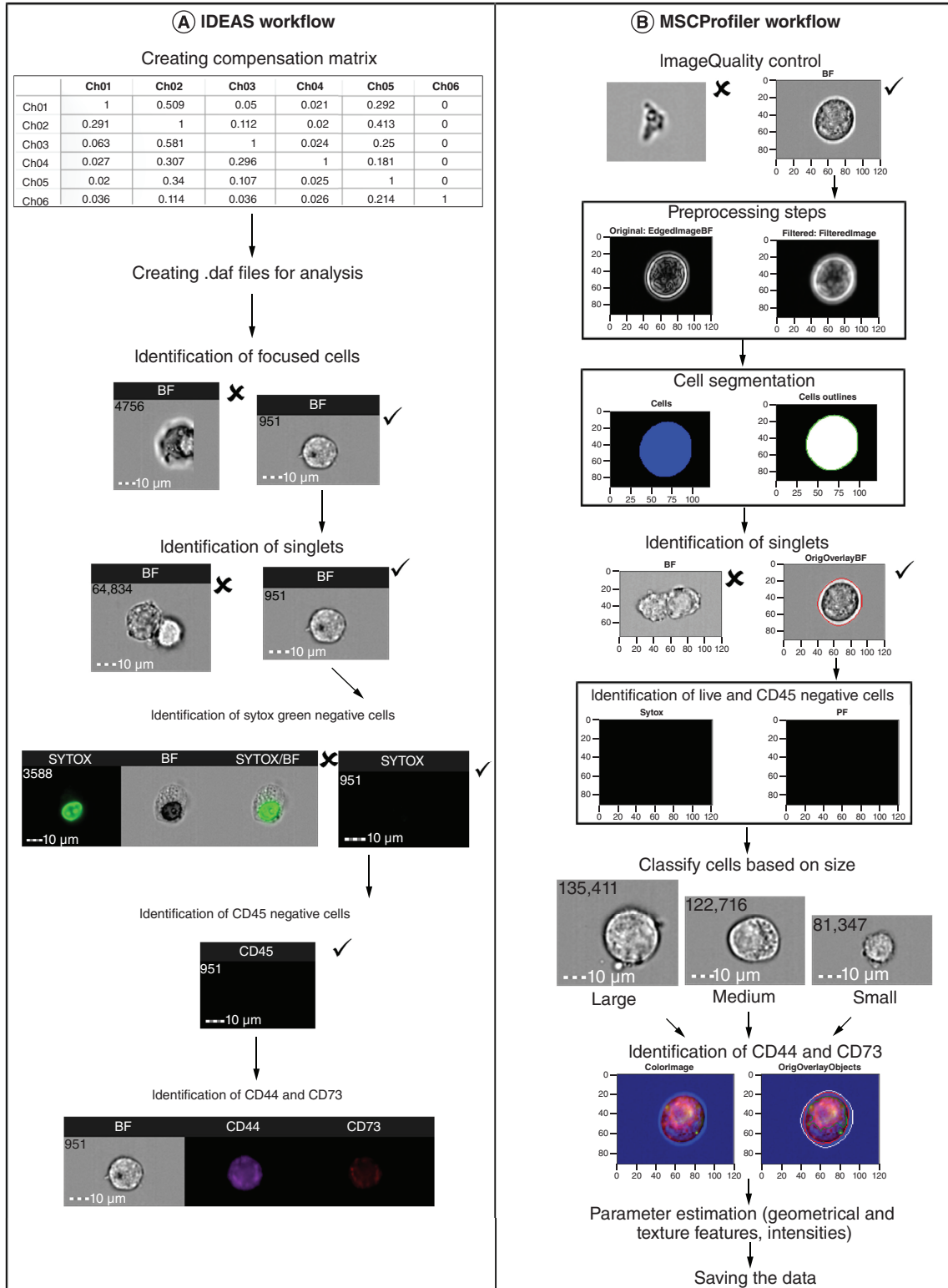


Figure 3. Stepwise identification of populations of stem cells of human exfoliated deciduous teeth (SHED) using the supervised and authors' automated workflow, MSCProfiler. (A) Sequential output of IDEAS workflow following the gating strategy as described. Representative cell images in each step are shown. (B) The sequential output of MSCProfiler workflow shows a comparable end result. However, in the first case, data input includes the .rif, while in MSCProfiler, data input is in the form of single cell images.

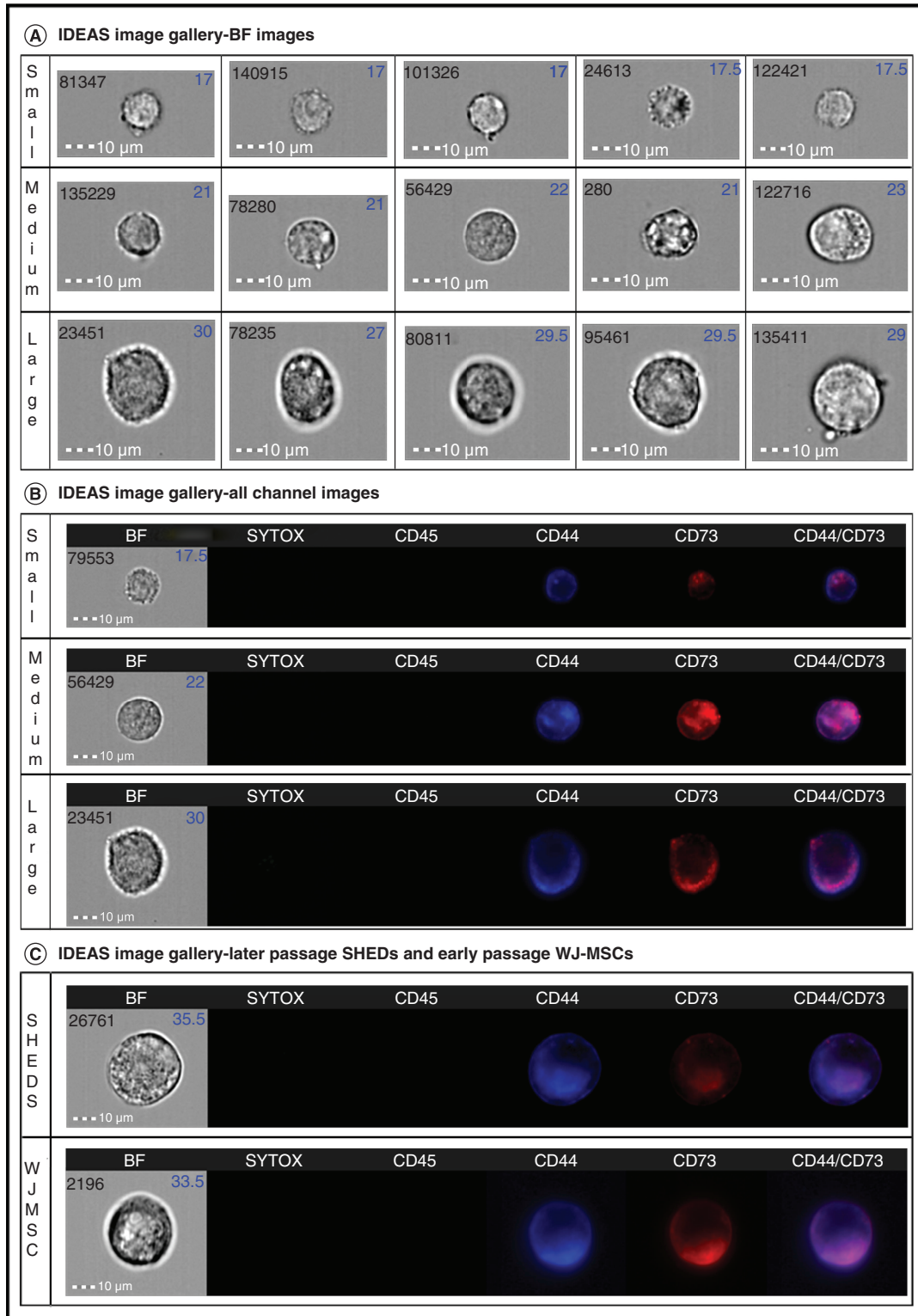


Figure 4. Single cell images are shown from the IDEAS image gallery. Each number indicated in the upper left corner is the cell/event number, and the number in the upper right corner (in blue) indicates the width of the cells. All acquisition was done using the 40× objective. (A) Brightfield images obtained from the IDEAS image gallery show the heterogeneity in size, categorized into small, medium and large observed in stem cells of human exfoliated deciduous teeth (SHEDs) at passage 9. (B) The three different categories of cells in all five channels along with the colocalization mask of CD44 and CD73 are shown. (C) Imaging flow cytometry data of SHEDs at passage 12 and WJMSC at passage 6 were acquired, and representative images of each cell type from all five channels have been shown. WJMSC: Wharton's jelly-derived mesenchymal stem cell.

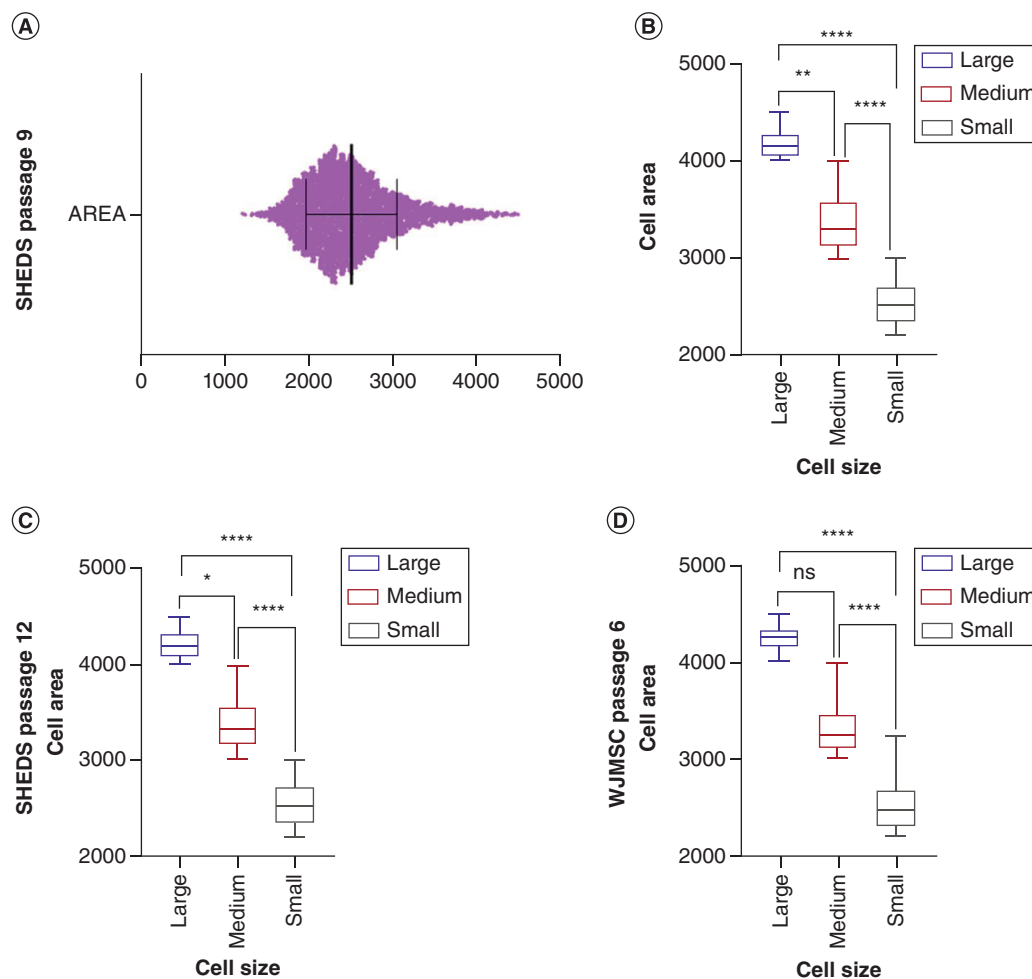


Figure 5. Cell area graphs to demonstrate cell size heterogeneity in mesenchymal stem cells using the MSCProfiler. (A) Graphical representation of the spread/distribution of the area parameter of stem cells of human exfoliated deciduous teeth (SHEDs) at passage 9, run through the MSCProfiler pipeline. (B) Classification into distinct groups of small, medium and large cells based on the cell area of SHEDs at passage 9; 3486 cells obtained as an output of the MSCProfiler pipeline were graphically plotted. (C & D) Images of SHEDs at passage 12 and WJMSC at passage 6 were run on MSCProfiler, then classified into small, medium and large cells. Statistical significance was determined using the Kruskal–Wallis multiple comparisons test using GraphPad Prism (v8.0.1) software.

Analysis using a novel workflow: MSCProfiler

The authors have outlined all the steps that went into building their novel pipeline: the MSCProfiler. The prime benefit of this lay in automation of the analysis workflow, starting from image quality control right up to the parameter estimation and classification of cells, described in Figure 3B. MSCProfiler can be fed with a large number of image sets depending upon the computational bandwidth available to the user. In this study, the datasets were split into batches to perform the analyses to ease out the data size. Post segmentation, the three types of features that were extracted from the imaging modalities were the geometrical and texture features and the intensity values. The 'Focused Cells' (54,356) annotated in this pipeline generated images of SHEDs that revealed statistically significant heterogeneous cell populations within a single passage of MSCs (SHEDs P9). Similarly, roughly 10,000 and 13,000 each of SHEDs (P12) and WJMSC (P6) cells, respectively, were also analyzed using the MSCProfiler (Supplementary Figures 2 & 3). The spread or distribution of area (based on number of pixels in a shape) in the cells (SHEDs P9), as seen in Figure 5A & B, demonstrated three different categories of populations, which were small (2200–2999 pixels), medium (3001–3999 pixels) and large (4008–4493 pixels), and most of the cells belonged to the small category. Categorization of the cell types of WJMSCs (P6) and SHEDs (P12) based on cell size are shown in Figure 5C & D. This also clearly indicates the robustness of the automated workflow using different cell types and passages, without human bias. The implication of this for the morphometric parameters was revealed further in the extraction of geometrical features. The shape quantification of the SHEDs enhanced the authors' understanding of the characterization parameters. With the goal of using

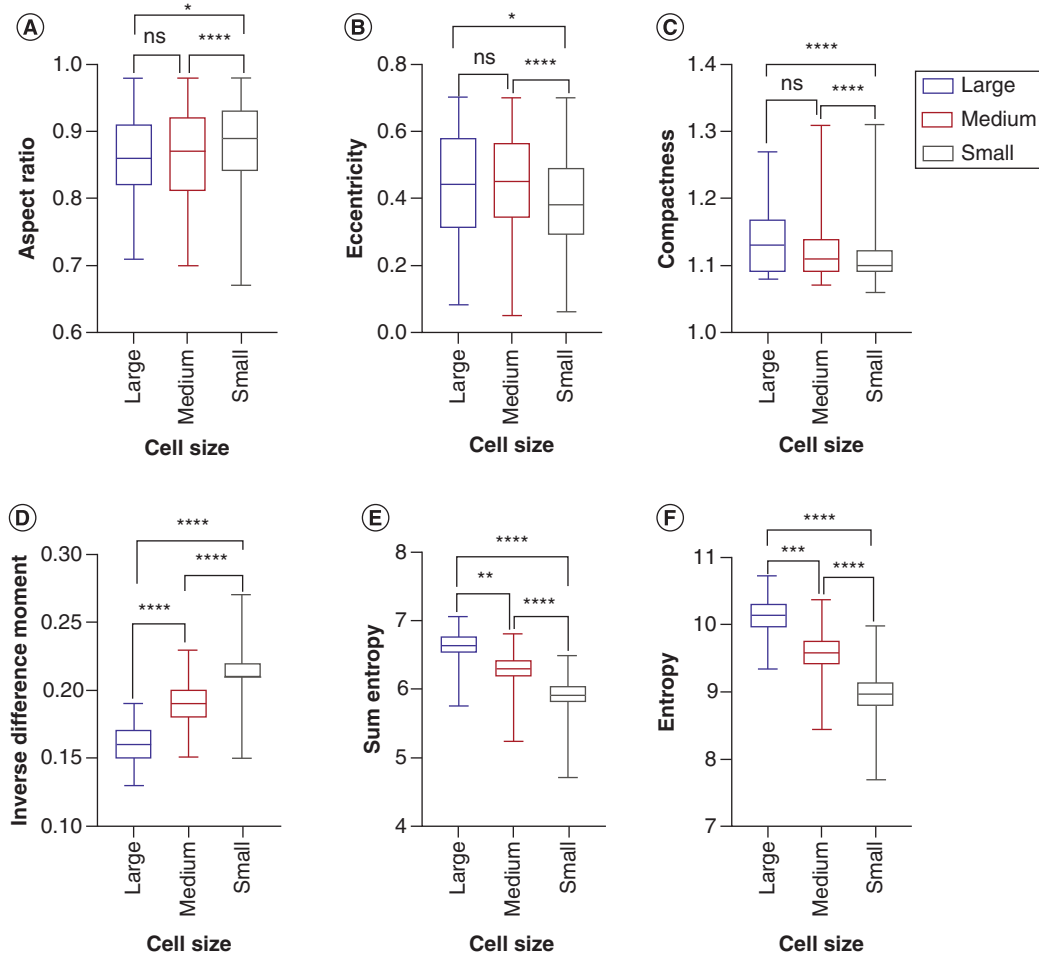


Figure 6. Geometrical and texture parameters demonstrated heterogeneity in mesenchymal stem cells (SHEDs P9) using the MSCProfiler. (A–C) Geometrical features such as aspect ratio, eccentricity and compactness were compared among the three different classes of cells. **(D–F)** Texture features such as inverse difference moment, sum entropy and entropy values were compared among the three different classes of cells in stem cells of human exfoliated deciduous teeth at passage 9. Statistical significance was determined using the Kruskal–Wallis multiple comparisons test using GraphPad Prism (v8.0.1) software.

the minimum necessary measurement features to characterize a single MSC adequately so that it can be unambiguously classified, the authors chose the aspect ratio, eccentricity and compactness of a single cell as discriminators. The performance of the pipeline in determining the shape measurements depended a lot on how the image objects were preprocessed. The distribution of aspect ratio (ratio of image object height vs width) did not show statistical significance among the three categories of cells (small, medium and large), as seen in Figure 6A. Analysis of the annotated pixel values using the Kruskal–Wallis multiple comparisons test demonstrated that the small cells were more circular (close to 1.0) than the medium and large cells from the same passage ($p > 0.99$). However, the distribution was negatively skewed in the small cells because the whisker and half-box were longer on the lower side of the median than on the upper side.

The eccentricity feature (ratio of the minor axis length to the major axis length of an image object) distributed the pixel values (between 0 and 1) and demonstrated that the small cells had lower eccentricity values than the medium and large cells in the same passage, as shown in Figure 6B. The center of distribution of the box and whisker plots was the lowest of the three distributions in the small cells (median: 0.2–0.4), while in the others the median was between 0.4 and 0.6. The distribution in all three classes was approximately symmetric, as both the half-boxes were almost the same length on both upper and lower sides. According to the statistics, small cells were more circular than the other two categories.

Cell shape measure can be best calculated from descriptors such as mean compactness (ratio of the area of an image object to the area of a circle within the same perimeter). A circle is depicted by a minimum value of 1.0. The larger the compactness, the more irregularities and complexities of the cell boundary. The small cells showed lower compactness values than the medium and large cells,

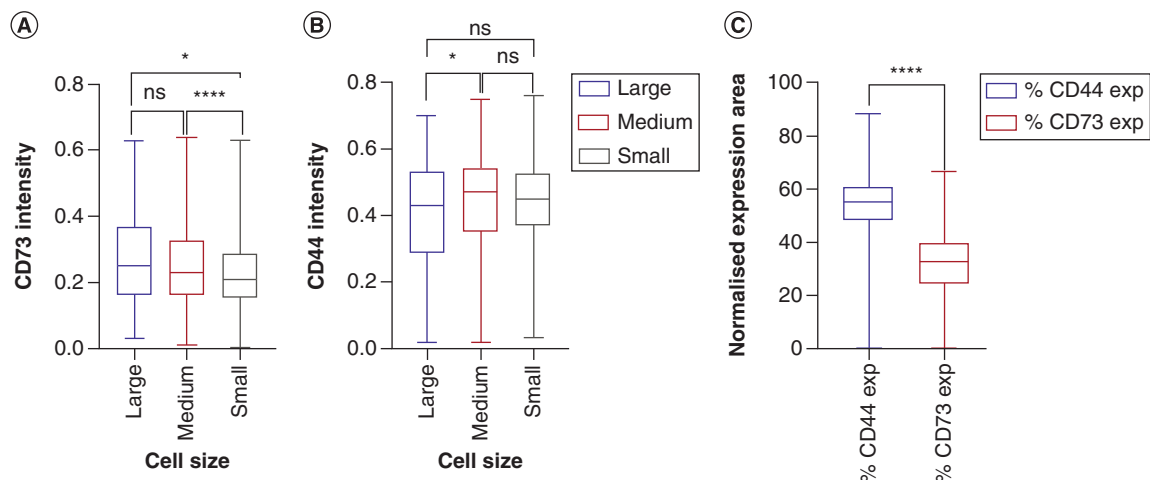


Figure 7. Fluorescence parameters demonstrate heterogeneity in SHEDs (P9) using the MSCProfiler. (A & B) Intensity of CD73 and CD44 expression compared among the three classes of cells. (C) Normalized values of cell area expressing markers CD44 and CD73 were compared. CD44 was expressed over a larger area when compared with CD73, significantly ($p < 0.0001$). Statistical significance was determined using the Mann–Whitney test using GraphPad Prism (v8.0.1) software (%CD44 Exp and %CD73 Exp denote the normalized percentage of CD44 and CD73 expression area, respectively).

as shown in Figure 6C. The center of distribution of the box and whisker plots was the lowest of the three distributions in the small cells (median: 1.0–1.1), while the medium cells had distributed values between 1.07 and 1.31 and large cells between 1.08 and 1.27. However, the distribution was positively skewed in the small cells because the whisker and half-box were longer on the upper side of the median than on the lower side.

Texture features are also very important computational feature extraction descriptors. They bring about the values between shapes and individual pixel values. An important measure of variation brought about from the Haralick texture features is inverse difference moment. It is a measure of homogeneity in cells, which gets maximized when neighboring image pixels share same values (i.e., while measuring texture analysis, two pixels are considered at a single time, the reference and neighbor pixel). The spatial relationship between the reference and neighbor pixel is calculated to understand the gray level differences. There were stark differences among the three classes of cells in terms of inverse difference moment, as seen in Figure 6D (also refer to Supplementary Figure 3). The small cells were more homogeneous in terms of texture compared to the other two classes of cells- the medium and large cells. It provided high discrimination accuracy for images acquired in motion. This discriminator for local homogeneity is lower in medium and much lower in large cell types. The center of distribution of the box and whisker plots was the highest of the three distributions in the small cells (median: 0.2–0.25), while the medium cells had distributed values close to 0.2 and large cells close to 0.15.

Entropy of population analysis can reveal highly structured cellular patterns. IFC dataset distributions are being utilized for identification of malignancy in other cell types by analyzing the differences in multidimensional distributions of related entropies. The entropy and combined entropy of the small cells (9.0) were lowest compared with the medium (9.5) and large cell types (10.71). The center of distribution of the box and whisker plots in all three sets showed homogeneous entropy patterns. More entropy-based patterns could be identified from the medium and large cells, as described in Figure 6E & F. Application of these textural entropy investigations can evaluate the homogeneity and randomness of gray values within the BF cell images, essentially making it a label-free digital image analysis of single cells.

In terms of biomarker expression, CD73-PerCP Cy5.5 and CD44-V450 expression levels were compared in SHEDs (P9). CD73 intensity of expression was higher in the large cells compared with the medium and small cells, as seen from Figure 7A. The authors observed that the CD44 expression levels were higher than CD73 in all three cell types, represented in Figure 7B. To compare the distribution pattern of both the markers, the authors normalized the cell area from which CD44 and CD73 showed expression, by dividing that area by total area of the cell to obtain percentage expression. Results showed that CD44 was expressed over a larger area when compared with CD73, significantly ($p < 0.0001$) when analyzed using the Mann–Whitney test shown in Figure 7C. FCS Express software analyzed a population of 0.27% and 0.69% of cells which were non-expressers of CD44 and CD73 in SHEDs P9 and P12, respectively (Supplementary Figure 1). Although MSCProfiler can identify these rare cell populations, a greater number of datasets and additional criteria are required to modify the existing pipeline (part of an ongoing study).

MSC heterogeneity has been documented by many researchers. It can be derived from different sources of tissues or even arise randomly from a clonally dividing cell population. However, what is debatable is whether the appearance of such cellular heterogeneity

within the MSC population follows a stochastic or a deterministic process. Identifying heterogeneity among the MSCs has always been a challenge, in which the classical approach using microscopy and standard cytometry assays gives information about their surfaceome but not an exhaustive one, as these stem cells do not express any exclusive signature surface markers. There have been attempts using deep learning and ML methods to explore functional heterogeneity and phenotypic and morphometric classification in MSCs. However, most of these studies have been conducted at the population level using microscopic imaging of MSC *in vitro* cultures, which restricts the sample size for analyses [23]. Few reports of *in silico* studies using single cell images of MSCs are under way, and all of these use comprehensive image processing algorithms with extensive knowledge of image processing computational tools [19]. MSCProfiler captures the information of MSC heterogeneity based on the texture features of the single cells from IFC and helps explain the detailed cellular features of the population. The existence of heterogeneity is proof enough to show that studies must not be limited to population level but must also look at single cell expression. This will help researchers come up with more stringent protocols for identifying MSCs best suited for clinical purposes. This brings in the rationale of the present study in developing an unsupervised workflow that can assist a stem cell biologist in the appropriate identification and classification of MSCs best fit for specific translational studies.

Feature extraction from images of single cells was the hallmark of this study, which led the authors to develop the MSCProfiler workflow. The aim was to identify postacquisition pattern recognition of MSCs (SHEDs) based on multiple image features of single cells such as aspect ratio, cell texture, shape, surface antigen distribution and intensities of expression of such antigens. The authors characterized the gross surfaceome of the SHEDs in this study by developing a nonsupervised image processing pipeline that can robustly segment and analyze single cell morphologies from BF standalone images. There are multiple robust, high-end screening image analysis programs available that can quantify visual cellular morphotypes by microscopy [15]. However, the critical criteria in any such image analysis tool should be lack of bias, ability to identify image-based aberrations (image blur, debris crowding, autofluorescence, saturation of pixels) and high speed of resolution of individual image objects. This pipeline used images of single cells generated from an imaging flow cytometer (Amnis ImageStream Mk II platform), which collectively gives an advantage and takes care of most of the image-based aberrations, making a single image object for acquired data files. This feature rules out the first concern of shadowing of cellular features in case of a smear or a tissue slice [24]. In this paper, the authors have described an automated protocol implemented in validated open-source software called CellProfiler [24–26] with the capacity to offer a suite of image-based measurement features which can extract quantitative information from images. In addition, the parameters extracted from this workflow can be further used to build an unbiased categorization of single cells based on the phenotypes using ML approaches. Though such tasks can be programmed using R/Python there are more user-friendly tools like CellProfiler Analyst. In fact, with the workflow described in this paper it is possible to extract cellular parameters in file formats that are supported by CellProfiler Analyst.

Although conventional flow cytometry on its own can be a source of high-throughput screening for large datasets, IFC has been able to plug in the image data output to further enhance its throughput. The authors have strategically validated their pipeline with both conventional and image flow cytometry data and demonstrated the shortcomings in either case. Conventional flow cytometry lacks spatial information of every dot on the analysis plot, while IDEAS on the Amnis platform is proprietary and needs to be customized to meet individual needs. This has been one of the first attempts to screen for cellular heterogeneity of MSCs using morphometric features of single cells.

Conclusion

MSCProfiler is an approach to analyzing IFC data that adds valuable information from the images concurrently with conventional flow cytometric analysis. This would be the value addition to answering the respective biological questions that can be resolved using MSCs. This method is completely automated, and so there is no human bias, which was one of the crucial challenges of the other currently available techniques. It does not require extensive programming knowledge to perform such an intense analysis. Analyzing other sources of MSCs and different passages within the same type highlights the robustness of the workflow developed. However, having a high computational processing capacity to analyze thousands of image datasets should be considered as a caveat while using the MSCProfiler. As this pipeline is dependent on the computational power of the data processing system, it brings along with it the time constraint and the data storage of large file sizes (.daf file generated from the IDEAS software is ~0.1 GB). Our study used only five parameters to be analyzed by the MSCProfiler. In cases where more parameters need to be explored (6–12), other data analytical tools such as Cytominer or customized algorithms have to be employed to classify these image sets. In this study, we had to segregate the images into groups of 10,000–20,000 images for a run time of 2–4 h on the MSCProfiler.

Future perspective

This study has been one of the first attempts to screen cellular heterogeneity of MSCs derived from two different tissue sources using morphometric features of single cells. An automated workflow provided by the MSCProfiler has proved to be an unbiased approach to extracting image texture information from a huge range of single cell images that is not dependent on the instrument generating the data. Our workflow has been able to extract similar morphometric features of different types of MSCs in an unbiased manner. On the other hand, MSCProfiler can also be used to identify different cell populations with the inclusion of additional criteria such as fluorescence signals of the surface markers and correlate the extracted texture features for their identification. This is being evaluated with ongoing experiments on identification of hematopoietic stem cells or ‘blasts’ in human bone marrow samples. Most importantly, MSCProfiler

does not require knowledge of any advanced computation language to apply this pipeline to the study of single cells. MSCs have a huge potential in drug discovery and cell-based therapeutic applications. While manufacturing clinical grade MSCs in an expanded scale, the availability of a quality assurance/quality control software such as the MSCProfiler can set comparable and rigorous standards for the production systems for cell culture. The stem cell heterogeneity, arising due to isolation, culture and expansion conditions, warrants a robust tool to set quality standards for these stem cells during production and make the supply more consistent and uniform in an efficient and cost-effective manner.

Executive summary

- To address the challenges in defining single cell phenotypes, an automated pipeline was developed using an enhanced image feature extraction approach.

Experimental

- Mesenchymal stem cells (MSCs) from stem cells derived from human exfoliated deciduous teeth (SHEDs) and Wharton jelly-derived MSCs (WJMSCs) obtained from the umbilical cord tissue, across different passages, were immunostained in single cell suspension and quantified using imaging flow cytometry on the Amnis ImageStream platform.
- Using these single cell images, an automated pipeline named MSCProfiler was developed. The workflow was developed using CellProfiler software to analyze the single cell images of mesenchymal stem cells.

Results & discussion

- The prime focus in automation of the analysis workflow (MSCProfiler) started from image quality control right up to parameter estimation and classification of cells.
- Postsegmentation, these images were classified to calculate geometrical and texture features such as shape, size, eccentricity and entropy along with intensity values of the surface markers from over 50,000 single cell images obtained from imaging flow cytometry.
- The texture features of the mesenchymal stem cells such as inverse difference moment, sum entropy and entropy values proved to be very important feature descriptors that showed differences between different passages of SHEDs and between SHEDs and WJMSCs.
- In terms of biomarker expression, CD73-PerCP Cy5.5 and CD44-V450 expression levels also showed additional differences in patterns. Results showed that CD44 was expressed over a larger area when compared with CD73 among the SHEDs.

Conclusion

- Development of the MSCProfiler was an approach to analyze the imaging flow cytometry data that added valuable information from the images concurrently with the conventional flow cytometry analysis. The hallmark of this screening pipeline was the identification and removal of nontarget images and extraction of features from single cell brightfield and fluorescent images of single cells. This was an important value addition to answering the respective biological questions of the mesenchymal stem cells.

Supplementary data

To view the supplementary data that accompany this paper please visit the journal website at: www.future-science.com/doi/suppl/10.2144/btn-2023-0048

Author contributions

Each coauthor listed participated sufficiently in the work to take responsibility for the content, and all those who qualify are listed. U Chakraborty and L Balasubramanian conceptualized and designed the study. A Gupta and SK Shaik performed the experimental work, analyzed the associated data, contributed to writing portions of the draft of the manuscript and revised it critically for important intellectual content. U Chakraborty, A Gupta and L Balasubramanian contributed to the analysis and interpretation of data. L Balasubramanian contributed to the data curation and establishment of the pipeline. U Chakraborty and L Balasubramanian contributed to the final approval of the version to be published. U Chakraborty supervised the entire study, including project administration, investigation and original draft writing and agreed to be accountable for all aspects of the work in ensuring that questions related to the accuracy or integrity of any part of the work are appropriately investigated and resolved. All authors approved the final manuscript.

Acknowledgments

The authors thank Cytek Biosciences for its support in providing the Amnis Imagestream Mark II imaging flow cytometer in their facility. They are grateful to Debjani Kundu, field application scientist, Cytek, for helping with data analysis on the IDEAS software. They thank Risani Mukhopadhyay for providing raw image files of Wharton's jelly-derived mesenchymal stem cells for analysis. The authors are grateful to the Manipal Institute of Regenerative Medicine for its support in conducting the experiments. A. Gupta is grateful for the support of TMA Pai Scholarship from Manipal Academy of Higher Education.

Financial disclosure

Financial and material support was received for this research by Intramural Grant Manipal Academy of Higher Education, Manipal, India. The authors have no other relevant affiliations or financial involvement with any organization or entity with a financial interest in or financial conflict with the subject matter or materials discussed in the manuscript apart from those disclosed.

Competing interests disclosure

The authors have no competing interests or relevant affiliations with any organization or entity with the subject matter or materials discussed in the manuscript. This includes employment, consultancies, honoraria, stock ownership or options, expert testimony, grants or patents received or pending or royalties.

Writing disclosure

No writing assistance was utilized in the production of this manuscript.

Ethical conduct of research

Institutional Committee on Stem Cell Research approval for conducting this research was obtained. For sample procurement (human third molar teeth and umbilical cord tissue) concerned hospital ethical clearance certificate was obtained for the work.

Open access

This work is licensed under the Attribution-NonCommercial-NoDerivatives 4.0 Unported License. To view a copy of this license, visit <http://creativecommons.org/licenses/by-nc-nd/4.0/>

References

Papers of special note have been highlighted as: • of interest

- Andrzejewska A, Lukomska B, Janowski M. Concise review: mesenchymal stem cells: from roots to boost. *Stem Cells* 37(7), 855–864 (2019).
- da Silva Meirelles L, Chagastelles PC, Nardi NB. Mesenchymal stem cells reside in virtually all post-natal organs and tissues. *J. Cell Sci.* 119(11), 2204–2213 (2006).
- Glenn JD. Mesenchymal stem cells: emerging mechanisms of immunomodulation and therapy. *World J. Stem Cells* 6(5), 526–539 (2014).
- Saeedi P, Halabian R, Fooladi AAl. A revealing review of mesenchymal stem cells therapy, clinical perspectives and modification strategies. *Stem Cell Investig.* 6, 34 (2019).
- Wilson A, Webster A, Genever P. Nomenclature and heterogeneity: consequences for the use of mesenchymal stem cells in regenerative medicine. *Regen. Med.* 14(6), 595–611 (2019).
- Pittenger MF, Discher DE, Péault BM *et al.* Mesenchymal stem cell perspective: cell biology to clinical progress. *NPJ Regen. Med.* 4(22), (2019).
- Lansdowne LE. Single cell analysis – advantages, challenges, and applications (2019). www.technologynetworks.com/drug-discovery/blog/single-cell-analysis-advantages-challenges-and-applications-322768
- This paper will enable the reader to understand single cell technology.
- Hennig H, Rees P, Blasi T *et al.* An open-source solution for advanced imaging flow cytometry data analysis using machine learning. *Methods* 112, 201–210 (2017).
- Maguire O, O’Loughlin K, Minderman H. Simultaneous assessment of NF- κ B/p65 phosphorylation and nuclear localization using imaging flow cytometry. *J. Immunol. Methods* 423, 3–11 (2015).
- Phadwal K, Alegre-Abarrategui J, Watson AS *et al.* A novel method for autophagy detection in primary cells: impaired levels of macroautophagy in immunosenescent T cells. *Autophagy* 8(4), 677–689 (2012).
- Pugsley HR. Quantifying autophagy: measuring LC3 puncta and autolysosome formation in cells using multispectral imaging flow cytometry. *Methods* 112, 147–156 (2017).
- Durdik M, Kosik P, Gursky J *et al.* Imaging flow cytometry as a sensitive tool to detect low-dose-induced DNA damage by analyzing 53BP1 and γ H2AX foci in human lymphocytes. *Cytometry A* 87(12), 1070–1078 (2015).
- Lee Y, Wang Q, Shuryak I, Brenner DJ, Turner HC. Development of a high-throughput γ -H2AX assay based on imaging flow cytometry. *Radiat. Oncol.* 14(1), 1–10 (2019).
- Filby A, Perucha E, Summers H *et al.* An imaging flow cytometric method for measuring cell division history and molecular symmetry during mitosis. *Cytometry A* 79(7), 496–506 (2011).
- The potential of using imaging flow cytometry is appropriately described in this paper.
- Negm AS, Hassan OA, Kandil AH. A decision support system for acute leukaemia classification based on digital microscopic images. *Alex. Eng. J.* 57(4), 2319–2332 (2018).
- Helgadottir S, Midvedt B, Pineda J *et al.* Extracting quantitative biological information from bright-field cell images using deep learning. *Biophys. Rev.* 2(3), 31401 (2021).
- Imboden S, Liu X, Lee B, Payn MC, Hsieh C-J, Lin NYC. Investigating heterogeneities of live mesenchymal stromal cells using AI-based label-free imaging. *Sci. Rep.* 11(1), 6728 (2021).
- Ottesteanu CF, Ugrinic M, Holzner G *et al.* A weakly supervised deep learning approach for label-free imaging flow-cytometry-based blood diagnostics. *Cell Rep. Methods* 1(6), 100094 (2021).
- Kim G, Jeon JH, Park K, Kin SW, Kim DH, Lee S. High throughput screening of mesenchymal stem cell lines using deep learning. *Sci. Rep.* 12(1), 17507 (2022).
- Sanz G, Martinez-Aranda LM, Tesch PA, Fernandez-Gonzalo R, Lundberg TR. Muscle2View, a CellProfiler pipeline for detection of the capillary-to-muscle fiber interface and high-content quantification of fiber type-specific histology. *J. Appl. Physiol.* 127(6), 1698–1709 (2019).
- Dominici M, Le Blanc K, Mueller I *et al.* Minimal criteria for defining multipotent mesenchymal stromal cells. The International Society for Cellular Therapy position statement. *Cytotherapy* 8(4), 315–317 (2006).
- Chan DK, Miskimins WK. Metformin and phenethyl isothiocyanate combined treatment *in vitro* is cytotoxic to ovarian cancer cultures. *J. Ovarian Res.* 5(1), 19 (2012).
- Gundry RL, Riordon DR, Tarasova Y *et al.* A cell surfaceome map for immunophenotyping and sorting pluripotent stem cells. *Mol. Cell. Proteomics* 11(8), 303–316 (2012).
- Bray MA, Carpenter AE. Quality control for high-throughput imaging experiments using machine learning in CellProfiler. *Methods Mol. Biol.* 1683, 89–112 (2018).
- This paper will enable the reader to understand the baseline software that was used to develop the MSCProfiler pipeline/workflow.
- Lamprecht MR, Sabatini DM, Carpenter AE. CellProfiler™: free, versatile software for automated biological image analysis. *BioTechniques* 42(1), 71–75 (2007).
- This paper will enable the reader to understand the baseline software that was used to develop the MSCProfiler pipeline/workflow.
- Bray MA, Vokes MS, Carpenter AE. Using CellProfiler for automatic identification and measurement of biological objects in images. *Curr. Protoc. Mol. Biol.* 109, 14.17.1–14.17.13 (2015).
- This paper will enable the reader to understand the baseline software that was used to develop the MSCProfiler pipeline/workflow.

Keywords or phrases:

Artificial intelligence (AI), Label-free cell analysis, cytotoxicity assay, live-cell analysis, cell viability, advanced image analysis

AI-Driven Label-Free Quantification of Cell Viability Using Live-Cell Analysis

Jasmine Trigg¹, Daniel Porto², Nevine Holtz², Nicola Bevan¹, Timothy Jackson¹, Timothy Dale¹, Gillian Lovell¹

1. Sartorius UK Ltd, Royston, Hertfordshire, UK

2. Sartorius Ann Arbor MI, USA

Correspondence

Email: AskAScientist@sartorius.com

Introduction

Live-cell imaging enables acquisition of phase contrast images and provides an ideal platform to study multi-faceted biological paradigms in drug discovery. This is vital to our understanding of human diseases and treatment strategies. The movement of these models towards increasingly complex physiologically relevant ones, including patient-derived cells and induced pluripotent stem cells (iPSCs), has concurrently driven the need for label-free methods that are non-perturbing to deliver deeper biological insights.^{1,2} The elimination of fluorescent reporters reduces workflow time, ensures that experimental outcomes are not attributed to the label, or labeling process itself, and is non-perturbing for when fluorescent labeling is not possible, such as when using rare or sensitive cell types.^{3,4}

Incorporating artificial intelligence (AI) into image analysis workflows has enabled powerful quantification of a wide range of cellular models, allowing researchers to make data-driven decisions and understand disease at a more granular level.⁵ These leading-edge technologies, based on neural-network algorithms, are much more complex than traditional image analysis and facilitate more robust segmentation of heterogeneous cell morphologies whilst minimizing user-introduced bias.² However, there exists several barriers to the widespread use of AI in image analysis, including hardware requirements, knowledge of training and testing methods, access to robust datasets for training, pre- and post-processing image analysis pipelines with a vast amount of data, and the general applicability of algorithms across cell types.⁶

Find out more: www.sartorius.com/incucyte-ai-cell-health-software

In this application note, we describe an automated, robust solution for label-free cell segmentation and live/dead classification of individual cells using integrated AI-based software. The Incucyte® AI Cell Health Analysis Software Module, driven by trained convolutional neural networks (CNN), allows us to reliably monitor cell viability in a non-perturbing unbiased manner with minimal user input.

Here, we show validation of the analysis software across a wide range of live and dead adherent and non-adherent cell types and exemplify how this approach can provide high-throughput, physiologically relevant insights into cell health through accurately predicting cell death across multiple treatments.

Assay Principle

The Incucyte® AI Cell Health Analysis Software Module enables label-free quantification of live or dead cells. The analysis module uses trained CNNs, which automatically analyze images to segment individual cells and classify them as live or dead, all in one step. This streamlined workflow (Figure 1) requires little user input, providing unbiased results which can be directly compared across assays.

Phase contrast images are acquired using AI Scan acquisition with 10x or 20x objectives. These images can be analyzed using Incucyte® AI Cell Health Analysis Software Module which provides metrics such as Total Cell Count (All Objects), as well as the number and percentage of live and dead cells. In cases where optional fluorescence images are acquired, the Mean and Total Integrated Intensity within all cells, as well as the live or dead subpopulations, will be provided. Fluorescence classification can be performed as an additional analysis, again providing metrics describing the count and percentage of high vs low fluorescence within total cells, and within live or dead subpopulations.

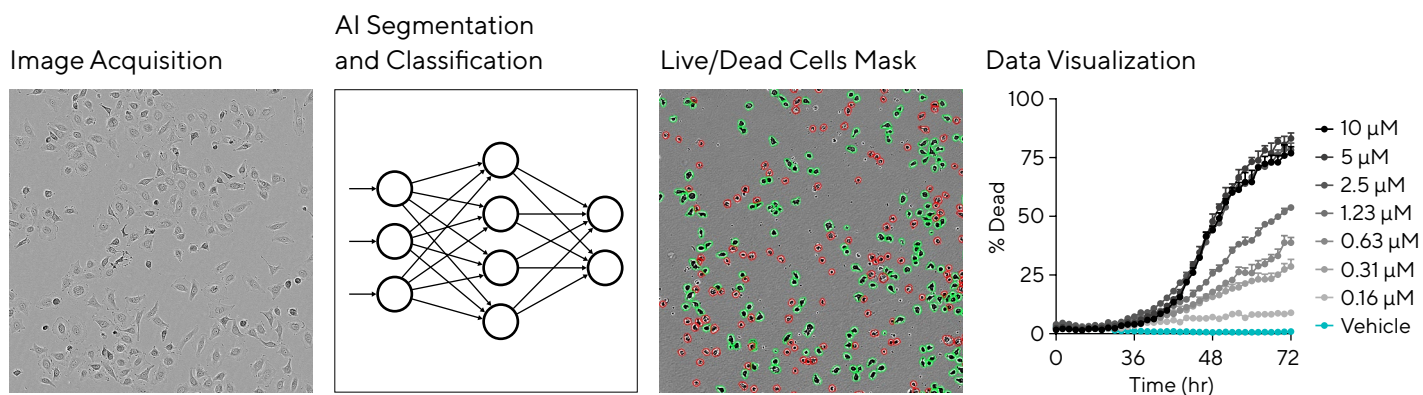


Figure 1: Incucyte® AI Cell Health Analysis Workflow.

Phase Contrast Images Are Acquired and Processed Using Neural Networks (CNN), to Automatically Segment and Classify Cells as Live or Dead.

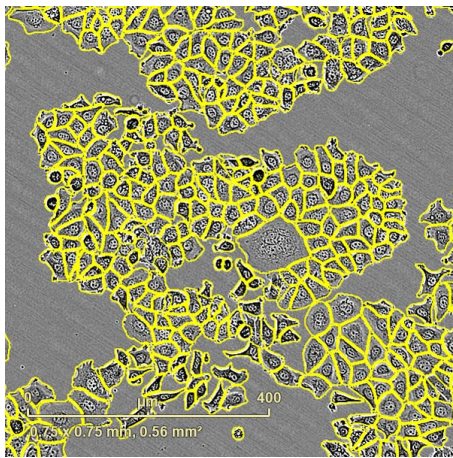
Precise segmentation provides accurate cell count data even at high cell confluence (up to 99% depending on cell morphology), yielding reliable proliferation data. Label-free classification of cells as live or dead enables quantification of cell viability within a physiologically relevant and non-perturbing environment. Combining this label-free analysis with optional fluorescence readouts from the live or dead subpopulations provides additional insight into mechanisms of cell death.

AI-Driven Cell Segmentation

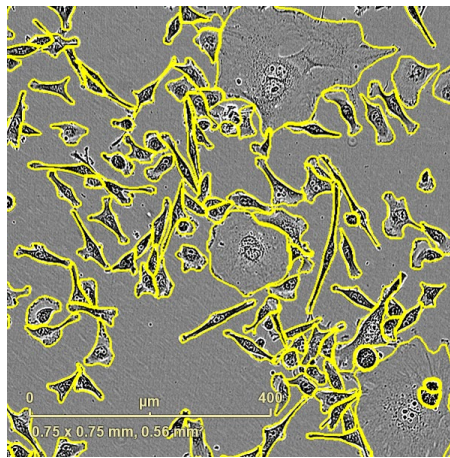
The AI Cell Health segmentation model was trained using phase contrast images which were manually annotated to identify the boundary of individual cells. A wide diversity of over 2 million individual cells were annotated including adherent and non-adherent cell types at a range of confluences, both healthy and apoptotic; adherent cell examples covered a wide range of morphologies. This broad spectrum of cells ensures that the final trained model is highly versatile, competently segmenting a multitude of cell types - even those which were not included within the training and validation datasets.⁷

The resulting segmentation is highly accurate even in confluent images and adapts to a multitude of cell morphologies - even where these are present within the same image. Figure 2 shows the AI segmentation applied to a highly clustering breast cancer cell line (MCF-7), an invasive epithelial-like cell line (MDA-MB-231), flat and transparent primary cells (primary rat astrocyte), and a non-adherent B cell line (Ramos). In addition, dead cells are accurately delineated (HMC3 cells treated with camptothecin, 1.1 μ M), as are monocytes in the presence of pHrodo[®] Bioparticles[®] for Incucyte[®] (RAW 264.7 in the presence of *E. coli* bioparticles, 10 μ g per well).

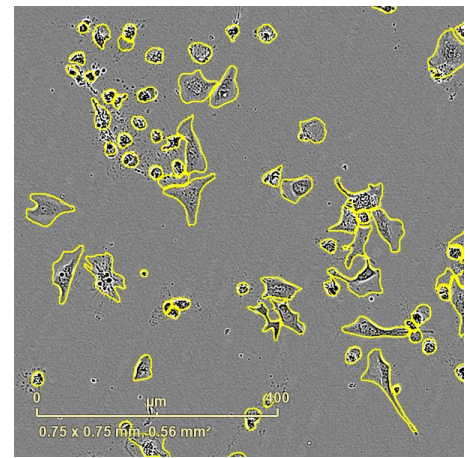
MCF-7



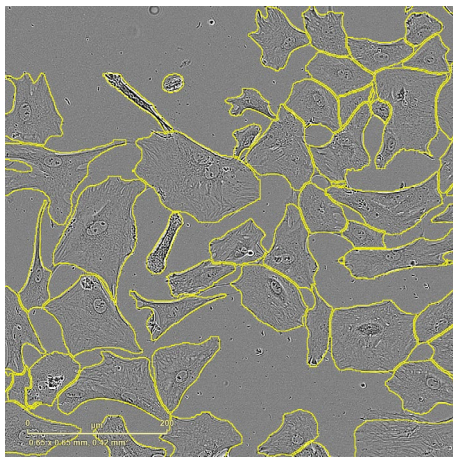
MDA-MB-231



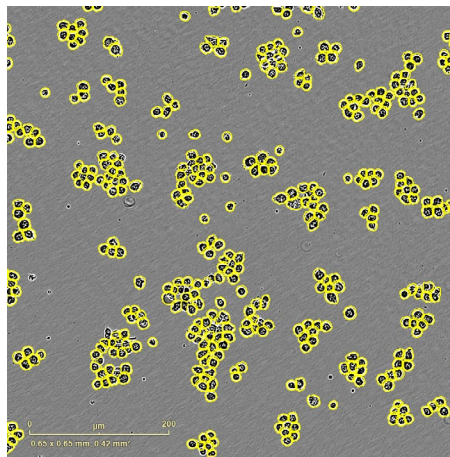
HMC3 + Camptothecin



Primary rat astrocyte



Ramos



RAW 264.7 + *E. coli*

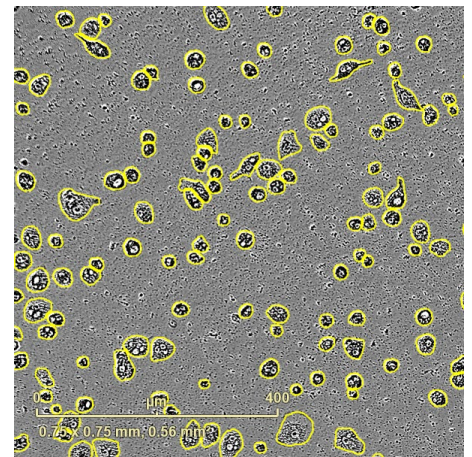


Figure 2: AI Cell Health Analysis Accurately Segments a Wide Range of Cell Types With Diverse Morphologies, Including Apoptotic Cells and Cells in the Presence of Bioparticles.

The segmentation model is trained specifically to detect cells and therefore ignores most non-cell objects. Cell segmentation is thus possible even in the presence of debris, compound precipitate, or bioparticles. Figure 3 demonstrates this advantage, showing primary macrophages accurately segmented in the presence of pHrodo® *E. coli* Bioparticles® for Incucyte® (10 µg/mL, 24 hr post treatment). As the bioparticles are engulfed, they are processed into acidic lysosomes, and the low pH causes the pHrodo® label to increase in fluorescence intensity. Quantification of fluorescence within the AI-masked cell boundary shows increasing intensity over time as the

bioparticles are engulfed (Figure 3B), and the total intensity is dependent on the densities of both bioparticles and cells (Figure 3C). Fluorescence classification of cells as high or low intensity enables identification of cells which are phagocytic (Figure 3D). At 30 µg/mL bioparticles, around 40% of the cells are phagocytic; this percentage decreases as the amount of bioparticles decreases. Interestingly, the percentage of phagocytic cells is independent of the cell seeding density but increases with higher bioparticle density, suggesting the bioparticles themselves have an activating effect.

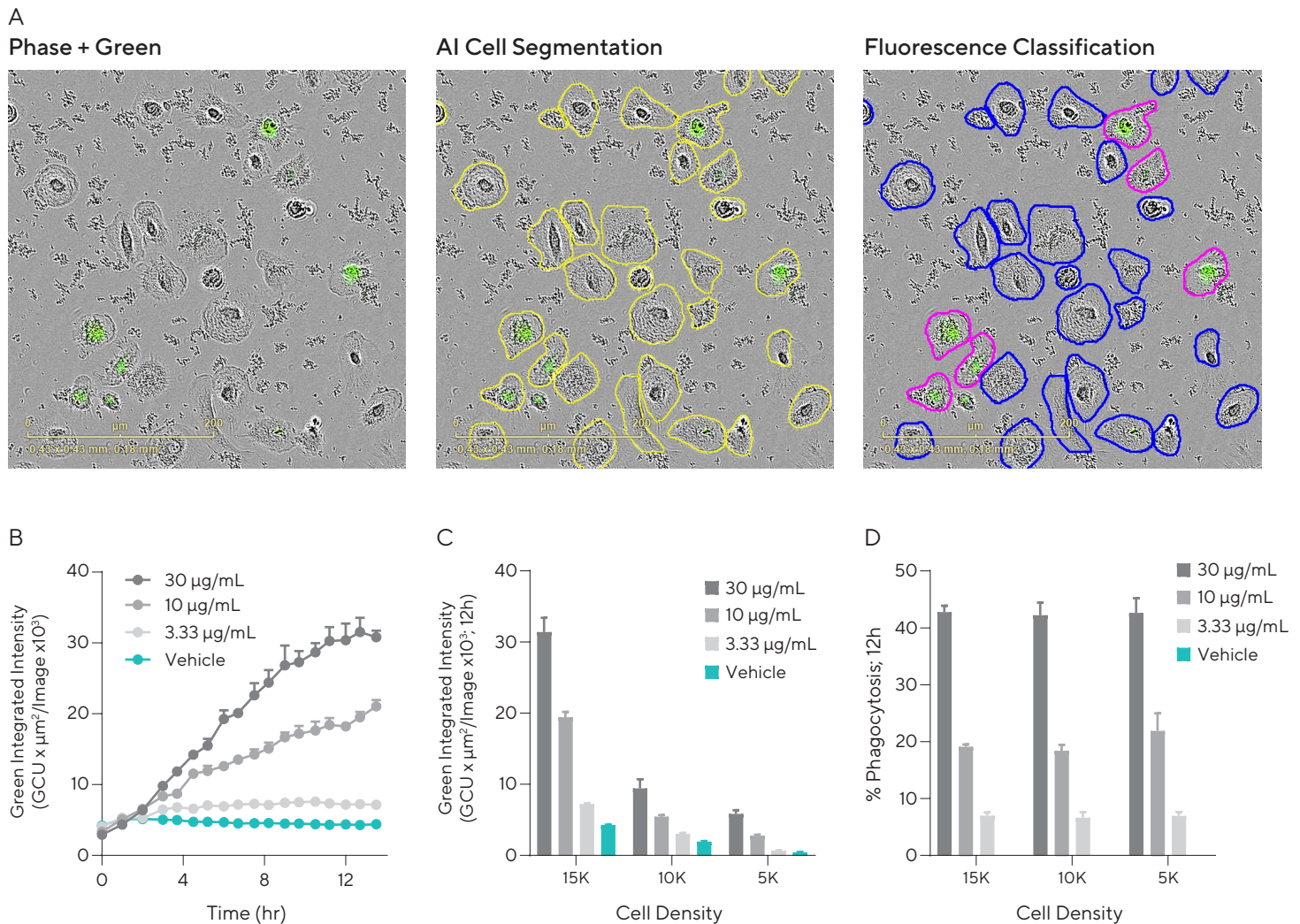


Figure 3: Robust Cell Segmentation Enables Accurate Quantification of Phagocytic Cells.

Images show primary macrophages 12 hr post treatment with pHrodo® *E. coli* Bioparticles® for Incucyte® (A). Non-engulfed bioparticles are visible in the phase contrast image while engulfed bioparticles fluoresce (green). AI Cell Segmentation shows accurate masking of cells alone, and fluorescence classification indicates phagocytic (magenta outline, high fluorescence) and non-phagocytic (blue outline, low fluorescence) cells. Time course demonstrates increasing fluorescence intensity within the segmented cell boundary over 12 hr (B). The increase in fluorescence is both cell- and bioparticle-dependent (C), while the percentage of phagocytic cells is dependent on bioparticle concentration but not cell density (D).

AI-Driven Live/Dead Classification

The AI model for classification was trained using pairs of phase contrast and fluorescence images of cells treated with cytotoxic compounds in the presence of Incucyte® Cytotox Dye. These paired images enable the neural network to infer cell death responses from the phase contrast image alone. These two AI models were combined to form the Incucyte® AI Cell Health Analysis Software Module, which was validated on multiple cell types using fluorescent markers for comparison. During validation studies, cells were treated with cytotoxic compounds in the presence of Incucyte® Cytotox Dye which enters non-viable cells, increasing their fluorescence intensity. Quantification of cell death was performed using both AI Cell Health Live | Dead classification (AI-driven, label-free analysis) and fluorescence classification of Cytotox positive cells. Cell image classification, evaluation of cell death time courses, and concentration response curves determining compound efficacy were used to confirm that cells exhibiting high fluorescence of Incucyte® Cytotox Dye are also being classed as dead by the Incucyte® AI Cell Health Analysis Software Module (Figure 4).

Images of HeLa cells treated with camptothecin (1.1 μM, 24 hr) with applied live (top image) and dead (bottom image) classification masks (Figure 4A) indicate a high correlation between cells which were analyzed using both label-free analysis (outline class mask) and fluorescence analysis (filled class mask). Time-course analyses of % dead cells induced by increasing concentrations of cisplatin (top graph, label-free analysis; bottom graph, fluorescence analysis) display similar time and concentration dependent responses (Figure 4B). The concentration response curves calculated using label-free and fluorescence analysis (Figure 4C).

This validation was performed across a wide range of adherent and non-adherent cell lines in monoculture and confirmed that the label-free Incucyte® AI Cell Health Analysis accurately identifies cell death induced by compounds with different efficacies and mechanisms of action.

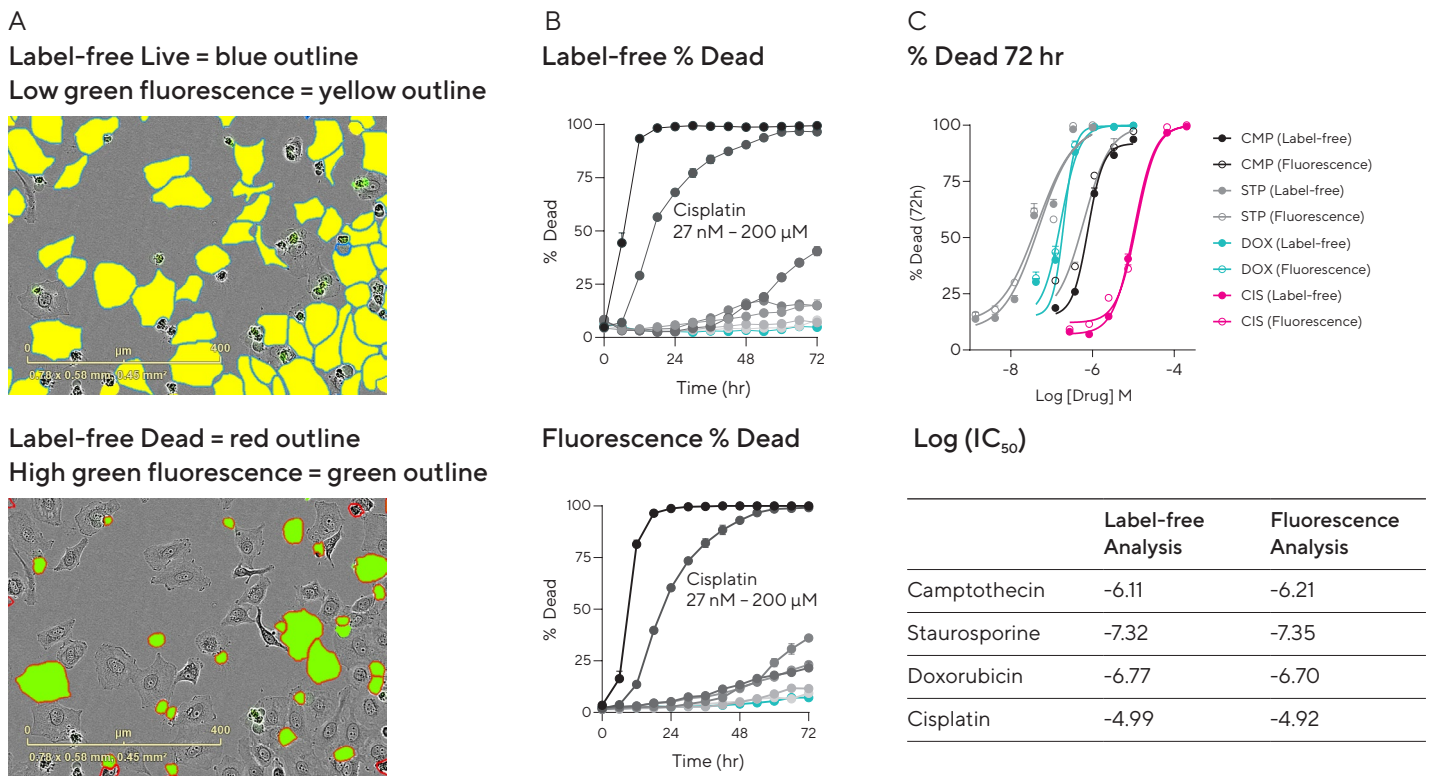


Figure 4: AI Cell Health Analysis Generates Comparable Cytotoxicity Data to Standard Fluorescence Methods.

HeLa cells were treated with concentration ranges of 4 different cytotoxic compounds in the presence of Incucyte® Cytotox Dye. Images show HeLa cells 24 hr post treatment with camptothecin. Top image (A) shows classification of live cells using Incucyte® AI Cell Health label-free analysis (blue outline) and fluorescence analysis of Cytotox Negative cells (yellow fill). Bottom image shows classification of dead cells (red outline) and cytotox positive cells (green fill) in the same image. Time courses (B) show the percentage of dead cells over time using label-free analysis (top row) or fluorescence classification (bottom row) of HeLa cells treated with increasing concentrations of cisplatin. Concentration response curves (C) plot cell death at 72 hr post treatment of camptothecin (CMP, black), staurosporine (STP, grey), doxorubicin (DOX, teal) and cisplatin (CIS, magenta). The table indicating log IC₅₀ values confirms that across compound with different mechanisms of action the efficacy values as calculated by label-free and fluorescence methods are comparable.

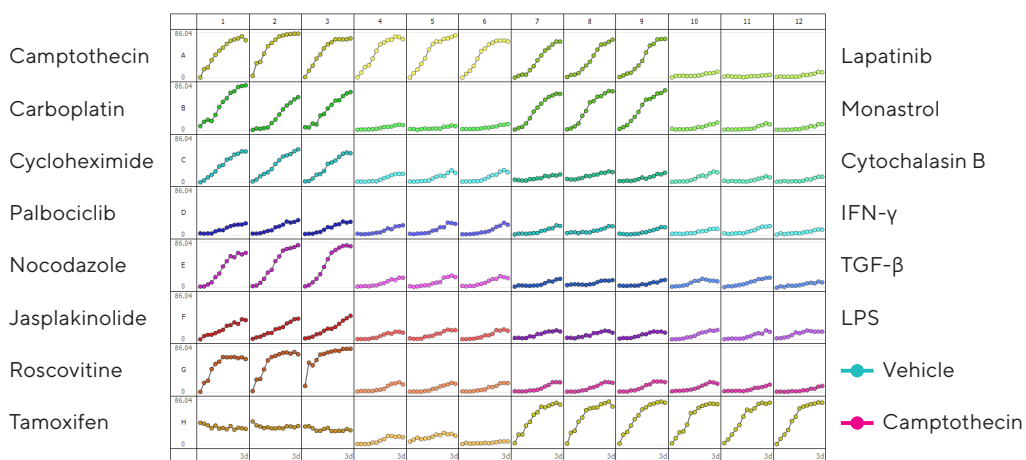
Label-Free Analysis of Cytotoxicity in Microplate Throughput

Incucyte® AI Cell Health Analysis is conducive to compound screen experiments in 96 and 384-well microplates. The highly adaptable analysis can be applied to cells with a wide range of morphologies providing directly comparable datasets, and visualization of the % dead cells per well in microplate view (Figure 5A) enables rapid and simple identification of cytotoxic compounds or conditions. End-point analysis at 48 hr post-treatment (Figure 5B) was used to confirm assay window and identify mechanisms of action between the vehicle (teal point) and positive control (high camptothecin, magenta point).

Vehicle control and similar compounds induced no inhibitory effect on cell growth (% confluence) and cell viability (% live) – these cluster in the top right of the scatter plot. Cytostatic compounds typically reduce cell growth but do not reduce cell viability – these compounds cluster in the top middle. In contrast, cytotoxic compounds reduce both cell growth and viability, clustering in the bottom left part of the plot.

A

Jurkat cells, % Dead 0 – 72 hr



B

Jurkat cells, % Live vs % Confluence, 48 hr

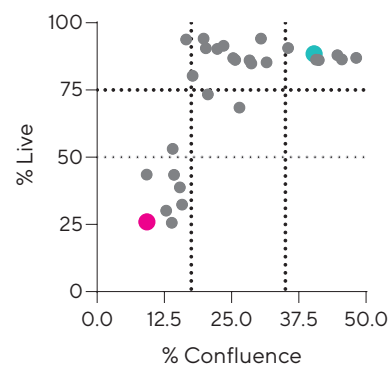


Figure 5: Analysis of Compound Effects in Non-adherent Cells.

Jurkat cells were seeded into 96-well plates coated with poly-L-ornithine and briefly centrifuged to lightly adhere to the plate surface. Cells were treated with 14 compounds in triplicate wells with high and low concentrations of each and placed into the Incucyte® to acquire phase contrast images every 2 hr for 3 days. Incucyte® AI Cell Health Analysis was used to quantify the % dead cells in each image over time (A). Mechanism of action was examined by correlating cell viability (AI Cell Health % live) with cell growth (AI Confluence) at 48 hr post treatment. Vehicle (teal) conditions displayed high viability and high growth; cytostatic compounds exhibit reduced cell growth but viability remains high; cytotoxic compounds including positive control camptothecin (10 μ M, magenta) reduce both viability and growth.

Combined Label-Free and Fluorescence Analyses Yield Additional Insight Into Mechanism of Apoptosis

Incucyte® AI Cell Health Analysis Software Module provides label-free analysis of live and dead cells, however label-free analysis also enables deeper insight into cell behavior when combined with optional fluorescence measurements. Staurosporine is known to induce cell death via both caspase-dependent and caspase-independent mechanisms. To examine these pathways, MDA-MB-231 cells were treated with staurosporine (1 μ M) in the presence of pan-caspase inhibitor Z-VAD-FMK (3 – 250 μ M). To measure caspase activation, Incucyte® Caspase 3/7

Apoptosis Dye was included. Phase contrast and fluorescence images were acquired every 2 hr for 3 days. Total cell death was quantified using Incucyte® AI Cell Health Analysis and indicated that staurosporine induced rapid cell death in the presence of all concentrations of Z-VAD-FMK (Figure 6A). Within the dead cell population, caspase activation was measured using fluorescence classification. Time course (Figure 6B) shows that the number of caspase positive dead cells decreased as the concentration of Z-VAD-FMK increased with efficacy $\log IC_{50} = -4.3$ M (Figure 6C).

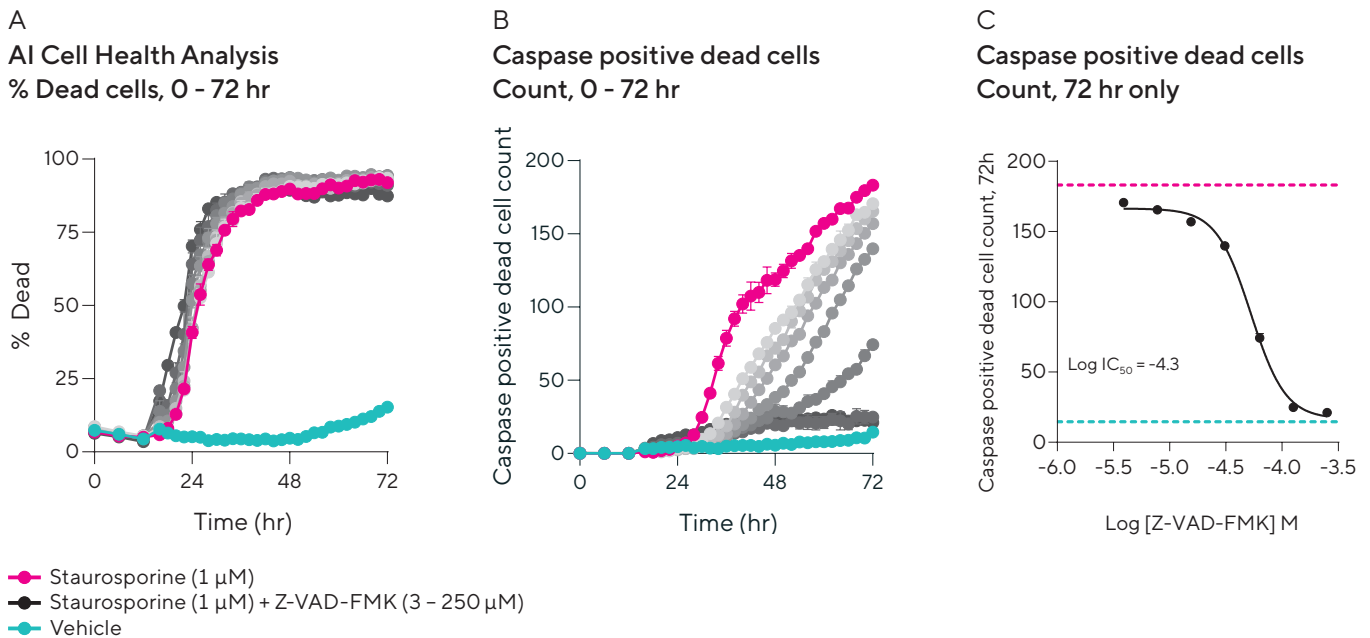


Figure 6: Label-Free Analysis With Additional Fluorescence Information Reveals Mechanisms of Apoptosis.

MDA-MB-231 cells were treated with staurosporine (1 μ M, magenta) in the presence of caspase inhibitor Z-VAD-FMK (3 – 250 μ M, grey) and Incucyte® Caspase 3/7 Apoptosis Dye. Total cell death was quantified using AI Cell Health label-free classification, and time course indicates that staurosporine induces cell death in the presence of all concentrations of Z-VAD-FMK (A). Fluorescence classification of caspase activity within the dead cell population reveals that Z-VAD-FMK reduces the number of caspase positive dead cells in a time- and concentration-dependent manner (B, C).

Summary & Conclusion

Incucyte® AI Cell Health Analysis Software Module enables accurate cell segmentation and live/dead classification. Using trained neural networks integrated into the Incucyte® live-cell analysis workflow, we have enabled user-friendly deployment of AI models for cell analysis which provide label-free quantification of cell death over time. Label-free analysis yields non-perturbing quantification of cytotoxicity which is increasingly vital when using precious patient-derived cell types. However by combining the label-free analysis with optional fluorescence readouts, additional information on the mechanisms of apoptosis can also be revealed.

References

1. Hillger, J.M., Lieuw, W.L., Heitman, L.H. & IJzerman, A.P. Label-free technology and patient cells: from early drug development to precision medicine. *Drug Discovery Today*, 22(12), 1808-1815 (2017).
2. Kusumoto, D., Yuasa, S., Fukuda, K. Induced Pluripotent Stem Cell-Based Drug Screening by Use of Artificial Intelligence. *Pharmaceuticals*, 15, 562 (2022).
3. Baens, M. et al. The dark side of EGFP: defective polyubiquitination. *PLoS ONE* 1, e54 (2006).
4. Cekanova, M. & Rathore, K. Animal models and therapeutic molecular targets of cancer: utility and limitations. *Drug Des. Devel. Ther.* 8, 1911-1922 (2014).
5. Ayers MA, Jayatunga M, Goldader J, Meier C. Adopting AI in Drug Discovery. *Boston Consulting Group*. Retrieved January 05, 2022. <https://www.bcg.com/publications/2022/adopting-ai-in-pharmaceutical-discovery>
6. Maddalena, L., Antonelli, L., Albu, A., Hada, A., Guarracino, M.R. Artificial Intelligence for Cell Segmentation, Event Detection, and Tracking for Label-Free Microscopy Imaging. *Algorithms*, 15, 313 (2022).
7. Edlund, C., Jackson, T.R., Khalid, N., Bevan, N., Dale, T., Dengel, A., Ahmed, S., Trygg, J., Sjögren, R. LIVECell: A large-scale dataset for label-free live cell segmentation. *Nat. Methods*, 18, 1038-1045 (2021).

North America

Sartorius Corporation
300 West Morgan Road
Ann Arbor, Michigan 48108
USA
Phone +1 734 769 1600
Email: lps.opm.na@sartorius.com

Europe

Sartorius UK Ltd.
Longmead Business Centre
Blenheim Road
Epsom
Surrey, KT19 9QQ
United Kingdom
Phone +44 1763 227400
Email: orderhandling.lps.ne@sartorius.com


Asia Pacific

Sartorius Singapore Pte. Ltd.
30 Pasir Panjang Road
#06-32, Mapletree Business City
Singapore 117440
Phone +65 6872 3966
Email: sartoriusap@sartorius.com

 **Find out more:** www.sartorius.com/incucyte

 **For questions, email:** AskAScientist@sartorius.com

High-resolution visualization and assessment of basal and OXPPOS-induced mitophagy in H9c2 cardiomyoblasts

Gustav Godtliebsen^a, Kenneth Bowitz Larsen^{a,b}, Zambarlal Bhujabal^a, Ida S. Opstad^c, Mireia Nager^d, Abhinanda R. Punnakkal^e, Trine B. Kalstad^d, Randi Olsen^b, Trine Lund^b, Dilip K. Prasad^e, Krishna Agarwal^c, Truls Myrmet^{a,d}, and Asa Birna Birgisdottir 

^aDepartment of Clinical Medicine, UiT-The Arctic University of Norway, Tromsø, Norway; ^bDepartment of Medical Biology, UiT-The Arctic University of Norway, Tromsø, Norway; ^cDepartment of Physics and Technology, UiT-The Arctic University of Norway, Tromsø, Norway; ^dDivision of Cardiothoracic and Respiratory Medicine, UiT-The Arctic University of Norway, Tromsø, Norway; ^eDepartment of Computer Science, UiT-The Arctic University of Norway, Tromsø, Norway

ABSTRACT

Mitochondria are susceptible to damage resulting from their activity as energy providers. Damaged mitochondria can cause harm to the cell and thus mitochondria are subjected to elaborate quality-control mechanisms including elimination via lysosomal degradation in a process termed mitophagy. Basal mitophagy is a house-keeping mechanism fine-tuning the number of mitochondria according to the metabolic state of the cell. However, the molecular mechanisms underlying basal mitophagy remain largely elusive. In this study, we visualized and assessed the level of mitophagy in H9c2 cardiomyoblasts at basal conditions and after OXPPOS induction by galactose adaptation. We used cells with a stable expression of a pH-sensitive fluorescent mitochondrial reporter and applied state-of-the-art imaging techniques and image analysis. Our data showed a significant increase in acidic mitochondria after galactose adaptation. Using a machine-learning approach we also demonstrated increased mitochondrial fragmentation by OXPPOS induction. Furthermore, super-resolution microscopy of live cells enabled capturing of mitochondrial fragments within lysosomes as well as dynamic transfer of mitochondrial contents to lysosomes. Applying correlative light and electron microscopy we revealed the ultrastructure of the acidic mitochondria confirming their proximity to the mitochondrial network, ER and lysosomes. Finally, exploiting siRNA knockdown strategy combined with flux perturbation with lysosomal inhibitors, we demonstrated the importance of both canonical as well as non-canonical autophagy mediators in lysosomal degradation of mitochondria after OXPPOS induction. Taken together, our high-resolution imaging approaches applied on H9c2 cells provide novel insights on mitophagy during physiologically relevant conditions. The implication of redundant underlying mechanisms highlights the fundamental importance of mitophagy.

Abbreviations: ATG: autophagy related; ATG7: autophagy related 7; ATP: adenosine triphosphate; BafA1: bafilomycin A₁; CLEM: correlative light and electron microscopy; EGFP: enhanced green fluorescent protein; MAP1LC3B: microtubule associated protein 1 light chain 3 beta; OXPPOS: oxidative phosphorylation; PepA: pepstatin A; PLA: proximity ligation assay; PRKN: parkin RBR E3 ubiquitin protein ligase; RAB5A: RAB5A, member RAS oncogene family; RAB7A: RAB7A, member RAS oncogene family; RAB9A: RAB9A, member RAS oncogene family; ROS: reactive oxygen species; SIM: structured illumination microscopy; siRNA: short interfering RNA; SYNJ2BP: synaptojanin 2 binding protein; TEM: transmission electron microscopy; TOMM20: translocase of outer mitochondrial membrane 20; ULK1: unc-51 like kinase 1.

ARTICLE HISTORY

Received 9 December 2022
Revised 9 June 2023
Accepted 22 June 2023

KEYWORDS

CLEM; deep learning; lysosomes; mitochondria; quality control; SIM

Introduction

Mitochondria are the main energy producing organelles in eukaryotic cells and are also central in the control of redox homeostasis, Ca²⁺ signaling, iron metabolism, innate immunity and programmed cell death [1–5]. In most cell types, mitochondria are arranged in highly dynamic networks, controlled by constant fusion and fission events [6] driven by mitochondria movements along the cytoskeleton [7]. Events such as cell cycle progression, cellular differentiation, oxidative stress, metabolic perturbation and engagement in

programmed cell death, all lead to significant alterations in the architecture of the mitochondrial network [8].

Mitochondria are dependent on oxygen for energy production in the form of adenosine triphosphate (ATP) through oxidative phosphorylation (OXPPOS). Reactive oxygen species (ROS) are formed as by-products during OXPPOS and thus mitochondria are susceptible to mitochondrial DNA mutations and protein misfolding that can ultimately lead to mitochondrial damage [9]. Damaged mitochondria result in energy-generation defects, the increased production of

CONTACT Asa Birna Birgisdottir  aasa.birna.birgisdottir@uit.no  Department of Clinical Medicine, UiT-The Arctic University of Norway, Tromsø 9037, Norway
 Supplemental data for this article can be accessed online at <https://doi.org/10.1080/15548627.2023.2230837>

© 2023 The Author(s). Published by Informa UK Limited, trading as Taylor & Francis Group.

This is an Open Access article distributed under the terms of the Creative Commons Attribution License (<http://creativecommons.org/licenses/by/4.0/>), which permits unrestricted use, distribution, and reproduction in any medium, provided the original work is properly cited. The terms on which this article has been published allow the posting of the Accepted Manuscript in a repository by the author(s) or with their consent.

harmful reactive oxygen species and can trigger programmed cell death when the damage is beyond repair. Hence, mitochondria are subjected to elaborate quality control mechanisms [10]. Damaged mitochondria can be selectively eliminated by one such mechanism, termed mitophagy, dependent on the autophagy machinery [11–13]. Mitophagy is often preceded by fission of damaged mitochondria (or parts of mitochondria) from the mitochondrial network, followed by sequestration by a double-membrane-bound autophagosome and culminates in fusion with a lysosome where the mitochondria are degraded by resident acidic hydrolases. There are multiple signaling pathways that govern autophagosome engulfment of damaged mitochondria [14].

Macroautophagy/autophagy initiation in mammalian cells is driven by the ULK1 (unc-51 like kinase 1) protein kinase complex that phosphorylates and activates key downstream mediators involved in autophagosome formation [15]. Activation and recruitment of the ULK1 complex has been implicated in mitophagy [16–19]. Autophagosome formation involves lipidation of the Atg8 (autophagy-related 8)-family proteins such as MAP1LC3B (microtubule associated protein 1 light chain 3 beta). Here, Atg8-family proteins are conjugated to phosphatidylethanolamine (PE) in the phagophore membrane, representing one of the key molecular signatures of canonical autophagy [20]. Atg8-family protein lipidation is a multistep process driven by the enzymatic activity of core autophagy proteins: the E1-like ATG7 (autophagy related 7), the E2-like ATG3 (autophagy related 3) and the E3-like ATG12–ATG5–ATG16L1 complex [21–23].

Selected cargo such as mitochondria destined for degradation are connected to the forming autophagosome through binding to Atg8-family proteins in a ubiquitin dependent or independent manner [10]. Intriguingly, non-canonical pathways, independent of ATG7 and Atg8-family protein lipidation, have also been described for lysosomal clearance of damaged mitochondria. These include alternative autophagy [24,25], microautophagy involving formation of small mitochondria derived vesicles (MDVs) [26] and degradation through the endo-lysosomal pathway involving the endosomal small GTPase RAB5A (RAB5A, member RAS oncogene family) [27]. Furthermore, non-canonical mitophagy described in mouse cardiomyocytes depends on ULK1 and the small GTPase RAB9A (RAB9A, member RAS oncogene family) [28]. Interestingly, mitochondria and lysosomes can also directly interact through the small GTPase RAB7A (RAB7A, member RAS oncogene family) [29].

The most studied ubiquitin-dependent mitophagy is known as PINK-PRKN-dependent mitophagy, orchestrated by the enzyme 3 (E3) ubiquitin ligase PRKN (parkin RBR E3 ubiquitin protein ligase) and the protein kinase PINK1 (PTEN induced putative kinase 1) [30]. Pioneering work for elucidation of PRKN-mediated mitophagy relied on induction of mitophagy by using cytotoxic agents targeting mitochondria, resulting in membrane potential dissipation of the entire network and loss of most of the mitochondria [31,32]. In contrast, basal mitophagy is considered a house-keeping mechanism where mitochondrial content is fine-tuned depending on the metabolic state of the cell [9,14]. Thus, use of mitochondria depolarizing agents is not

optimal to simulate physiological situations. Notably, the molecular mechanisms governing basal level of mitophagy in cells under physiological conditions remain mostly elusive.

In this work we set out to visualize and assess mitophagy in H9c2 cardiomyoblasts during normal culture conditions and after OXPHOS induction by galactose adaptation. We exploited H9c2 cells expressing pH-sensitive tandem mCherry-enhanced green fluorescent protein (EGFP) fluorescent mitochondrial reporters and applied state-of-the-art imaging methods for a detailed characterization of mitochondrial fragments within acidic compartments. Our results provide novel insights into the dynamics and regulation of lysosomal degradation of mitochondria in physiologically relevant settings.

Results

H9c2 cells with a pH-sensitive fluorescent mitochondrial reporter display induced formation of acidic mitochondria when adapted to galactose

In order to monitor lysosomal degradation of mitochondria in rat cardiac myoblasts (H9c2) we established stable cell lines with constitutive expression of a fluorescent (mCherry-EGFP) tandem-tagged trans-membrane (TM) domain of the outer mitochondrial membrane protein SYNJ2BP/OMP25 (synaptojanin 2 binding protein) [33–35] or tandem tagged full-length TOMM20 (translocase of the outer mitochondrial membrane 20) protein. The mitochondria thus display both green (EGFP) and red (mCherry) fluorescence and appear yellow in merged images of the green and the red channel during fluorescence imaging of the cells. The EGFP fluorescence is quenched at low pH while the mCherry fluorescence is acid stable (Figure 1A) [36]. Therefore, during imaging, mitochondria or parts of mitochondria in acidic compartments (late endosomes or lysosomes) appear as red-only structures in merged images. Under normal culture conditions, red-only dots were easily detected by fluorescence microscopy of stably transfected H9c2 cells, thus enabling monitoring of basal levels of lysosomal acidification of engulfed mitochondria (Figure 1B). In order to investigate the effect of a metabolic shift on mitochondria degradation, the cells were adapted to galactose in glucose-free growth medium for a minimum of 7 days. In this way the cells become mostly dependent on OXPHOS for ATP production [37]. As a control, the cells were kept in normal high glucose containing media for the same time-period and propagated simultaneously. The cells were then fixed and imaged by fluorescence microscopy (Figure 1B). Image analysis software was used to assess the number of cells containing red-only mitochondria as well as the number of red-only dots per cell (Figure S1A). Our data demonstrate that during normal culture conditions approximately 50% of the mCherry-EGFP-SYNJ2BP-TM cells displayed acidic mitochondria (Figure 1C). Interestingly, a significant increase in the number of cells with acidic mitochondria was detected in the galactose-adapted cells (approximately 90%) with an almost a two-fold increase in the number of red-only dots per cell (Figure 1C). Similarly, the TOMM20-mCherry-EGFP H9c2 cells displayed an increase in the number of red-

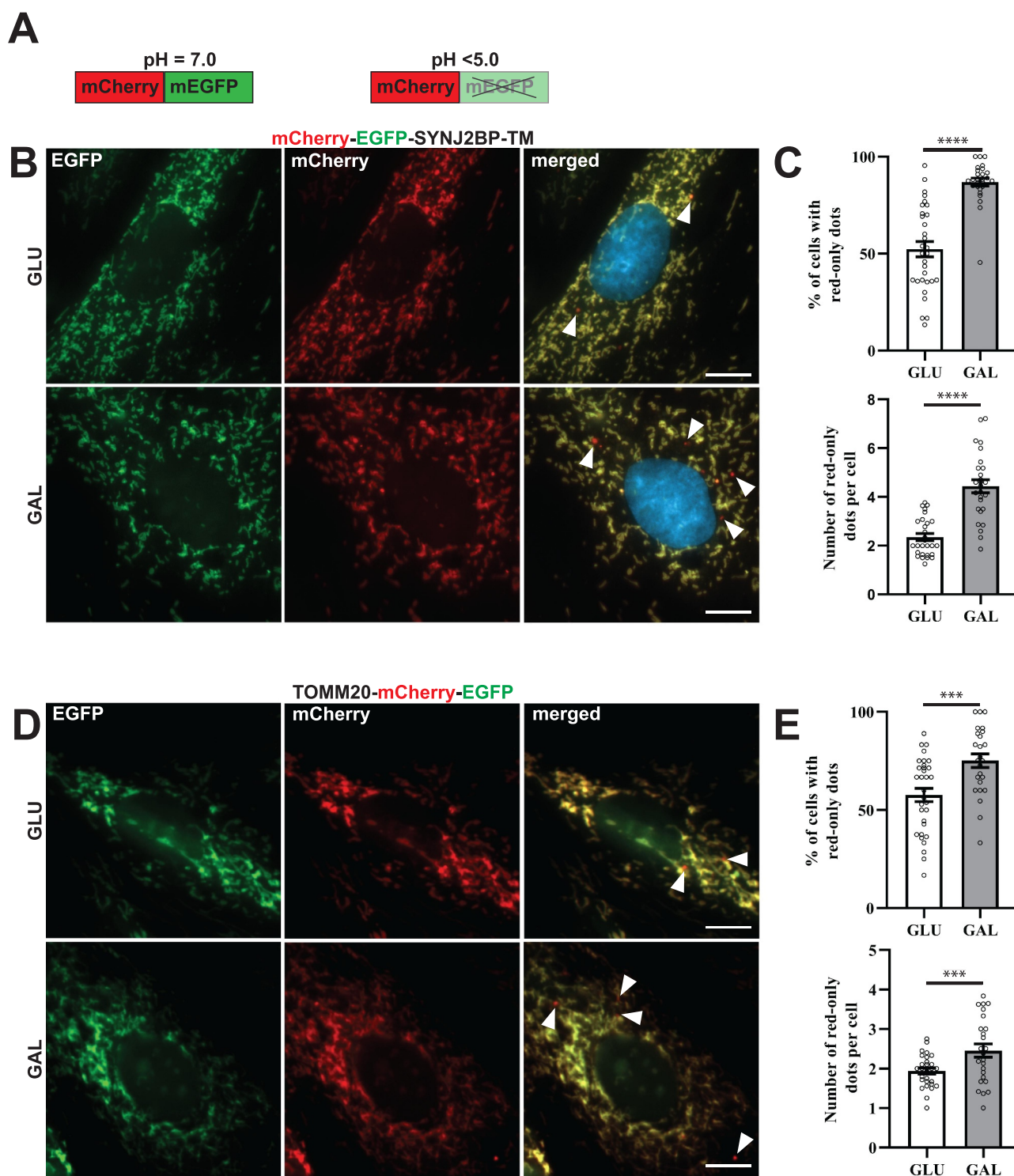


Figure 1. Reporter H9c2 cells display an increase in acidic mitochondria during galactose adaption. (A) An illustration of the pH-sensitive tandem fluorescent reporter mCherry-EGFP at different pH levels (red and green at neutral pH and red-only at acidic pH). (B) Representative widefield fluorescence microscopy images of H9c2 cells with a stable expression of the mCherry-EGFP-SYNJ2BP-TM reporter grown in glucose (GLU) or adapted to galactose (GAL) media. (C) Quantification of the percentage of cells containing red-only dots and quantification of the number of red-only dots per cell in cells with red-only dots in glucose vs galactose media for cells with the mCherry-EGFP-SYNJ2BP-TM reporter. (D) Representative widefield fluorescence microscopy images of H9c2 cells with a stable expression of the TOMM20-mCherry-EGFP reporter grown in glucose (GLU) or adapted to galactose (GAL) media. (E) Quantification of the percentage of cells containing red-only dots and quantification of the number of red-only dots per cell in cells with red only dots in glucose vs galactose media for cells with the TOMM20-mCherry-EGFP reporter. Data presented in (C) and (E) is shown as mean \pm SEM from 3 independent experiments, with more than 100 cells in each condition. The individual datapoints are per frame cell averages.

Note: * $p < 0.05$, ** $p < 0.01$, *** $p < 0.001$ and **** $p < 0.0001$. Scale bar: 10 μ m.

only dots per cell when adapted to galactose (Figure 1D,E). In comparison, 16 h of hypoxia (0.3% O₂), a well-known inducer of mitophagy [38], resulted in an equivalent increase in the number of red-only structures per cell (Figure S1B). Furthermore, using transient transfection of the pH-sensitive mt-Keima probe targeted to the mitochondrial matrix [39,40], we detected a significant increase in acidic mitochondria per cell in galactose adapted H9c2 cells (Figure S1C). To summarize, galactose adaptation of H9c2 cells induced lysosomal engulfment of mitochondria visualized by different pH-sensitive mitochondria targeted probes.

Galactose adaptation of H9c2 cells results in more fragmented mitochondria morphology, elevated mitochondrial respiration and higher susceptibility to mitochondrial damage.

Degradation of mitochondria is commonly preceded by mitochondrial fission or fragmentation [41,42]. We performed computational image analysis of mitochondrial morphology in the tandem-tagged H9c2 cells using machine learning. This enabled classification and quantification of the mitochondria morphology as networks, rods or dots as described previously [43,44]. We used confocal images of fixed mCherry-EGFP-SYNJ2BP-TM H9c2 cells grown under normal culture conditions or adapted to galactose (Figure 2A). Our computational analysis revealed that for both growth conditions, most of the mitochondria were in a network but for the galactose adapted cells the percentage was significantly lower and there were more mitochondria classified as rods and dots (Figure 2B). Furthermore, the average length of rod-shaped mitochondria as well as mitochondrial networks was significantly shorter in the galactose adapted cells (Figure 2C). Thus, our morphology analysis showed more fragmented mitochondria in galactose adapted cells. To demonstrate that galactose adaptation of the cells in fact induces OXPHOS, we characterized mitochondrial function by performing high-resolution respirometry using an Oxygraph-2k (Oroboros Instruments). Our results showed that cells adapted to galactose displayed higher mitochondrial respiration and higher ATP-linked respiration in comparison to cells under normal culture conditions, indicative of induced OXPHOS (Figure 2D). For investigation of the level of mitochondrial ROS production we applied the mitochondria-targeted superoxide indicator MitoSOX Red in H9c2 cells in glucose or adapted to galactose. This indicator gives rise to a fluorescent signal in the presence of mitochondria superoxide [45]. To measure mitochondrial ROS induction, we subjected these cells to antimycin A treatment for 4 h. Live confocal imaging of the cells (Figure S2) and Flow cytometry (Figure 2E) revealed substantially higher mitochondrial ROS production in galactose adapted cells in comparison to cells in glucose after antimycin A treatment. This demonstrates that the cells in galactose have become more dependent on their mitochondria and thus are more susceptible to mitochondrial toxicants [46]. Taken together, these results are consistent with OXPHOS-induced degradation of mitochondria after galactose adaptation as indicated by the increase in red-only structures.

Red-only structures stain positive for markers of the different mitochondrial compartments but are devoid of mitochondrial membrane potential.

To verify targeting of the mCherry-EGFP-SYNJ2BP-TM reporter to the mitochondria in H9c2 cells and to demonstrate that red-only structures contained other mitochondrial markers, we performed immunofluorescence staining with antibodies against the outer mitochondrial membrane proteins TOMM20 and FIS1 (fission, mitochondrial 1) as well as the inner membrane protein ATP5F1A/ATP5A (ATP synthase F1 subunit alpha) and the matrix protein PDHA1 (pyruvate dehydrogenase E1 alpha 1). As expected, our results showed a high degree of colocalization of the tandem-tagged reporter with all the different mitochondrial markers, indicating correct targeting of the reporter to the mitochondria (Figure 3A). In addition, several of the red-only structures stained positive for the markers of the different mitochondrial compartments, confirming the presence of mitochondrial proteins in addition to the reporter in an acidic environment (Figure 3A enlarged). For assessment of mitochondrial membrane potential, we incubated the cells with MitoTracker Deep Red and performed live confocal imaging of the cells. Interestingly, the red-only structures did not stain positive for MitoTracker Deep Red, indicating loss of membrane potential (Figure 3B). In summary, the red-only structures represent fragments of mitochondrial origin that have lost the membrane potential.

Functional lysosomes give rise to red-only structures

To study colocalization of red-only mitochondria and acidic organelles (endo/lysosomes) we utilized LysoTracker Deep Red staining of the mCherry-EGFP-SYNJ2BP-TM H9c2 cells and applied three-dimensional (3D) structured illumination microscopy (SIM) on the cells after fixation. The obtained super-resolution images clearly demonstrated the presence of the reporter on the targeted mitochondrial outer membrane (Figure 4A). Furthermore, our results showed that most of the red-only mitochondria were positive for LysoTracker Deep Red staining, indicating colocalization of red-only mitochondria and lysosomes (Figure 4Ai,ii). To establish that the increased appearance of red-only mitochondria in galactose adapted H9c2 cells was in fact dependent on low pH inside lysosomes (or late endosomes) and that the reporter responded dynamically to lysosomal pH, we subjected the galactose adapted cells to bafilomycin A₁ (BafA1) treatment for 6 h (Figure 4B). BafA1 inhibits the vacuolar type H⁺-ATPase (V-ATPase) and results in pH elevation in the lysosome lumen leading to a subsequent inhibition of resident hydrolases. In addition, BafA1 can impair fusion between autophagosomes and lysosomes [47]. As anticipated, the number of cells with red-only mitochondria as well as the number of these per cell was abolished in the presence of BafA1 (Figure 4C). In contrast, treatment with inhibitors of lysosomal cathepsins, pepstatin A (PepA) and E64d, does not affect acidification of lysosomes but hampers cargo degradation [47]. Indeed, treatment of the H9c2 cells with the cathepsin inhibitors for 6 or 12 h resulted in an increase in the number of cells with red-only mitochondria as well as the abundance of red-only dots per cell, demonstrating the importance of

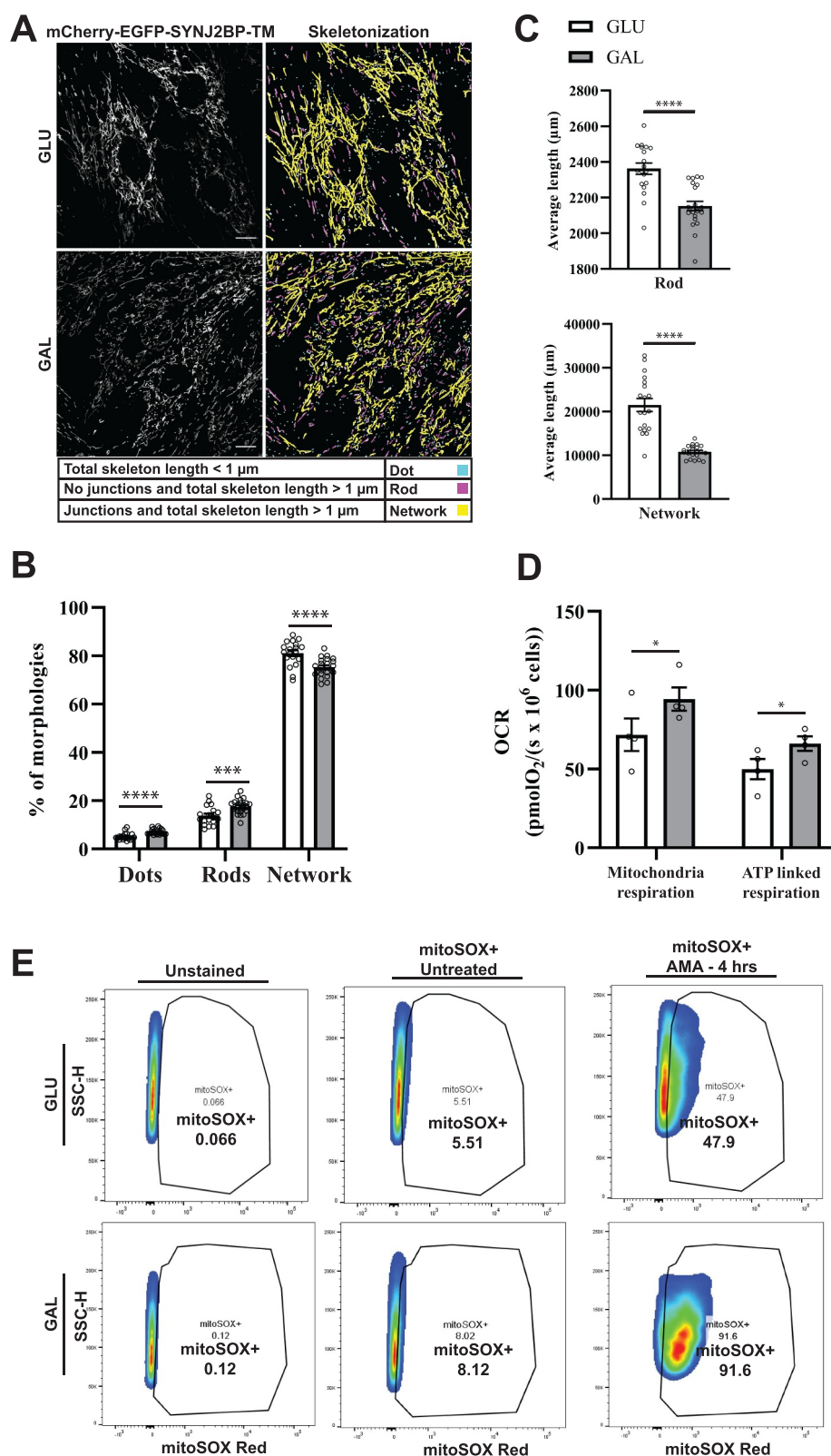


Figure 2. Mitochondria morphology analysis, mitochondrial respiration and ROS measurements indicate more fragmented mitochondria and OXPHOS dependence after galactose adaptation. (A) Morphological analysis of confocal images of cells grown in glucose vs galactose media. A representative skeletonization mask is depicted for each culture condition with the different morphology classes indicated in different colors. Rules for morphology classes are displayed at the bottom. (B) Overview of the distribution of mitochondria morphology classes in percentage for the two different growth conditions. The distribution for glucose vs galactose adaption is 5.16% vs 7.14% for dots, 13.79% vs 17.58% for rods and 81.04% vs 75.28% for network. (C) Quantification of the average length of mitochondria in the rod and network morphology classes for cells grown in glucose vs galactose. (D) High-resolution respirometry performed in an Oxygraph-2k (Oroboros Instruments). Oxygen consumption rate, OCR ($\text{pmolO}_2/\text{s} \times 10^6 \text{ cells}$) of cells grown under normal conditions (high glucose) or adapted to galactose was corrected for residual oxygen consumption (ROX) and normalized to the cell number per ml in the chambers. The values displayed in the graph are from four independent experiments \pm SEM, indicating mitochondrial respiration (basal respiration minus ROX) and ATP-linked respiration (basal respiration minus proton leak), respectively. (E) Flow cytometry analysis of H9c2 cells grown in normal media with glucose or adapted to galactose. The antimycin A (AMA) treated/untreated cells were stained with

lysosomal cathepsins in degradation of red-only dots (Figure 4D). We also demonstrated the same effect of the lysosomal inhibitors in the H9c2 TOMM20-mCherry-EGFP cells (Figure S3). Taken together, these results indicate that functional lysosomes are a prerequisite for the appearance and degradation of acidic mitochondria.

Capturing formation of acidic mitochondria by super-resolution imaging

To visualize the formation of acidic mitochondria we performed three-dimensional (3D) structured illumination microscopy (SIM) of live mCherry-EGFP-SYNJ2BP-TM H9c2 cells during normal culture conditions and in galactose adapted cells after LysoTracker Deep Red staining. Interestingly, in live videos from cells in both growth conditions (Video S1 and S2) we could detect a LysoTracker-positive structure containing a mitochondrial fragment of around 500 nm with both red and green fluorescence, indicating recent engulfment since the EGFP fluorescence was still detectable (Figure 5A,B). We identified these structures in the start of the videos and thus were unable to trace their formation back in time (Figure 5A). The majority of LysoTracker positive structures however did not contain any traces of EGFP fluorescence, possibly reflecting their more “mature” or degradative state. Notably, there is a significant time-delay between capturing the different channels during live 3D SIM imaging resulting in a slightly shifted appearance of the red and the green fluorescence of the same mitochondrial structure (Figure 5A). This makes it challenging to follow the formation of red-only structures in live SIM videos. To overcome this issue, we stained cells with LysoView 650 and used Airyscan FAST imaging to record videos at high temporal and spatial resolution (500 frames, frame time 1.01 s), without time delay between channels (Video S3–S5). As expected, we saw an almost complete overlap between LysoView 650 and red-only dots, confirming their acidic nature. Furthermore, the highly motile red-only dots were observed in close proximity with tubular mitochondria (Figure 6A). The time-lapse imaging revealed the red-only dots engaged in numerous transient contacts with the tubular mitochondria (Figure 6A, 2:34; Figure 6B, 2:19; Figure 6C, 0:24) lasting from less than 30 seconds to several minutes. Following such contacts, a mitochondrion was in some instances seen to alter its shape to become notably pulled toward red-only dots (see mitochondrion in contact with two red-only dots in the enlarged view in Figure 6C; compare timepoints around 1:00 to 2:45 in video S5). Furthermore, we observed several instances of apparent rapid transfer of material between a mitochondrion and a red-only dot (Figure 6C enlarged views from 1:36 to 2:12). Importantly, in such cases EGFP fluorescence was only briefly detectable at the intersection between the structures, suggesting uptake into an acidic

lumen and an almost instant quenching of the EGFP fluorophore. Taken together, by applying 3D SIM and Airyscan FAST live cell imaging we could capture lysosomal engulfment of mitochondrial contents.

CLEM reveals red-only structures as single membrane vesicles containing collapsed mitochondria and lamellar lysosomes

Correlative light and electron microscopy (CLEM) enables the determination of ultrastructural features of fluorescently labeled structures in a cellular context. For this type of high-resolution image analysis of the red-only dots we seeded our tandem-tagged SYNJ2BP-TM H9c2 cells grown under normal conditions or adapted to galactose on gridded dishes and stained the cells with LysoTracker Deep Red prior to fixation. Confocal imaging of the fixed cells and the grid after 4',6-diamidino-2-phenylindole (DAPI) staining allowed us to relocate the coordinates of cells of interest after resin embedding. Serial section ultramicrotomy was performed on selected positions/cells, and the sections were then imaged by transmission electron microscopy (TEM). By overlay of confocal images and TEM images we could identify red-only mitochondria positive for LysoTracker Deep Red as quite electron dense structures with features typical of autophagic vacuoles, with varying size and content in cells under normal conditions (Figure 7A). The ultrastructural characteristics of red-only dots did not seem to depend significantly on their size, since smaller red-only dots showed similar features as larger ones (Figure S4A). In contrast, mitochondria with both EGFP and mCherry fluorescence had a tubular shape and normal cristae (Figure 7A_{vi}). For the galactose adapted cells, the red-only structures were more homogenous and less electron dense (Figure 7B). Of note, when inspecting multiple consecutive sections of the same cells (Figure 7B_{iv-v}), red-only structures were frequently seen in close vicinity (or in contact) with both the tubular mitochondrial network and the ER, as well as with electron-dense structures reminiscent of lysosomes (Figure 7B_{vi}). Serial section imaging revealed the ultrastructure of these red-only/LysoTracker-positive dots as single membrane vesicles surrounding remnants of what appeared to be collapsed mitochondria (no cristae) and an electron dense multilamellar lysosome (Figure 7C). To investigate the ultrastructure of red-only dots in a state of hampered lysosomal turnover, we performed CLEM after treatment with PepA and E64d, on cells grown in both glucose and galactose (Figure S4B and S4C, respectively). As expected, we observed an increased number of red-only dots which appeared heavily aggregated and had an increased electron density after lysosomal inhibition. Our results are consistent with increased lysosomal degradation of mitochondria after galactose

mitoSOX Red and compared with unstained cells as a negative control. During normal culture conditions, antimycin A treatment resulted in approximately 47% mitoSOX Red positive cells, while in galactose 91% of the cells were mitoSOX Red positive. The data depicted represent one of three independent experiments. Data presented in (B) and (C) is shown as mean \pm SEM of 20 fields of view per condition. The individual datapoints are per frame cell averages.

Note: * $p < 0.05$, ** $p < 0.01$, *** $p < 0.001$ and **** $p < 0.0001$. Scale bar: 10 μ m.

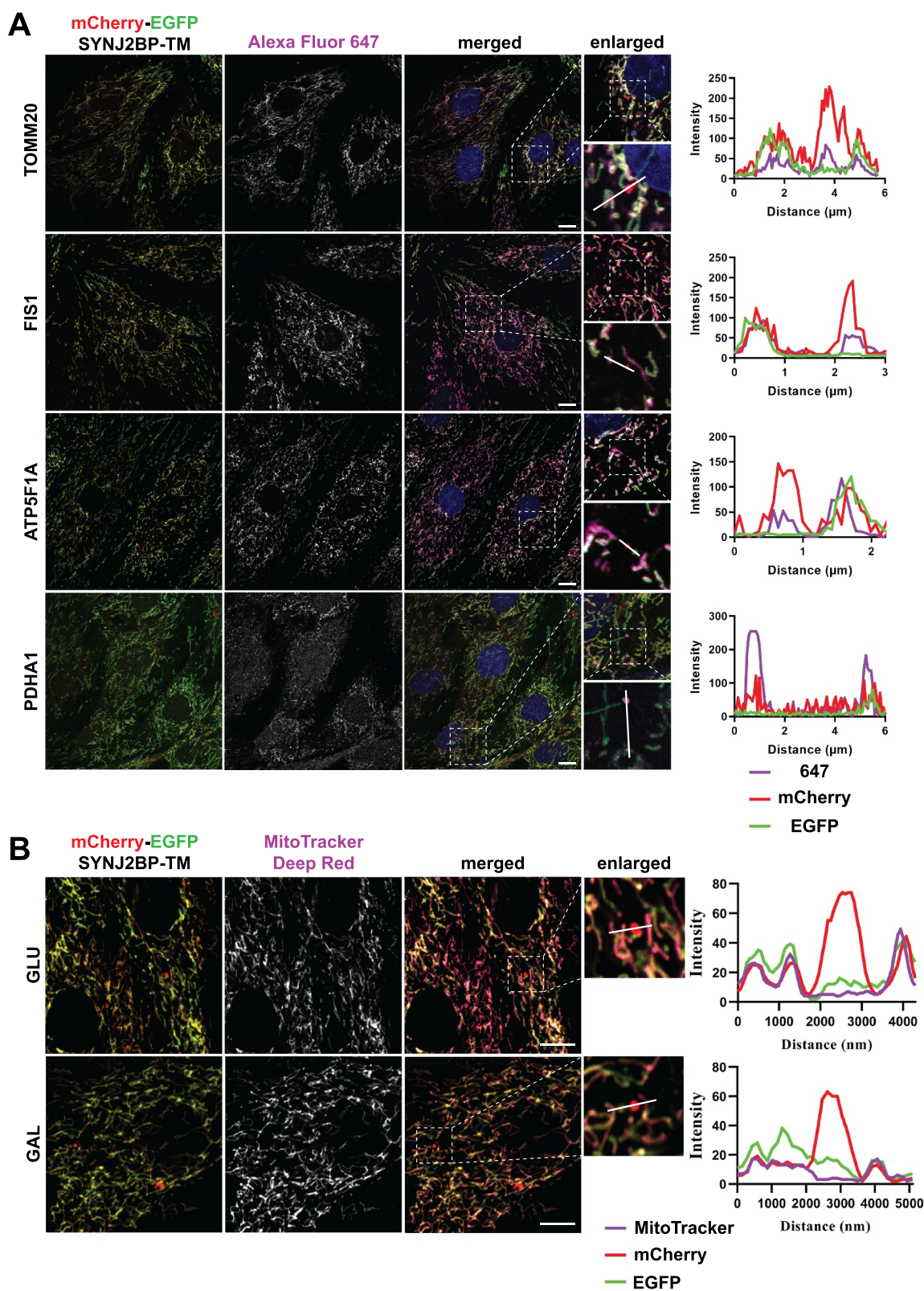


Figure 3. Red-only dots colocalize with mitochondrial markers of different mitochondrial compartments and lack membrane potential. (A) Confocal microscopy images of fixed tandem-tagged (mCherry-EGFP-SYNJ2BP-TM) H9c2 cells demonstrating colocalization of red-only dots with mitochondrial marker proteins of the different mitochondrial compartments; FIS1 and TOMM20 (outer membrane), ATP5F1 A (inner membrane) and PDHA1 (matrix). Region of interest for each marker is presented in a zoomed-in image with a line profile including an enlarged red-only dot displaying the colocalization. (B) Confocal microscopy images of live H9c2 cells with the mCherry-EGFP-SYNJ2BP-TM reporter and MitoTracker Deep Red staining for both glucose and galactose adapted cells. The enlarged region of interest depicts line profiles demonstrating colocalization of MitoTracker Deep Red in mitochondrial networks, but lack of colocalization in red-only dots. Scale bar: 10 μm .

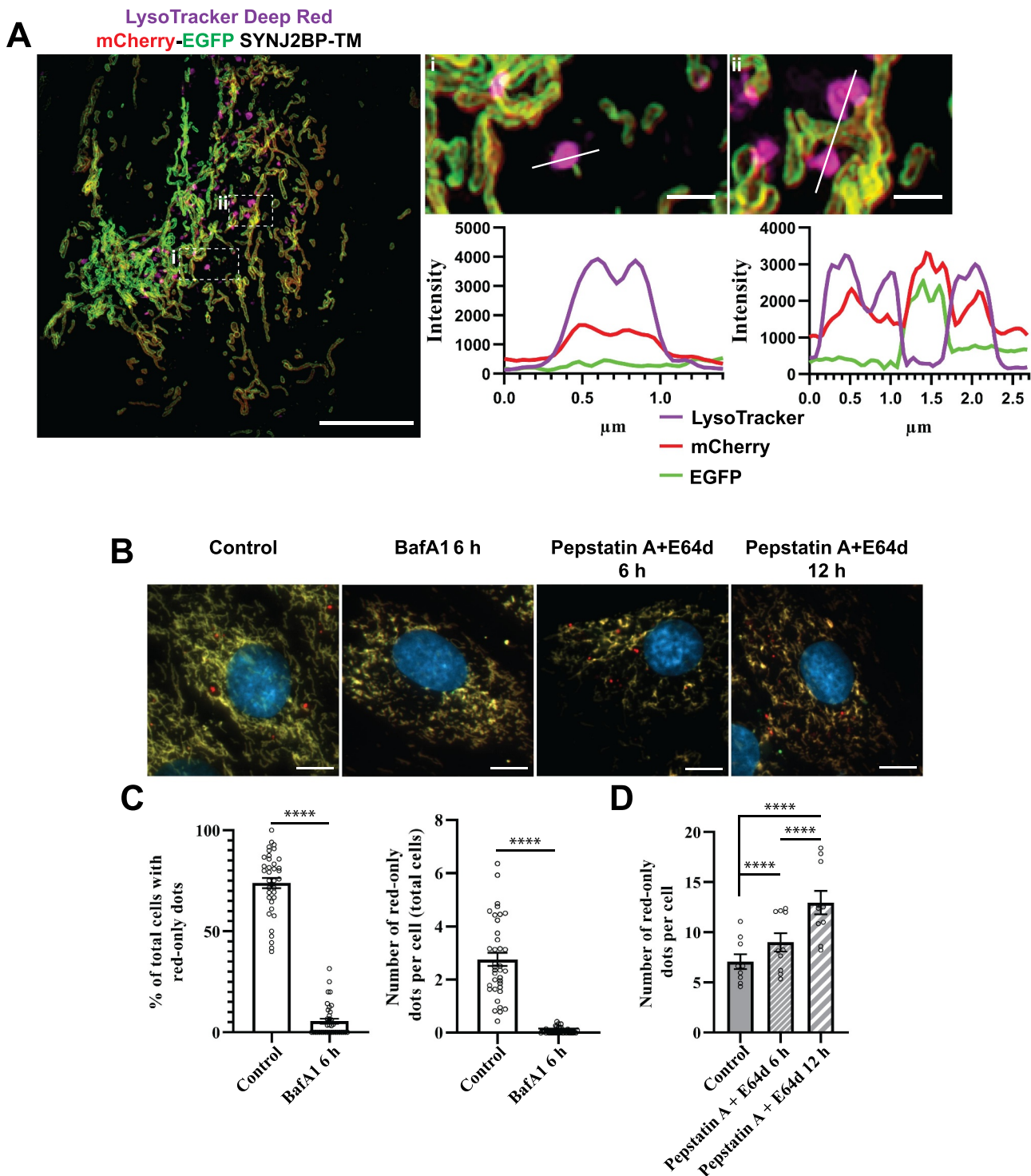


Figure 4. Functional lysosomes are essential for the appearance and removal of red-only dots during galactose adaption. (A) Structured illumination microscopy (SIM) imaging of fixed mCherry-EGFP-SYNJ2BP-TM H9c2 cells showing red-only dots that are positive for LysoTracker DeepRed staining (magenta). Line profiles through the LysoTracker-positive red-only dots in the enlarged boxed regions of interest are depicted, with corresponding numbers between the overview image and enlarged images. (B) Representative images of galactose adapted mCherry-EGFP-SYNJ2BP-TM H9c2 cells during control conditions and after treatment with the lysosomal inhibitors bafilomycin A₁ (BafA1; 200 nM) and pepstatin a (PepA; 10 µg/ml) and E64d (10 µg/ml) for the indicated times. (C) Quantification of the effects of a 6 h treatment of BafA1 on galactose adapted cells with the mCherry-EGFP-SYNJ2BP-TM reporter by assessing the percentage of cells containing red-only dots and number of red-only dots per total cells. (D) Quantification of the effects of a time course treatment of PepA and E64d assessed by number of red-only dots per cell in cells with red-only dots in galactose adapted cells with the mCherry-EGFP-SYNJ2BP-TM reporter. Over 150 cells were analyzed for each condition. The data is presented as mean ± SEM from 3 independent experiments, with more than 100 cells per condition. The individual datapoints are per frame cell averages. NOTE: * $p < 0.05$, ** $p < 0.01$, *** $p < 0.001$ and **** $p < 0.0001$. Scale bars: 10 µm and 1 µm (Ai and Aii).

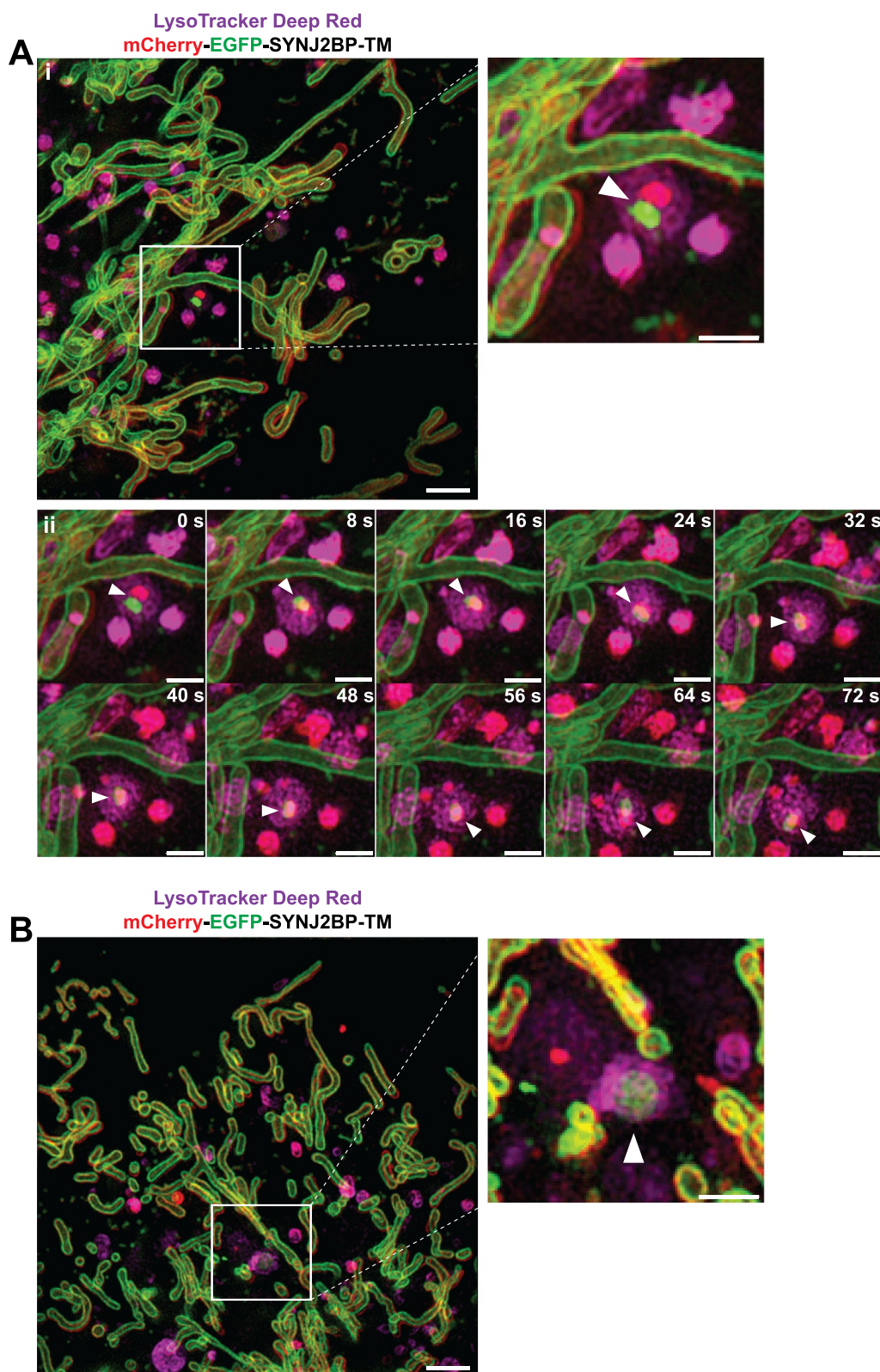


Figure 5. Three-dimensional (3D) structured illumination microscopy (SIM) live cell imaging of mCherry-EGFP-SYNJ2BP-TM H9c2 cells captures mitochondrial fragments within acidic structures. (Ai) A still frame overview image (merged channels) from the start of Video S1 displaying a cell during normal culture conditions after adding the LysoTracker Deep Red dye (100 nM for 40 min). The boxed area indicates a mitochondrial fragment with both EGFP and mCherry fluorescence inside a LysoTracker Deep Red-positive structure. The channels for red and green fluorescence are slightly shifted due to the time-delay between images of the different channels. The region of interest is shown as an enlarged image and the structure is highlighted with an arrowhead. (Aii) A time series of the boxed area in Video S1 following the movement of the lysosome containing the mitochondrial fragment (arrowhead). (B) A still frame overview image (merged channels) from the start of Video S2 displaying a cell after galactose adaptation after adding the LysoTracker Deep Red dye (100 nM for 40 min). The boxed area indicates a mitochondrial fragment with both EGFP and mCherry fluorescence inside a LysoTracker Deep Red-positive structure. The region of interest is shown as an enlarged image with the identified structure highlighted with an arrowhead. Max projection was utilized for all the images. Scale bars: 2 μm (overview images) and 1 μm (the enlarged images and for the time series).

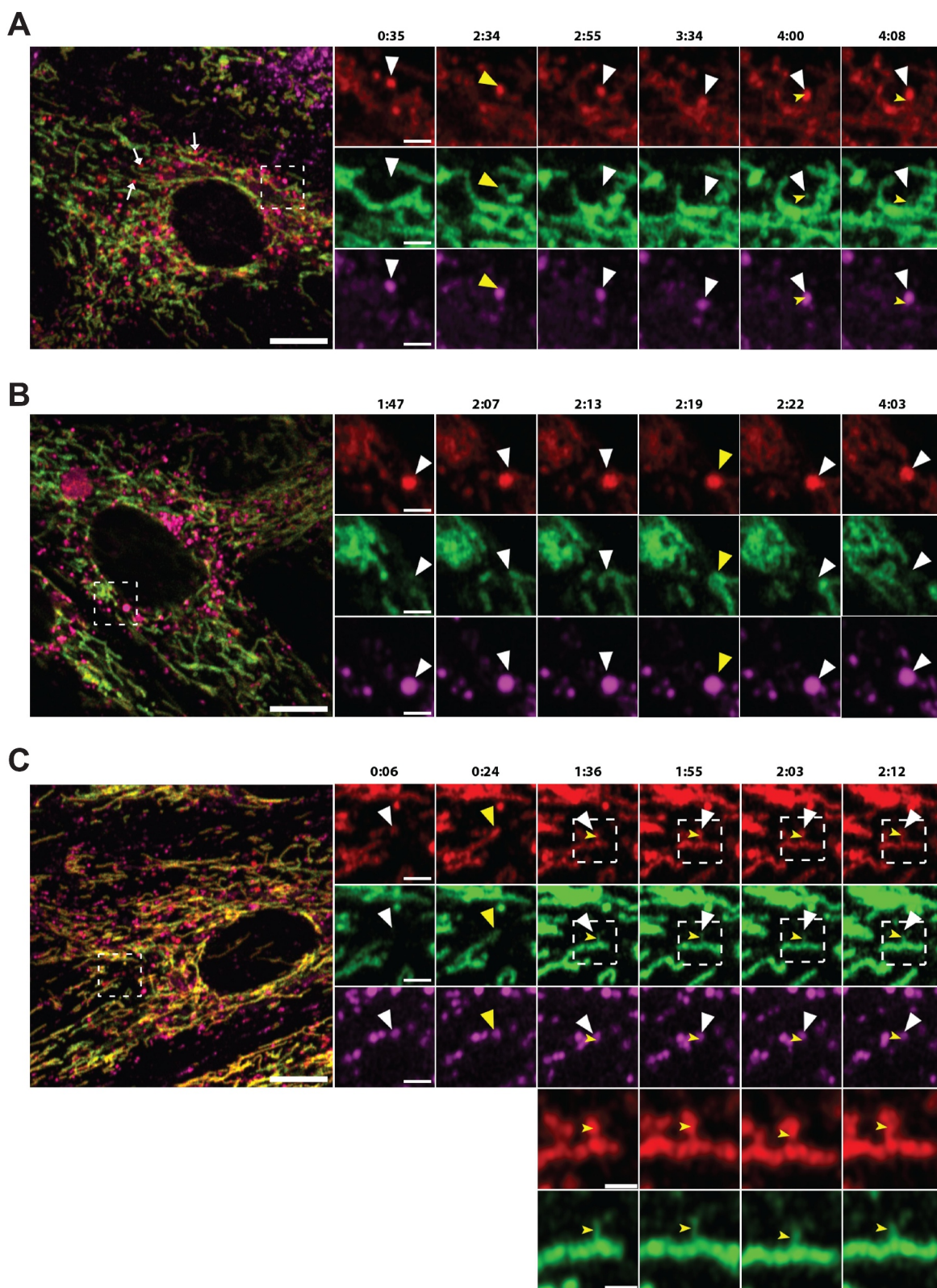


Figure 6. Airyscan FAST imaging of live galactose adapted mCherry-EGFP-SYNJ2B-TM H9c2 cells stained with LysoView 650 reveals transient contact and transfer between the mitochondrial network and red-only dots. (A) Full frame of video S3 at time 0:35 with zoomed-in area indicated (white box) for the selected time points (small panels, right). White arrows in the full frame show examples of red-only dots in close proximity with tubular mitochondria. White arrowheads in the small panels highlight a red-only dot approaching and contacting the mitochondrial network, producing a brief colocalized signal (yellow arrowheads) around time 2:34. At time 2:55, EGFP fluorescence has diminished, and the structure again appears red-only (white arrowheads). In subsequent frames, small protrusions of EGFP fluorescence (notched yellow arrowheads) can be seen upon close inspection to extend from the mitochondrion and into the red-only dot, and then rapidly disappear (see also video S3). (B) Full frame of video S4 at time 1:47 with zoomed-in area indicated (white box) as in (A). White arrowheads indicate a red-only dot approaching the mitochondrial network from time point 2:07. The EGFP signal remains detectable within the red-only dot for a few seconds around time 2:19 (yellow arrowheads) and then disappears around time point 2:22 (see also video S4). (C) Full frame of video S5 at time 0:06 with zoomed-in area indicated (white box) as in (A) and (B). White arrowheads indicate a red-only dot which encounters a tubular mitochondrion from time point 0:24 (yellow arrowheads). In subsequent frames, small protrusions of EGFP fluorescence can be seen to extend into the red-only dots (notched yellow arrowheads at time 1:36, 1:55, 2:03, and 2:12). An enlarged partial view (white boxes) of the mCherry and EGFP channels is shown below each time point. Scale bars: 10 μm (full frames), 2 μm (small panels), and 1 μm (enlarged views).

adaptation and demonstrate the importance of imaging serial sections when characterizing ultrastructural features.

Knockdown of Ulk1, Atg7 or Rab9a, respectively, impacts on OXPPOS induced lysosomal degradation of mitochondria.

In an attempt to elucidate the mechanism(s) driving lysosomal degradation of mitochondria induced by galactose adaptation in H9c2 cells, we performed short interfering RNA (siRNA) knockdown of selected key genes involved in autophagic or endosomal degradation of mitochondria in cardiac cells: *Atg7* (canonical autophagy machinery) [48], *Rab9a* (alternative mitophagy) [28], *Ulk1* (upstream of both ATG7 and RAB9A) [15,28] as well as *Rab5a* (endosomal mitophagy) [27]. We also knocked down *Rab7a*, the small GTPase involved in direct contact between mitochondria and lysosomes [28]. We chose a knockdown strategy with siRNA due to difficulties in generating CRISPR-Cas9 knockouts in H9c2 cells as also previously reported [49]. The cells were subjected to 48 h of siRNA knockdown and grown with or without the lysosomal cathepsin inhibitors PepA and E64d during the final 12 h. After fixation, the cells were analyzed by fluorescence microscopy (Figure 8A). The use of PepA and E64d enabled us to assess perturbation of autophagic flux resulting from siRNA knockdown by quantifying red-only dots (Figure 8B). The knockdown of each protein was verified with western blots of cell lysates from cells adapted to galactose (Figure 8C). The abundance of red-only dots was quantified and compared with cells treated with PepA and E64d. Surprisingly, siRNA knockdown of neither *Ulk1*, *Atg7*, *Rab9a*, *Rab5a* nor *Rab7a* affected the number of red-only dots per cell during steady-state conditions. However, knockdown of *Ulk1*, *Atg7* and *Rab9a* led to an impaired flux, demonstrated by a lack of an increase in red-only dots after PepA and E64d treatment (Figure 8B). This did not apply to siRNA knockdown of *Rab5a* or *Rab7a* where the flux was unaffected. Our data thus show the importance of using lysosomal inhibitors when evaluating the effects of siRNA knockdowns on OXPPOS induced degradation of mitochondria. Prolonging the PepA and E64d treatment from 12 to 24 h did not uncover any further increase in the level of red-only dots (Figure S5A). Likewise, extending the siRNA knock-down to 72 h did not alter mitochondrial protein expression levels (Figure S5B). To further investigate the importance of the canonical autophagy machinery we monitored the presence of the autophagy marker MAP1LC3B on mitochondria and on red-only dots. To this end, we performed a proximity ligation assay (PLA) [50] using anti-MAP1LC3B antibody in combination with anti-PDHA1 antibody. This assay enables the assessment of proximity of the two targeted proteins in situ in fixed cells, giving rise to a fluorescent PLA signal or puncta only when the targeted proteins are within 40 nm of each other. The PLA puncta were localized on mitochondria, both networks and smaller structures, but were not present on red-only dots (Figure 8D). Notably, there was no increase in the number of PLA puncta per cell in galactose adapted cells compared to

cells in normal glucose containing conditions (Figure 8E). This suggests the presence of MAP1LC3B on mitochondria before acidification but also indicates that MAP1LC3B is not the main mediator of enhanced mitochondrial degradation in galactose adapted cells. In conclusion, our data indicate the involvement of both ULK1, ATG7 and RAB9A in lysosomal degradation of mitochondria in H9c2 cells. In contrast, RAB5A and RAB7A do not seem to play a major role.

Discussion

Given the central role of mitochondria in cell homeostasis, maintaining functional mitochondria is crucial. Basal levels of mitophagy have been considered too low for a reliable assessment [47]. Interestingly, use of pH-sensitive mitochondria reporters such as mt-Keima and *mito-QC* reveal a substantial but heterogenous level of basal mitophagy in tissues of mice and flies [51–56] and a detectable level in *C. elegans* and zebrafish [57]. Since the fraction of mitochondria targeted for lysosomal degradation at any given time under normal conditions is likely small compared to the total pool of mitochondria within the cell, such sensitive reporters are crucial to detect the degradation. The *mito-QC* reporter has been used in H9c2 cardiomyoblasts to display induced mitophagy during cell differentiation [49]. We exploited a similar dual color fluorescence-quenching assay based on a mCherry-EGFP outer mitochondrial membrane targeted reporter to detect lysosomal degradation of mitochondria in H9c2 cells. Our quantification of basal mitophagy in H9c2 cells showed a high percentage (around 50%) of cells containing red-only mitochondria. This is substantially higher than reported for e.g., human neuroblastoma SH-SY5Y cells [58] and mouse embryonic fibroblasts [59,60] where less than 20% of the cells display red-only mitochondria. Notably, the number of acidic mitochondrial structures detected per cell (around 3–4) of H9c2 cells with red-only dots was similar as to that reported for SH-SY5Y cells and human retinal pigment epithelial ARPE-19 cells [61]. By employing a metabolic shift to OXPPOS by galactose adaptation we detected a significant increase in both the number of cells containing acidic mitochondria as well as the number of red-only dots per cell. Our results are in line with studies on OXPPOS-induced mitophagy in mouse endothelial fibroblasts (MEFs) [59] as well as in HeLa cells and human primary skeletal muscle myoblasts [62]. In addition, piecemeal mitophagy of specific mitochondrial proteins is OXPPOS induced in HeLa cells [63] and in MEFs [60]. Most likely the induced removal of mitochondria or mitochondrial proteins is due to higher turnover of the mitochondria during elevated activity of the electron transport chain. This would sustain renewal of mitochondria and avoid accumulation of damaged organelles. In support of this, we have previously shown an increased formation of mitochondria derived vesicles in galactose adapted H9c2 cells [35]. Conversely, OXPPOS dependence blocks iron chelator-induced mitophagy in human bone osteosarcoma U2OS cells and SH-SY5Y cells [58] and Carbonyl cyanide 3-chlorophenylhydrazone (CCCP) depolarization-induced mitophagy in neurons and HeLa cells [64–67]. Hence, the

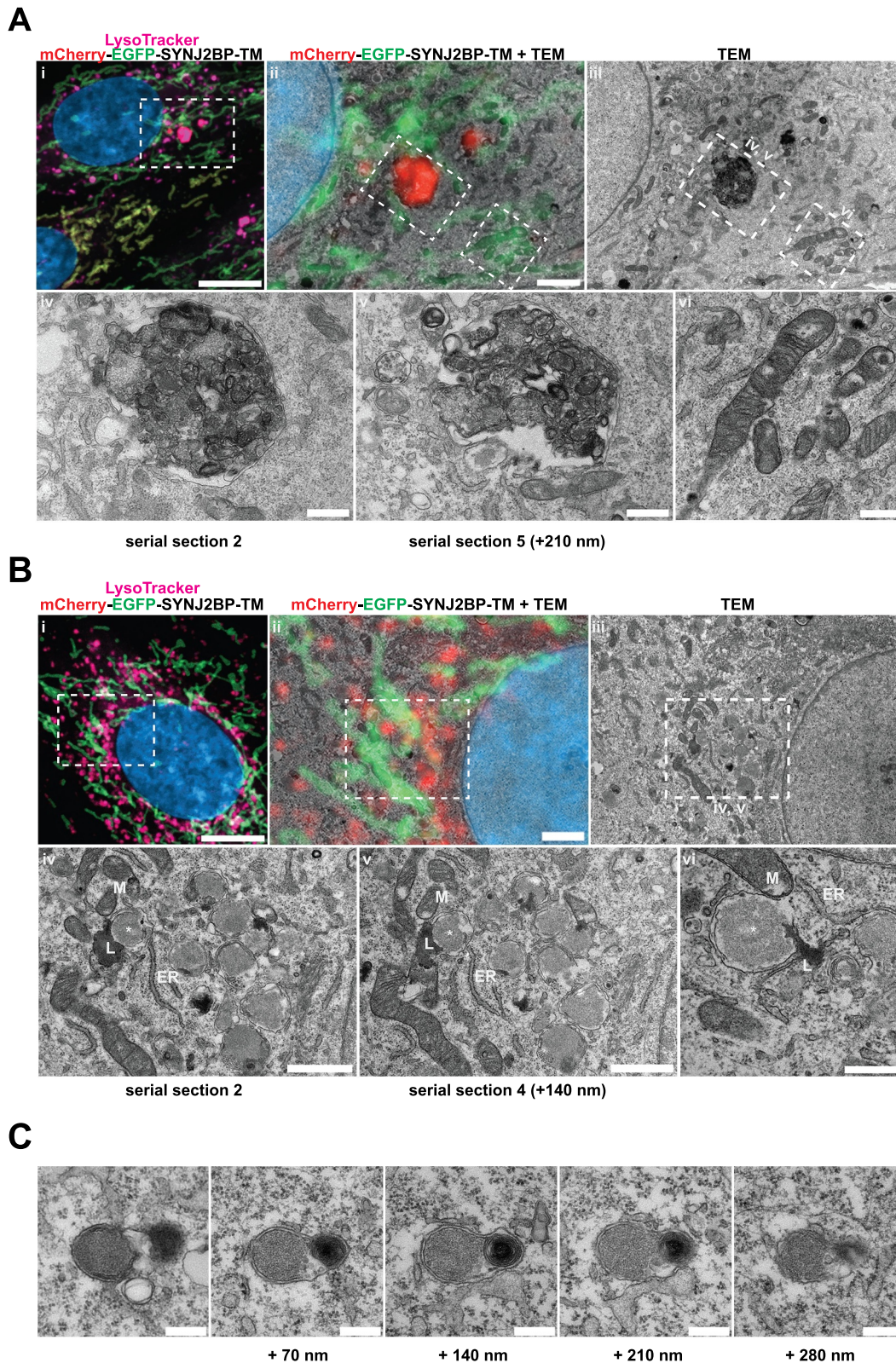


Figure 7. Correlative light and electron microscopy of mCherry-EGFP- SYNJ2BP-TM H9c2 cells reveals the ultrastructure of red-only dots. (A) Red-only dots in cells grown in media containing glucose correspond to autophagic vacuoles with a diverse internal milieu at varying stages of cargo engulfment and maturation (A iv-v). Meanwhile, mitochondria displaying both EGFP and mCherry fluorescence have a normal tubular morphology with distinct inner and outer membranes and intact cristae (A vi). (B) Structures corresponding to red-only dots in galactose adapted cells are more uniform and less electron dense. Imaging of consecutive ultrathin sections (B iv-vi) revealed that these structures are in close proximity (or may be continuous) with membranes of the endoplasmic reticulum (ER) and mitochondria (M). Also note apparent lysosomes (L) at the periphery of red-only structures (*). Scale bars: 10 μm (A i and B i), 2 μm (A ii and B ii), 1 μm (B iv and B v) and 0.5 μm (A iv-vi and B vi). (C) Serial section TEM imaging of a red-only dot shows a single membrane vesicle with apparent remnants of mitochondria and a multilamellar lysosome. Scale bar: 0.3 μm .

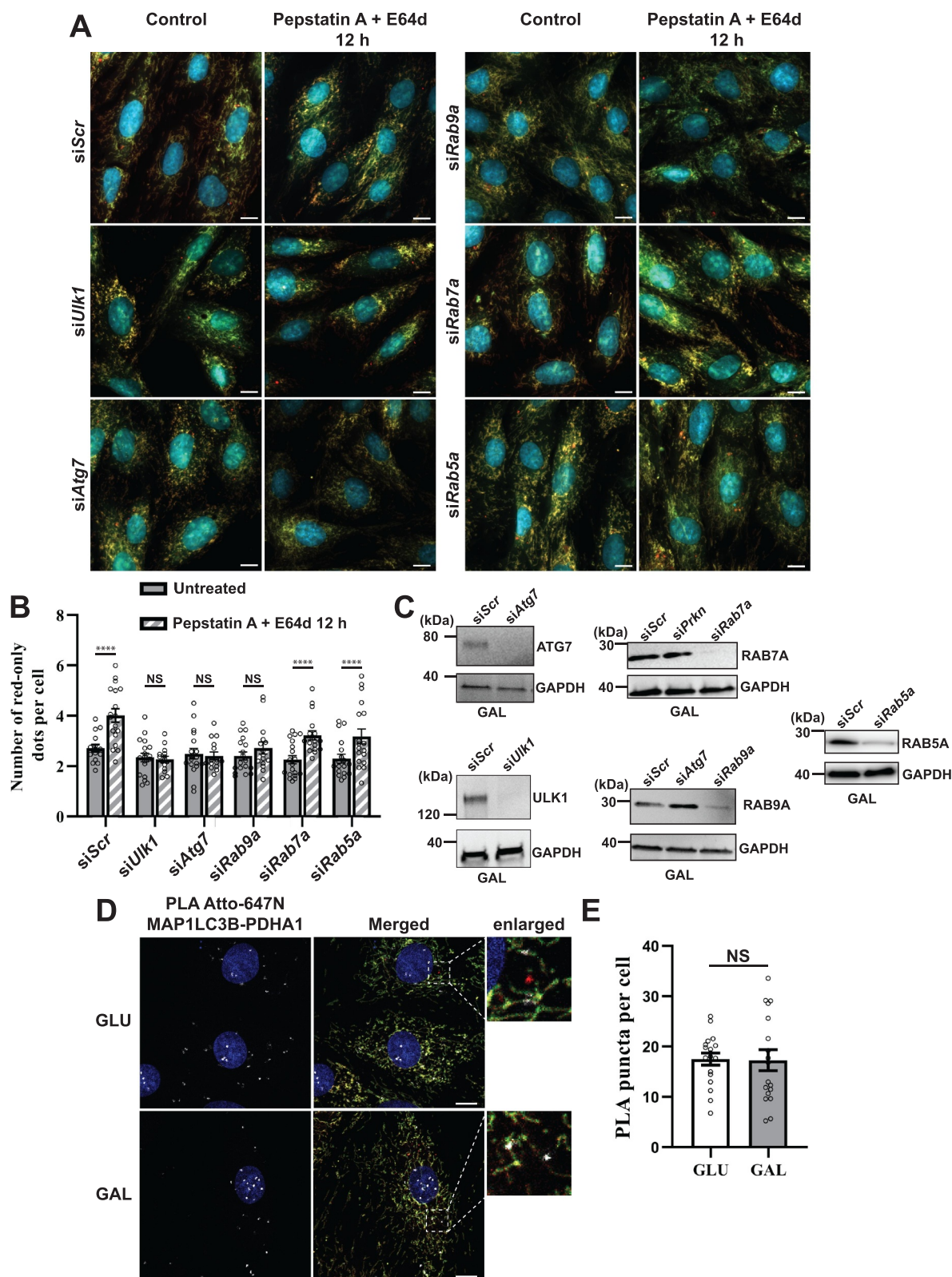


Figure 8. Effect of siRNA knockdowns on mitophagic flux and evaluation of LC3 involvement by proximity ligation assay (PLA). (A) Representative widefield images of mCherry-EGFP- SYNJ2BP-TM H9c2 cells analyzed 48 h after transfection with scrambled siRNA (siScr) or siRNA against *Ulk1*, *Atg7*, *Rab9a*, *Rab7a* or *Rab5a* respectively. (B) Quantification of the effect of 48 h siRNA knockdowns by assessment of number of red-only dots per cell in cells containing red-only dots in control conditions against a 12 h PepA and E64d treatment. The data is presented as mean \pm SEM from 3 independent experiments, with more than 100 cells per condition (total number analyzed per experiment was over 1200 cells). (C) Western blots showing the expression levels of the siRNA targeted proteins in control and siRNA treated cells for verification of successful knockdown. (D) Representative confocal images of detected PLA puncta (white) using anti-MAP1LC3B and anti-PDHA1 antibody during normal (GLU) and galactose (GAL) adapted conditions. The enlarged boxes display the PLA puncta on the mitochondria network and small mitochondrial fragments but their absence on red-only dots. (E) Quantification of the number of PLA puncta per cell in 10 images (with more than 50 cells in total) per condition from two independent experiments. The individual datapoints are per frame cell averages. * $p < 0.05$, ** $p < 0.01$, *** $p < 0.001$ and **** $p < 0.0001$. Scale bar: 10 μ m.

metabolic status of the mitochondria can dictate the level of mitophagy, dependent on the cell type and growth conditions. Interestingly, a recent study suggests that mitophagy itself initiates an increase in mitochondrial biogenesis and oxidative metabolism in induced pluripotent stem cells undergoing endothelial differentiation [68].

Using a deep-learning approach we were able to quantify the morphological change of mitochondria in H9c2 cells, adopting a more fragmented or shorter appearance after the metabolic shift. Mitochondrial fragmentation has also been observed in neonatal cardiomyocytes where the percentage of mitochondria with shorter lengths increases during glucose deprivation by galactose adaptation [28]. Mitochondrial fragmentation is often mediated by peripheral fission which is mechanistically different from mid-zone fission directing mitochondria biogenesis [42]. In green monkey kidney fibroblast-like Cos-7 cells the smaller peripheral fission-derived mitochondria display a length distribution of only 1–2 μm and are mainly subjected to degradation. In addition, the rate of peripheral fissions per cell increases when the Cos-7 cells are grown in glucose-free, galactose containing media [42].

Performing super-resolution live cell imaging on tandem tagged SYNJ2BP-TM H9c2 cells with labeled lysosomes, we were able to monitor highly dynamic interactions between lysosomes and mitochondria. Furthermore, we detected rapid lysosomal engulfment of mitochondrial contents within a few minutes. The rapid formation of these structures could also indicate their rapid degradation and thus influence the numbers of such events detected in snapshots of fixed cells. The potential consequence could therefore be an underestimation of the levels of lysosomal degradation of mitochondria when studying fixed cells and tissue. We are not aware of previous publications demonstrating super-resolution live cell imaging of the formation of acidic mitochondria.

Applying CLEM, we revealed the ultrastructure of red-only mitochondria in the H9c2 cells in steady-state conditions and after a metabolic shift toward OXPHOS. There are only a few studies that have performed CLEM analysis on acidified mitochondria. The ultrastructures of mt-Keima acidic dots analyzed by CLEM in *Drosophila* muscle cells also contain features of multilamellar bodies and are of a comparable size as those detected in the H9c2 cells [55]. In studies performed in mammalian cells, iron depletion with DFP [57,67] or stress induced with propionic acid [69] or CCCP and overexpression of PRKN [70] are used to induce degradation of mitochondria before the CLEM analysis. Thus, to our knowledge, our study is the first to visualize the ultrastructure of acidified mitochondria in mammalian cells cultured under physiologically relevant conditions. Taken together, in view of our results from live cell SIM and Airyscan FAST imaging, the CLEM data presented are consistent with a model where mitochondria are fragmented at (or in close vicinity to) the ER, and rapidly fuse with lysosomes.

There are still many unanswered questions regarding the molecular mechanisms of basal mitophagy. Notably, pH-dependent mitochondrial reporters indicate acidification of tagged mitochondria or parts of mitochondria and thus their presence in acidic late endosomes or lysosomes. However, the

route of the labeled mitochondria toward lysosomes is not revealed by the reporters. We chose siRNA knockdown of *Ulk1*, *Atg7*, *Rab9a* to assess the contribution of both canonical and non-canonical autophagy in lysosomal degradation of mitochondria in the H9c2 cells. Knockdown of neither *Ulk1*, *Atg7* nor *Rab9a* reduced the level of red-only dots in galactose adapted cells. However, these siRNA experiments resulted in hampered mitophagic flux, revealed using lysosomal inhibitors. Therefore, our data indicate the presence of redundant mechanisms for lysosomal degradation of mitochondria in H9c2 cells where both the canonical autophagy machinery and alternative RAB9A mediated mitophagy operate during OXPHOS reliant conditions. In addition, because of the unaffected basal level during all knockdown experiments, other mechanisms such as different types of micromitophagy [26] could be involved and require further investigations.

Our study shows that assessment and visualization of lysosomal degradation of mitochondria at high temporal and spatial resolution is feasible during basal conditions. Our results indicate highly dynamic interactions and transfer of material between mitochondria and lysosomes and give important insights that are valuable for future studies and therapeutic targeting of mitophagy.

Materials and methods

Cell culture

Rat cardiomyoblast H9c2 cells (Sigma-Aldrich, 88092904) were cultured in high-glucose (4.5 g/L) Dulbecco's Modified Eagle Medium (DMEM; Sigma-Aldrich, D5796) with 10% Fetal Bovine Serum (FBS) and 1% streptomycin/penicillin (Sigma-Aldrich, P4333). For glucose deprivation and adaptation to galactose, the cells were grown in DMEM without glucose (Gibco, 11966-025) supplemented with 2 mM L-glutamine (Sigma-Aldrich, G7513) 1 mM sodium pyruvate (Sigma-Aldrich, S8636), 10 mM galactose (Sigma-Aldrich, G5388), 10% fetal bovine serum (Sigma-Aldrich, F7524) and 1% streptomycin-penicillin (Sigma-Aldrich, P4333). The cells were adapted to galactose for at least 7 days before the experiments. Stable H9c2 cells (see below) were grown in the same medium with the addition of 1 $\mu\text{g}/\text{ml}$ of puromycin (InvivoGen, ant-pr-1). For hypoxic conditions, the cells were incubated at 0.3% O_2 for 2, 4, 6 or 16 h. For labeling of lysosomes, the cells were treated with 50 or 100 nM LysoTracker Deep Red (ThermoFisher Scientific, L12492) for 30–40 min or with LysoView 650 (Biotium, 70059). Cells were treated as indicated with 0.2 μM bafilomycin A₁ (BafA1 from *Streptomyces griseus*; Sigma-Aldrich, B1793) or 10 $\mu\text{g}/\text{ml}$ pepstatin A (Sigma-Aldrich, P5318) and 10 $\mu\text{g}/\text{ml}$ E64d (Sigma-Aldrich, E8640). All cell lines were maintained at 37°C and under 5% CO_2 .

Generation of stable mCherry-EGFP-SYNJ2BP-TM and TOMM20-mCherry-EGFP H9c2 cell lines

H9c2 cells with stable expression of tandem tagged (mCherry-EGFP) mitochondria

outer membrane protein SYNJ2BP/OMP25 (synaptojanin 2 binding protein)-transmembrane domain (TM) or tandem-tagged (C terminus) full length TOMM20 protein were generated by retroviral transduction. The mCherry-EGFP-SYNJ2BP-TM construct [32] was amplified with PCR and cloned into the retroviral expression vector pMRXIP with the selection marker puromycin. The vector was made with deletion of GFP-STX17 from the pMRXIP-GFP-STX17 plasmid (Addgene, 45909; Noburo Mizushima lab). Full-length TOMM20 was amplified by PCR using mTagBFP2-TOMM20-N-10 plasmid (Addgene, 55328; Michael Davidson lab) as a template and cloned into the pMRXIP vector with the tandem tag. The plasmids were verified by restriction enzyme digestion and DNA sequencing (Applied Biosystems, 4337455BigDye). The HEK293-Phoenix packaging cell line (ATCC, CRL-3213) was transfected with the pMRXIP-reporter vectors using MetafectenePro (Biontex, T040-1.0). The virus-containing media from transfected HEK293-Phoenix cells was harvested 24, 48 and 72 h post transfection. The harvested media was subsequently filtered through a 0.45- μm filter and then added onto subconfluent H9c2 cells. Hexadimetretribromide-polybrene (Sigma-Aldrich, H9268) was added to a final concentration of 8 $\mu\text{g}/\text{ml}$. The H9c2 cells were incubated with the virus-containing media with polybrene for 6–12 h each time. The transduced H9c2 cells were then selected with 1 $\mu\text{g}/\text{ml}$ of puromycin. Stable expression of mCherry-EGFP-SYNJ2BP-TM or TOMM20-mCherry-EGFP was verified by western blotting and confocal imaging. Furthermore, the cells were sorted by fluorescence activated cell sorting (FACS) to ensure approximately equal expression level of the mitochondrial outer membrane reporter.

High-resolution respirometry

At the day of measurements, the mCherry-EGFP-SYNJ2BP-TM H9c2 cells, grown in glucose or adapted to galactose for 7 to 21 days, were trypsinized, and resuspended in their conditioned medium and counted using Countess II (ThermoFisher Scientific). Respirometry was performed in an Oxygraph-2k system (Oroboros Instruments, Innsbruck, Austria) calibrated to air (gain for oxygen sensor was set to 2) with standard cell culture medium at 37°C. The measurements were repeated in 4 independent experiments. Based on the cell number, a calculated volume of cells was added to the two stirred (750 rpm) chambers aiming to a final concentration of 0.4×10^6 cells/ml. The cell counting was repeated to determine the exact cell concentration in each chamber, and chambers were sealed to obtain a closed system. Analysis of the oxygen concentration in the chambers was performed using DatLab version 5.1.0.20 (Oroboros Instruments, Innsbruck, Austria). Decreasing oxygen concentration in the chambers resembled cellular oxygen consumption. When the oxygen consumption rate, OCR (O_2 flux ($\text{pmolO}_2/\text{s} \cdot \text{ml}$)) reached a steady state level, a measurement was recorded displaying total cellular respiration (basal). Leak respiration was assessed by the addition of oligomycin (Sigma-Aldrich, O4876) in a final concentration of 5 μM . Subsequently, the proton gradient

was released by stepwise titration (0.5 $\mu\text{M}/\text{step}$) of the uncoupler carbonylcyanide-3-chlorophenylhydrazone (CCCP) (Sigma-Aldrich, C2759) until the maximum respiration was achieved (electron transport system capacity, ETS capacity). The addition of 0.5 μM rotenone (Sigma-Aldrich, R8875) an inhibitor of CI and 2.5 μM antimycin A (Sigma-Aldrich, A8674) an inhibitor of CIII blocked mitochondrial respiration completely, resulting in residual oxygen consumption (ROX). The respiration measurement at the different STATES (basal, leak, ETS) were corrected for ROX afterward. Mitochondrial respiration was calculated by subtracting the non-mitochondrial respiration after antimycin A addition from the basal respiration level. ATP linked respiration was derived from subtracting the leak respiration (oligomycin) from the basal level. All respiration data was normalized to the cell count in the chamber. The results were presented as a mean.

Mitochondrial ROS measurements with MitoSox Red

H9c2 cells grown under normal culture conditions or adapted to galactose were treated with 100 nM antimycin A for 4 h or left untreated. After treatment, cells were harvested by trypsinization, washed three times with respective media and then incubated with 1 μM MitoSOX Red (ThermoFisher Scientific, M36008) for 30 min inside the cell incubator in their respective media. The cells were then washed 3 times with HBSS (Gibco, 1402-092) followed by flow cytometry analysis with a LSRFortessa (BD Biosciences). The excitation light used was 488 nm, emission was passed through 556LP filter and detected using a 616/23 nm emission filter. For confocal imaging purposes the cells were seeded in MatTek dishes (MatTek, P35-1.5-14-C) treated with antimycin A and stained with MitoSOX Red as described above, followed by HBSS washing prior to live cell confocal imaging. MitoSOX Red fluorescence was excited using the 514 nm laser and the emitted light was detected between 565–715 nm.

Mitochondrial membrane potential visualization

The mCherry-EGFP-SYNJ2B-TM H9c2 cells grown under normal conditions or adapted to galactose were incubated with MitoTracker Deep Red (ThermoFisher Scientific, M22426) at 100 nM concentration for 30 min. The cells were then given fresh cell culture media and subjected to live Airyscan FAST imaging using the Zeiss LSM 880.

Antibodies

The following primary antibodies were used: anti-GAPDH (Sigma-Aldrich, G9545; 1:5000) anti-TOMM20 (Santa Cruz Biotechnology, SC-11415; 1:500), anti-FIS1 (Proteintech, 10956-1-1ap; 1:100), anti-ATP5F1A/ATP5A (Abcam, Ab14748; 1:200), anti-PDHA1 (Abcam, ab110330; 1:200), anti-ATG7 (Cell Signaling Technology, 8558; 1:1000), anti-RAB9A (Cell Signaling Technology, 5118; 1:1000), anti-ULK1 (Cell Signaling Technology, 8054; 1:1000), anti-RAB5A (Cell Signaling Technology, C8B1; 1:1000), anti-RAB7 (ERP7589; Abcam,

ab137029; 1:1000), anti-LC3B (Sigma-Aldrich, L7543;1:200). Alexa Fluor 647-conjugated goat anti-rabbit and anti-mouse IgG (Invitrogen, A21244 and A32728; 1:500) were used as secondary antibodies.

Immunostaining of fixed cells

For immunofluorescent staining the cells were seeded on #1.5 glass coverslips. At

approximately 80% confluence the cells were subjected to treatment. The cells were then fixed using 4% formaldehyde (ThermoFisher Scientific, J19943.K2) at 37°C for 20 min. The cells were permeabilized with methanol at room temperature for 5 min. The permeabilized cells were blocked with 3% pre-immune goat serum (Sigma-Aldrich, G6767) in phosphate-buffered saline (PBS; Sigma-Aldrich, D8537) for 1 h at room temperature before overnight incubation at 4°C with primary antibodies diluted in PBS with 1% goat serum. Cells were then washed and incubated for 1 h with Alexa Fluor-coupled secondary antibodies diluted 1:500 in PBS supplemented with 1% goat serum. After a final wash in PBS the coverslips were mounted on glass slides using Prolong Glass (Invitrogen, P36980).

RNAi

The short interfering RNAs (siRNAs) used were pre-designed and validated *Silencer*[®]Select siRNAs (Invitrogen, 4390771): siRNA against *Ulk1* (siRNA ID s166350), siRNA against *Atg7* (siRNA ID s161900), siRNA against *Rab9a* (siRNA ID s136762), siRNA against *Rab5a* (siRNA ID s134381), siRNA against *Rab7a* (siRNA ID s131440) and negative control siRNA (Ambion, 4390844). The cells were transfected with siRNA using Lipofectamine RNAiMax Transfection Reagent (Invitrogen, 13778-075) according to the manufacturer's recommendation. After 6 h of incubation the cell media was changed to remove the transfection reagent in order to avoid H9c2 cell death. After 48 or 72 h (two consecutive siRNA transfections) of siRNA knockdown the cells were fixed or harvested for western blot analysis. The cells were fixed with 4% formaldehyde with 0.2% glutaraldehyde (Sigma-Aldrich, G5882). For each coverslip of fixed cells/condition, 10 positions (containing more than 100 cells in total) were selected and imaged as a Z-stack on a Cell Discoverer7 widefield microscope (Carl Zeiss Microscopy). Quantification of red-only dots was performed using the IMARIS imaging analysis software (see below).

NaveniFlex Proximity Ligation Assay (PLA)

The PLA assay was performed according to Navinci's recommendations using NaveniFlex MR In Situ Detection kit (Navinci, NF.100.2) and all incubations were performed in a humidity chamber. Briefly, cells were seeded on coverslips and grown until around 80% confluency. The cells were fixed using 4% PFA at 37°C for 20 min and permeabilized with 100% methanol at room temperature for 5 min. The coverslips were then washed two times in PBS, blocked with Blocking solution (Navinci, NF.1.100.01) for 30 min at 37°C and then incubated with two primary antibodies (derived from mouse

and rabbit, respectively) diluted in primary antibody diluent (Navinci, NF.1.100.02) overnight at 4°C. As a negative control one coverslip was incubated in Antibody diluent with only one primary antibody. The coverslips were washed and then incubated with the PLA probes corresponding to the primary antibodies using Navenibody M1 (Navinci, NF.1.100.004,) and Navenibody R2 (Navinci, NF.1.100.05) in Navenibody Diluent (Navinci, NF.1.100.03) for 1 h at 37°C. Then, the coverslips were washed and subsequently incubated for DNA ligation with enzyme A (Navinci, NF.2.100.09) in buffer A (Navinci, NF.2.100.08) and enzyme B (Navinci, NF.2.100.11) in buffer B (Navinci, NF.2.100.10) for 1 hour and 30 min, respectively at 37°C. The coverslips were washed and finally incubated with enzyme C (Navinci, NF.2.100.15), a DNA polymerase, diluted in amplification buffer C Atto 647N (Navinci, NF.2.100.14) for 90 min at 37°C protected from light. Finally, the coverslips were stained with DAPI, washed, and then mounted on glass slides using Prolong Glass antifade mountant media. The fluorescent PLA signal and DAPI was detected using LSM800 confocal microscope (Carl Zeiss Microscopy) equipped with a 40X NA1.2 water immersion objective. Images were acquired as 3-slice Z-stacks. A minimum of 10 positions per coverslip of fixed cells (containing over 50 cells in total) were imaged per condition in two independent experiments. Quantification of PLA puncta was performed on the images using the IMARIS image analysis software.

Western blot analysis of total H9c2 cell lysates

Cells were lysed by scraping in 2X sodium dodecyl sulfate (SDS) buffer (100 mM Tris-HCl, pH 6.8, 20% glycerol, 4% SDS) with 1× Complete Mini EDTA-Free Protease Inhibitor Cocktail (Roche, 11697498001) and boiling for 5 min. Total protein content of cell extracts was determined using a Bicinchoninic Acid (BCA) Kit (ThermoFisher Scientific, 23227). Total protein lysates (15 µg) were run on Mini-Protean TGX 4–20% gradient gels (Bio-Rad, 456–1093) and transferred onto Invitrolon[™] PVDF membranes (Invitrogen, LC2005). Transfer was visualized with Ponceau staining and the membrane was blocked with 5% nonfat dry milk in TBST (20 mM Tris pH 7.5, 150 mM NaCl, 0.1% Tween 20 [P1379, Sigma-Aldrich]). The membrane was incubated with primary antibody overnight at 4°C followed by 1 h incubation at room temperature with horseradish peroxidase (HRP)-conjugated secondary antibody; BD Pharmingen HRP Goat Anti-Mouse Ig (BD Biosciences, 554002) or HRP-conjugated Affinipure Goat Anti-Rabbit IgG (H+L) (Proteintech, SA00001–2). Signal detection was performed with a western blotting chemiluminescent reagent (Sigma-Aldrich, CPS3500) and an iBright Imaging System (ThermoFisher Scientific).

Widefield and confocal imaging of fixed cells

For imaging, Celldiscoverer7, LSM800 and LSM880 (all systems Carl Zeiss Microscopy) were used. For all images taken with the Celldiscoverer7 a Plan-Apochromat 50× objective with an NA of 1.2 was used. The images were acquired as

z-stacks. The LSM800 was used with a Plan-Apochromat 63× oil (M27) objective with an NA of 1.4 for verification of colocalization of red-only dots and mitochondrial proteins. The Plan-Apochromat 40× water objective with an NA of 1.2 was used for imaging PLA puncta, which were acquired as z-stacks. For the LSM880 the images were acquired either with a Plan-Apochromat 63× oil objective with an NA of 1.4 or a C-Apochromat 40× water objective with an NA of 1.2. The LSM880 was used for bright field and fluorescence imaging in CLEM experiments to image cells of interest and to map the relevant grid coordinate for correlation with TEM images.

Three-dimensional (3D) structured illumination microscopy (SIM) imaging of fixed and live cells cells.

The mCherry-EGFP-SYNJAB-TM H9c2 cells were seeded on MatTek dishes (MatTek Corporation, P35G-1.5-14-C) and imaged when they reached approximately 80% confluency. For labeling of lysosomes, the cells were treated with 100 nM LysoTracker Deep Red (ThermoFisher Scientific, L12492) for 40 min. After labeling, the cells were fixed with 4% formaldehyde and 0.2% glutaraldehyde or the media was replaced with fresh cell-culture media right before live imaging. The fixed cells were washed in PBS and imaged in PBS. For live cell imaging the cells were imaged in their growth medium at 37°C with atmospheric gas levels. The images were acquired using a DeltaVision OMX V4 Blaze imaging system (GE Healthcare) equipped with a 60X 1.42NA oil-immersion objective (Olympus), three sCMOS cameras, and 405, 488, 568, and 642 nm lasers for excitation. The vendor-specified optical resolution of the 3DSIM system is 110–160 nm laterally, and 340–380 nm axially, depending on the color channel. Super-resolution 3D images were obtained by 3DSIM reconstructions using the manufacturer-supplied softWoRx program (GE Healthcare). The SIM figure panels and AVI movies (maximum intensity z-projected and bleach corrected image sequenced using the exponential fit option) were assembled using Fiji [71].

AiryScan FAST imaging of live cells after lysosome labeling with LysoView 650

Live mCherry-EGFP-SYNJ2B-TM H9c2 cells grown in MatTek dishes were stained with LysoView 650 (Biotium, 70059) for 30 min and imaged using the AiryScan FAST mode of the LSM880, utilizing line-wise switching between tracks to avoid time delay between channels. Cells were maintained in a humidified stage-top incubator at 37°C and 5% CO₂ during imaging. Timelapse series (500 frames in total) were recorded using a 40× NA1.2 water immersion objective lens and a zoom factor of 4.0, with optimized scan settings for subsequent AiryScan processing (50 nm pixel size). The pixel dwell time was 0.73 μs, resulting in an individual frame time of 1.01 s. Laser excitation at 488 nm, 561 nm and 633 nm was used for EGFP, mCherry, and LysoView 650, respectively. The resulting

raw files were processed using automatic settings (strength 6.0) in ZEN ver. 2.3 (Carl Zeiss Microscopy).

Correlative-light and electron microscopy (CLEM)

Cells were grown on gridded #1.5 glass coverslips in 35-mm dishes (P35G-1.5-14-CGRD, MatTek). The cells were incubated with 50 nM LysoTracker Deep Red for 30 min before fixation with 4% formaldehyde and 0.5% glutaraldehyde in PHEM buffer, pH 6.9 (60 mM PIPES, 25 mM HEPES, 10 mM EGTA, 2 mM MgCl₂). The cells were stained with DAPI and washed twice with PBS. After confocal imaging, the cells were processed for TEM using 0.05% malachite green (Sigma-Aldrich, 101398), 1% osmium tetroxide (Electron Microscopy Sciences, 19110)/0.8% K₃Fe(CN)₆ (Sigma-Aldrich, 702587), 1% tannic acid (Electron Microscopy Sciences, 21700), and 1% uranyl acetate (Electron Microscopy Sciences, 22400), followed by stepwise ethanol dehydration and embedding in epoxy resin (Agar, R1043). All processing steps were carried out using a microwave processor (Pelco BioWave, Ted Pella, Inc.). Finally, the resin was polymerized at 60° C for 48 h. After polymerization, the relevant dish coordinates were relocated and trimmed using a glass knife on an UC6 ultramicrotome (Leica Microsystems). Ultrathin sections (70 nm) were cut using a 35° ultra-knife (Diatome) and collected on slot grids. Sections were imaged using a HT7800 transmission electron microscope (Hitachi High-Tech) at 100 kV using a Xarosa CMOS camera and Radius ver. 2.0 (EMSYS). Preliminary image correlation of confocal images and TEM images was performed at the microscope using MirrorCLEM ver. 2.0.3 (Astron, Inc.). Final correlation was performed using the ec-CLEM plugin [72] in Icy ver. 2.4.2.0 [73] using DAPI, LysoTracker Deep Red, and tubular EGFP/mCherry-positive mitochondria as registration landmarks.

Image analysis.

Fluorescence images were analyzed using Imaris ver. 9.6.1 (Bitplane). Images were converted from the .zen file format used by ZEISS microscopes into the .ims file format used by Imaris by the Imaris file converter. No preprocessing was performed. For the quantification of red-only mitochondria the Imaris XTension Channel Arithmetics was used in conjunction with an adapted Batch Processing XTension to create a new third image channel containing only areas where the mCherry signal was 50% higher than the EGFP signal. The Spots function was then

utilized to mark the mCherry signal and the DAPI-stained nuclei of all cells in the image, excluding those within 1 μm of the edge of the image. Each image was then manually inspected to remove artifacts. The Spots function was also utilized for the quantification of PLA puncta.

Machine learning classification of mitochondria morphology

Classification of mitochondria was performed on the segmentation results obtained from the deep learning-based

segmentation model that is trained on a simulated dataset [43]. The training dataset consists of thousands of images that are simulated by one, mimicking the geometrical shapes of mitochondria, and two, computationally modeling the process of image formation in a microscope. The simulated dataset is curated to closely match the microscope parameters of the data to be analyzed. The steps of segmentation began with the input confocal fluorescence images (EGFP-channel) that were cropped to sizes suitable for the deep learning-based segmentation model. The results from the segmentation model were then stitched back together to the original sizes of the images. The morphological classification of the individual mitochondria was done based on their branch lengths. For this, the segmentation results were first skeletonized using the Skan library [74] and the branch lengths of individual mitochondria were calculated for each experimental group. To prevent noisy segmentations from being included in the analysis, entries with branch lengths less than the resolution limit of the microscope were excluded. The rules for classifying mitochondria into the morphological classes of dots, rods, and networks were as follows; any mitochondria less than 1 μm in length was classified as a dot, those having lengths greater than 1 μm were further subdivided into rods, if they did not have junctions in their skeleton, and networks if they had at least one junction. The morphology classification was normalized per image frame for 19 or 22 images from each condition, glucose or galactose adapted cells respectively.

Statistical analysis

The quantification data acquired using the IMARIS software underwent statistical analysis.

For the percentage of cells that contained red-only dots we approximated the proportions with normal distributions and thereafter we performed a two-tailed Z-test. For the average number of red-only dots per cell we assumed that these averages followed normal distributions so that a two-tailed Z-test could be utilized for the large sample sizes. The same was assumed for analysis of average number of PLA puncta per cell and for the morphological analysis. For the morphological analysis the statistical analysis was performed on a per frame basis. For the mitochondrial respiration data two-tailed paired t-tests were performed. Multiple comparison correction was performed with Bonferroni correction. Datasets subjected to quantitative and statistical analysis were from a minimum of three independent experiments, each independent experiment contained minimum 100 cells per condition analyzed. The exception was the dataset for PLA puncta quantification that was derived from two independent experiments and the morphological classification which had a dataset made from a single independent experiment. The PLA dataset contained minimum 50 cells per condition analyzed for each independent experiment, while the morphological classification was based on a single qualitative dataset of approximately 20 frames with representative cells from each condition. The data in graphs is represented as the mean \pm SEM, individual datapoints are

per frame averages. Statistical significance in the form of p-value is shown as * $p < 0.05$, ** $p < 0.01$, *** $p < 0.001$ and **** $p < 0.0001$.

Acknowledgements

We thank professor Terje Johansen (University of Tromsø–The Arctic University of Norway) for access to reagents for constructing stable cell lines. We acknowledge professor Balpreet S. Ahluwalia and Dr. Deanna Wolfson (University of Tromsø–The Arctic University of Norway) for facilitating SIM imaging. We thank the Advanced Microscopy Core-Facility (University of Tromsø–The Arctic University of Norway) for use of instruments and assistance.

Disclosure statement

No potential conflict of interest was reported by the author(s).

Funding

The work was supported by the Helse Nord RHF [HNF1449-19]; Horizon 2020 Framework Programme [grant agreement No 964800]; Universitetet i Tromsø [VirtualStain; project number 2061348].

ORCID

Asa Birna Birgisdottir  <http://orcid.org/0000-0003-1080-3619>

Data availability statement

The 3D SIM data that support the findings of this study are openly available in Opstad, IS. et al, 2021, "3DSIM data of mitochondria in the cardiomyoblast cell-line H9c2 adapted to either glucose or galactose", at https://doi.org/10.18710/PDCLAS_DataverseNO_V2

References

- [1] Zorov DB, Juhaszova M, Sollott SJ. Mitochondrial reactive oxygen species (ROS) and ROS-induced ROS release. *Physiol Rev.* 2014 Jul;94(3):909–950. Pubmed PMID: 24987008. doi: [10.1152/physrev.00026.2013](https://doi.org/10.1152/physrev.00026.2013)
- [2] Pathak T, Trebak M. Mitochondrial Ca^{2+} signaling. *Pharmacol Ther.* 2018 Dec;192:112–123. Pubmed PMID: 30036491. doi: [10.1016/j.pharmthera.2018.07.001](https://doi.org/10.1016/j.pharmthera.2018.07.001)
- [3] Dietz JV, Fox JL, Khalimonchuk O. Down the Iron path: mitochondrial Iron Homeostasis and Beyond. *Cells.* 2021 Aug 25;10(9):2198. Pubmed PMID: 34571846. doi: [10.3390/cells10092198](https://doi.org/10.3390/cells10092198)
- [4] Sandhir R, Halder A, Sunkaria A. Mitochondria as a centrally positioned hub in the innate immune response. *Biochim Biophys Acta Mol Basis Dis.* 2017 May;1863(5):1090–1097. Pubmed PMID: 27794419. doi: [10.1016/j.bbadis.2016.10.020](https://doi.org/10.1016/j.bbadis.2016.10.020)
- [5] Bock FJ, Tait SWG. Mitochondria as multifaceted regulators of cell death. *Nat Rev Mol Cell Biol.* 2020 Feb;21(2):85–100. Pubmed PMID: 31636403. doi: [10.1038/s41580-019-0173-8](https://doi.org/10.1038/s41580-019-0173-8)
- [6] Youle RJ, van der Bliek AM. Mitochondrial fission, fusion, and stress. *Science.* 2012 Aug 31;337(6098):1062–1065. Pubmed PMID: 22936770. doi: [10.1126/science.1219855](https://doi.org/10.1126/science.1219855)
- [7] Kruppa AJ, Buss F. Motor proteins at the mitochondria-cytoskeleton interface. *J Cell Sci.* 2021 Apr 1;134(7):jcs226084. Pubmed PMID: 33912943. doi: [10.1242/jcs.226084](https://doi.org/10.1242/jcs.226084)
- [8] Yapa NMB, Lisnyak V, Reljic B, et al. Mitochondrial dynamics in health and disease. *FEBS Lett.* 2021 Apr;595(8):1184–1204. Pubmed PMID: 33742459. doi: [10.1002/1873-3468.14077](https://doi.org/10.1002/1873-3468.14077)
- [9] Montava-Garriga L, Ganley IG. Outstanding questions in mitophagy: what we do and do not know. *J Mol Biol.* 2020 Jan 3;432

- (1):206–230. Pubmed PMID: 31299243. doi: [10.1016/j.jmb.2019.06.032](https://doi.org/10.1016/j.jmb.2019.06.032)
- [10] Ng MYW, Wai T, Simonsen A. Quality control of the mitochondrion. *Developmental Cell*. 2021 Apr 5;56(7):881–905. Pubmed PMID: 33662258. doi: [10.1016/j.devcel.2021.02.009](https://doi.org/10.1016/j.devcel.2021.02.009)
- [11] Lemasters JJ. Selective mitochondrial autophagy, or mitophagy, as a targeted defense against oxidative stress, mitochondrial dysfunction, and aging. *Rejuvenation Res*. 2005;8(1):3–5. SpringSpring. doi: [10.1089/rej.2005.8.3](https://doi.org/10.1089/rej.2005.8.3)
- [12] Kim I, Rodriguez-Enriquez S, Lemasters JJ. Selective degradation of mitochondria by mitophagy. *Arch Biochem Biophys*. 2007 Jun 15;462(2):245–253. Pubmed PMID: 17475204. doi: [10.1016/j.abb.2007.03.034](https://doi.org/10.1016/j.abb.2007.03.034)
- [13] Youle RJ, Narendra DP. Mechanisms of mitophagy. *Nat Rev Mol Cell Biol*. 2011 Jan;12(1):9–14. Pubmed PMID: 21179058. doi: [10.1038/nrm3028](https://doi.org/10.1038/nrm3028)
- [14] Palikaras K, Lionaki E, Tavernarakis N. Mechanisms of mitophagy in cellular homeostasis, physiology and pathology. *Nat Cell Biol*. 2018 Sep;20(9):1013–1022. Pubmed PMID: 30154567. doi: [10.1038/s41556-018-0176-2](https://doi.org/10.1038/s41556-018-0176-2)
- [15] Zachari M, Ganley IG, Lane JD, et al. The mammalian ULK1 complex and autophagy initiation. *Essays Biochem*. 2017 Dec 12;61(6):585–596. Pubmed PMID: 29233870. doi: [10.1042/EBC20170021](https://doi.org/10.1042/EBC20170021)
- [16] Egan DF, Shackelford DB, Mihaylova MM, et al. Phosphorylation of ULK1 (hATG1) by AMP-activated protein kinase connects energy sensing to mitophagy. *Science*. 2011 Jan 28;331(6016):456–461. Pubmed PMID: 21205641. doi: [10.1126/science.1196371](https://doi.org/10.1126/science.1196371)
- [17] Wu W, Tian W, Hu Z, et al. ULK1 translocates to mitochondria and phosphorylates FUNDC1 to regulate mitophagy. *EMBO Rep*. 2014 May;15(5):566–575. Pubmed PMID: 24671035. doi: [10.1002/embr.201438501](https://doi.org/10.1002/embr.201438501)
- [18] Laker RC, Drake JC, Wilson RJ, et al. Ampk phosphorylation of Ulk1 is required for targeting of mitochondria to lysosomes in exercise-induced mitophagy. *Nat Commun*. 2017 Sep 15;8(1):548. Pubmed PMID: 28916822. doi: [10.1038/s41467-017-00520-9](https://doi.org/10.1038/s41467-017-00520-9)
- [19] Murakawa T, Okamoto K, Omiya S, et al. A mammalian mitophagy receptor, Bcl2-L-13, recruits the ULK1 complex to induce mitophagy. *Cell Rep*. 2019 Jan 8;26(2):338–345. Pubmed PMID: 30625316. doi: [10.1016/j.celrep.2018.12.050](https://doi.org/10.1016/j.celrep.2018.12.050)
- [20] Martens S, Fracchiolla D. Activation and targeting of ATG8 protein lipidation. *Cell Discov*. 2020 May 5;6(1):23. Pubmed PMID: 32377373. doi: [10.1038/s41421-020-0155-1](https://doi.org/10.1038/s41421-020-0155-1)
- [21] Tanida I, Mizushima N, Kiyooka M, et al. Apg7p/Cvt2p: a novel protein-activating enzyme essential for autophagy. *Mol Biol Cell*. 1999 May;10(5):1367–1379. Pubmed PMID: 10233150. doi: [10.1091/mbc.10.5.1367](https://doi.org/10.1091/mbc.10.5.1367)
- [22] Tanida I, Tanida-Miyake E, Ueno T, et al. The human homolog of *Saccharomyces cerevisiae* Apg7p is a Protein-activating enzyme for multiple substrates including human Apg12p, GATE-16, GABARAP, and MAP-LC3. *J Biol Chem*. 2001 Jan 19;276(3):1701–1706. Pubmed PMID: 11096062. doi: [10.1074/jbc.C000752200](https://doi.org/10.1074/jbc.C000752200)
- [23] Komatsu M, Tanida I, Ueno T, et al. The C-terminal region of an Apg7p/Cvt2p is required for homodimerization and is essential for its E1 activity and E1-E2 complex formation. *J Biol Chem*. 2001 Mar 30;276(13):9846–9854. Pubmed PMID: 11139573. doi: [10.1074/jbc.M007737200](https://doi.org/10.1074/jbc.M007737200)
- [24] Honda S, Arakawa S, Nishida Y, et al. Ulk1-mediated Atg5-independent macroautophagy mediates elimination of mitochondria from embryonic reticulocytes. *Nat Commun*. 2014 Jun 4;5(1):4004. Pubmed PMID: 24895007. doi: [10.1038/ncomms5004](https://doi.org/10.1038/ncomms5004)
- [25] Hirota Y, Yamashita S, Kurihara Y, et al. Mitophagy is primarily due to alternative autophagy and requires the MAPK1 and MAPK14 signaling pathways. *Autophagy*. 2015;11(2):332–343. Pubmed PMID: 25831013. doi: [10.1080/15548627.2015.1023047](https://doi.org/10.1080/15548627.2015.1023047)
- [26] Wang L, Klionsky DJ, Shen HM. The emerging mechanisms and functions of microautophagy. *Nat Rev Mol Cell Biol*. 2022 Sep 12;24(3):186–203. Pubmed PMID: 36097284. doi: [10.1038/s41580-022-00529-z](https://doi.org/10.1038/s41580-022-00529-z)
- [27] Hammerling BC, Najor RH, Cortez MQ, et al. A Rab5 endosomal pathway mediates Parkin-dependent mitochondrial clearance. *Nat Commun*. 2017 Jan 30;8(1):14050. Pubmed PMID: 28134239. doi: [10.1038/ncomms14050](https://doi.org/10.1038/ncomms14050)
- [28] Saito T, Nah J, Oka SI, et al. An alternative mitophagy pathway mediated by Rab9 protects the heart against ischemia. *J Clin Invest*. 2019 Feb 1;129(2):802–819. Pubmed PMID: 30511961. doi: [10.1172/JCI122035](https://doi.org/10.1172/JCI122035)
- [29] Wong YC, Ysselstein D, Krainc D. Mitochondria-lysosome contacts regulate mitochondrial fission via RAB7 GTP hydrolysis. *Nature*. 2018;554(7692):382–386. Feb 15 Pubmed PMID: 29364868 doi: [10.1038/nature25486](https://doi.org/10.1038/nature25486)
- [30] McWilliams TG, Muqit MM. PINK1 and Parkin: emerging themes in mitochondrial homeostasis. *Curr Opin Cell Biol*. 2017 Apr;45:83–91. Pubmed PMID: 28437683. doi: [10.1016/j.ceb.2017.03.013](https://doi.org/10.1016/j.ceb.2017.03.013)
- [31] Narendra D, Tanaka A, Suen DF, et al. Parkin is recruited selectively to impaired mitochondria and promotes their autophagy. *J Cell Bio*. 2008 Dec 1;183(5):795–803. Pubmed PMID: 19029340. doi: [10.1083/jcb.200809125](https://doi.org/10.1083/jcb.200809125)
- [32] Narendra DP, Jin SM, Tanaka A, et al. PINK1 is selectively stabilized on impaired mitochondria to activate Parkin. *PLoS Biol*. 2010 Jan 26;8(1):e1000298. Pubmed PMID: 20126261. doi: [10.1371/journal.pbio.1000298](https://doi.org/10.1371/journal.pbio.1000298)
- [33] Wang Y, Serricchio M, Jauregui M, et al. Deubiquitinating enzymes regulate PARK2-mediated mitophagy. *Autophagy*. 2015 Apr 3;11(4):595–606. Pubmed PMID: 25915564. doi: [10.1080/15548627.2015.1034408](https://doi.org/10.1080/15548627.2015.1034408)
- [34] Bhujabal Z, Birgisdottir ÅB, Sjøttem E, et al. FKBP8 recruits LC3A to mediate Parkin-independent mitophagy. *EMBO Rep*. 2017 Jun;18(6):947–961. Pubmed PMID: 28381481. doi: [10.15252/embr.201643147](https://doi.org/10.15252/embr.201643147)
- [35] Opstad IS, Godtliebsen G, Ahluwalia BS, et al. Mitochondrial dynamics and quantification of mitochondria-derived vesicles in cardiomyoblasts using structured illumination microscopy. *J Biophoto*. 2022 Feb;15(2):e202100305. Pubmed PMID: 34766731. doi: [10.1002/jbio.202100305](https://doi.org/10.1002/jbio.202100305)
- [36] Shaner NC, Steinbach PA, Tsien RY. A guide to choosing fluorescent proteins. *Nat Methods*. 2005 Dec;2(12):905–909. Pubmed PMID: 16299475. doi: [10.1038/nmeth819](https://doi.org/10.1038/nmeth819)
- [37] Dott W, Mistry P, Wright J, et al. Modulation of mitochondrial bioenergetics in a skeletal muscle cell line model of mitochondrial toxicity. *Redox Biol*. 2014. Jan 10;2:224–233. Pubmed PMID: 24494197. doi: [10.1016/j.redox.2013.12.028](https://doi.org/10.1016/j.redox.2013.12.028)
- [38] Wu H, Chen Q. Hypoxia activation of mitophagy and its role in disease pathogenesis. *Antioxid Redox Signal*. 2015 Apr 20;22(12):1032–1046. Pubmed PMID: 25526784. doi: [10.1089/ars.2014.6204](https://doi.org/10.1089/ars.2014.6204)
- [39] Katayama H, Kogure T, Mizushima N, et al. A sensitive and quantitative technique for detecting autophagic events based on lysosomal delivery. *Chem Biol*. 2011 Aug 26;18(8):1042–1052. Pubmed PMID: 21867919. doi: [10.1016/j.chembiol.2011.05.013](https://doi.org/10.1016/j.chembiol.2011.05.013)
- [40] Sun N, Malide D, Liu J, et al. A fluorescence-based imaging method to measure in vitro and in vivo mitophagy using mt-Keima. *Nat Protoc*. 2017 Aug;12(8):1576–1587. Pubmed PMID: 28703790. doi: [10.1038/nprot.2017.060](https://doi.org/10.1038/nprot.2017.060)
- [41] Twig G, Elorza A, Molina AJ, et al. Fission and selective fusion govern mitochondrial segregation and elimination by autophagy. *Embo J*. 2008 Jan 23;27(2):433–446. Pubmed PMID: 18200046. doi: [10.1038/sj.emboj.7601963](https://doi.org/10.1038/sj.emboj.7601963)
- [42] Kleele T, Rey T, Winter J, et al. Distinct fission signatures predict mitochondrial degradation or biogenesis. *Nature*. 2021 May;593(7859):435–439. Pubmed PMID: 33953403. doi: [10.1038/s41586-021-03510-6](https://doi.org/10.1038/s41586-021-03510-6)
- [43] Sekh AA, Opstad IS, Godtliebsen G, et al. Physics-based machine learning for subcellular segmentation in living cells. *Nat Mach Intell*. 2021;3(12):1071–1080. doi: [10.1038/s42256-021-00420-0](https://doi.org/10.1038/s42256-021-00420-0)

- [44] Punnakkal AR, Godtliebsen G, Somani A, et al. Analyzing mitochondrial morphology through simulation supervised learning. *J Vis Exp.* 2023 Mar 3;(193). Pubmed PMID: 36939264. doi: [10.3791/64880-v](https://doi.org/10.3791/64880-v)
- [45] Mukhopadhyay P, Rajesh M, Haskó G, et al. Simultaneous detection of apoptosis and mitochondrial superoxide production in live cells by flow cytometry and confocal microscopy. *Nat Protoc.* 2007;2(9):2295–2301. Pubmed PMID: 17853886. doi: [10.1038/nprot.2007.327](https://doi.org/10.1038/nprot.2007.327)
- [46] Marroquin LD, Hynes J, Dykens JA, et al. Circumventing the Crabtree effect: replacing media glucose with galactose increases susceptibility of HepG2 cells to mitochondrial toxicants. *Toxicol Sci.* 2007 Jun;97(2):539–547. Pubmed PMID: 17361016. doi: [10.1093/toxsci/kfm052](https://doi.org/10.1093/toxsci/kfm052)
- [47] Klionsky DJ, Abdel-Aziz AK, Abdelfatah S, et al. Guidelines for the use and interpretation of assays for monitoring autophagy (4th edition)¹. *Autophagy.* 2021 Jan;17(1):1–382. Pubmed PMID: 33634751. doi: [10.1080/15548627.2020.1797280](https://doi.org/10.1080/15548627.2020.1797280)
- [48] Collier JJ, Suomi F, Oláhová M, et al. Emerging roles of ATG7 in human health and disease. *EMBO Mol Med.* 2021 Dec 7;13(12):e14824. Pubmed PMID: 34725936. doi: [10.15252/emmm.202114824](https://doi.org/10.15252/emmm.202114824)
- [49] Zhao JF, Rodger CE, Allen GFG, et al. HIF1 α -dependent mitophagy facilitates cardiomyoblast differentiation. *Cell Stress.* 2020 Mar 4;4(5):99–113. Pubmed PMID: 32420530. doi: [10.15698/cst2020.05.220](https://doi.org/10.15698/cst2020.05.220)
- [50] Söderberg O, Gullberg M, Jarvius M, et al. Direct observation of individual endogenous protein complexes in situ by proximity ligation. *Nat Methods.* 2006 Dec;3(12):995–1000. Pubmed PMID: 17072308. doi: [10.1038/nmeth947](https://doi.org/10.1038/nmeth947)
- [51] Sun N, Yun J, Liu J, et al. Measuring in vivo mitophagy. *Molecular Cell.* 2015 Nov 19;60(4):685–696. Pubmed PMID: 26549682. doi: [10.1016/j.molcel.2015.10.009](https://doi.org/10.1016/j.molcel.2015.10.009)
- [52] McWilliams TG, Prescott AR, Allen GF, et al. Mito-QC illuminates mitophagy and mitochondrial architecture in vivo. *J Cell Bio.* 2016 Aug 1;214(3):333–345. Pubmed PMID: 27458135. doi: [10.1083/jcb.201603039](https://doi.org/10.1083/jcb.201603039)
- [53] McWilliams TG, Prescott AR, Montava-Garriga L, et al. Basal mitophagy occurs independently of PINK1 in mouse tissues of high metabolic demand. *Cell Metab.* 2018 Feb 6;27(2):439–449.e5. Pubmed PMID: 29337137. doi: [10.1016/j.cmet.2017.12.008](https://doi.org/10.1016/j.cmet.2017.12.008)
- [54] Lee JJ, Sanchez-Martinez A, Martinez Zarate A, et al. Basal mitophagy is widespread in *Drosophila* but minimally affected by loss of Pink1 or parkin. *J Cell Bio.* 2018 May 7;217(5):1613–1622. Pubmed PMID: 29500189. doi: [10.1083/jcb.201801044](https://doi.org/10.1083/jcb.201801044)
- [55] Cornelissen T, Vilain S, Vints K, et al. Deficiency of parkin and PINK1 impairs age-dependent mitophagy in *Drosophila*. *Elife.* 2018 May 29;7:e35878. Pubmed PMID: 29809156. doi: [10.7554/eLife.35878](https://doi.org/10.7554/eLife.35878)
- [56] Singh F, Prescott AR, Rosewell P, et al. Pharmacological rescue of impaired mitophagy in Parkinson's disease-related LRRK2 G2019S knock-in mice. *Elife.* 2021 Aug 3;10:e67604. Pubmed PMID: 34340748. doi: [10.7554/eLife.67604](https://doi.org/10.7554/eLife.67604)
- [57] Munson MJ, Mathai BJ, Ng MYW, et al. GAK and PRKCD are positive regulators of PRKN-independent mitophagy. *Nat Commun.* 2021 Oct 20;12(1):6101. Pubmed PMID: 34671015. doi: [10.1038/s41467-021-26331-7](https://doi.org/10.1038/s41467-021-26331-7)
- [58] Allen GF, Toth R, James J, et al. Loss of iron triggers PINK1/Parkin-independent mitophagy. *EMBO Rep.* 2013 Dec;14(12):1127–1135. Pubmed PMID: 24176932. doi: [10.1038/embor.2013.168](https://doi.org/10.1038/embor.2013.168)
- [59] Rojansky R, Cha MY, Chan DC. Elimination of paternal mitochondria in mouse embryos occurs through autophagic degradation dependent on PARKIN and MUL1. *Elife.* 2016 Nov 17;5:e17896. Pubmed PMID: 27852436. doi: [10.7554/eLife.17896](https://doi.org/10.7554/eLife.17896)
- [60] Abudu YP, Shrestha BK, Zhang W, et al. SAMM50 acts with p62 in piecemeal basal- and OXPHOS-induced mitophagy of SAM and MICOS components. *J Cell Bio.* 2021 Aug 2;220(8):e202009092. Pubmed PMID: 34037656. doi: [10.1083/jcb.202009092](https://doi.org/10.1083/jcb.202009092)
- [61] Montava-Garriga L, Singh F, Ball G, et al. Semi-automated quantitation of mitophagy in cells and tissues. *Mech Ageing Dev.* 2020 Jan;185:111196. Pubmed PMID: 31843465. doi: [10.1016/j.mad.2019.111196](https://doi.org/10.1016/j.mad.2019.111196)
- [62] Melsner S, Chatelain EH, Lavie J, et al. Rheb regulates mitophagy induced by mitochondrial energetic status. *Cell Metab.* 2013 May 7;17(5):719–730. Pubmed PMID: 23602449. doi: [10.1016/j.cmet.2013.03.014](https://doi.org/10.1016/j.cmet.2013.03.014)
- [63] Guerroué F L, Eck F, Jung J, et al. Autophagosomal content profiling reveals an LC3C-Dependent piecemeal mitophagy pathway. *Mol Cell.* 2017 Nov 16;68(4):786–796.e6. Pubmed PMID: 29149599. doi: [10.1016/j.molcel.2017.10.029](https://doi.org/10.1016/j.molcel.2017.10.029)
- [64] Van Laar VS, Arnold B, Cassidy SJ, et al. Bioenergetics of neurons inhibit the translocation response of Parkin following rapid mitochondrial depolarization. *Hum Mol Genet.* 2011 Mar 1;20(5):927–940. Pubmed PMID: 21147754. doi: [10.1093/hmg/ddq531](https://doi.org/10.1093/hmg/ddq531)
- [65] MacVicar TD, Lane JD. Impaired OMA1-dependent cleavage of OPA1 and reduced DRP1 fission activity combine to prevent mitophagy in cells that are dependent on oxidative phosphorylation. *J Cell Sci.* 2014 May 15;127(Pt 10):2313–2325. Pubmed PMID: 24634514. doi: [10.1242/jcs.144337](https://doi.org/10.1242/jcs.144337)
- [66] Lee S, Zhang C, Liu X. Role of glucose metabolism and ATP in maintaining PINK1 levels during Parkin-mediated mitochondrial damage responses. *J Biol Chem.* 2015 Jan 9;290(2):904–917. Pubmed PMID: 25404737. doi: [10.1074/jbc.M114.606798](https://doi.org/10.1074/jbc.M114.606798)
- [67] Zhen Y, Spangenberg H, Munson MJ, et al. ESCRT-mediated phagophore sealing during mitophagy. *Autophagy.* 2020 May;16(5):826–841. Pubmed PMID: 31366282. doi: [10.1080/15548627.2019.1639301](https://doi.org/10.1080/15548627.2019.1639301)
- [68] Krantz S, Kim YM, Srivastava S, et al. Mitophagy mediates metabolic reprogramming of induced pluripotent stem cells undergoing endothelial differentiation. *J Biol Chem.* 2021 Dec;297(6):101410. Pubmed PMID: 34785214. doi: [10.1016/j.jbc.2021.101410](https://doi.org/10.1016/j.jbc.2021.101410)
- [69] Jung M, Choi H, Kim J, et al. Correlative light and transmission electron microscopy showed details of mitophagy by mitochondria quality control in propionic acid treated SH-SY5Y cell. *Materials.* 2020 Sep 29;13(19):4336. Pubmed PMID: 33003589. doi: [10.3390/ma13194336](https://doi.org/10.3390/ma13194336)
- [70] Li H, Doric Z, Berthet A, et al. Longitudinal tracking of neuronal mitochondria delineates PINK1/Parkin-dependent mechanisms of mitochondrial recycling and degradation. *Sci Adv.* 2021 Aug 6;7(32):eabf6580. Pubmed PMID: 34362731. doi: [10.1126/sciadv.abf6580](https://doi.org/10.1126/sciadv.abf6580)
- [71] Schindelin J, Arganda-Carreras I, Frise E, et al. Fiji: an open-source platform for biological-image analysis. *Nat Methods.* 2012 Jun 28;9(7):676–682. Pubmed PMID: 22743772. doi: [10.1038/nmeth.2019](https://doi.org/10.1038/nmeth.2019)
- [72] Paul-Gilloteaux P, Heiligenstein X, Belle M, et al. Ec-CLEM: flexible multidimensional registration software for correlative microscopies. *Nat Methods.* 2017 Jan 31;14(2):102–103. Pubmed PMID: 28139674. doi: [10.1038/nmeth.4170](https://doi.org/10.1038/nmeth.4170)
- [73] de Chaumont F, Dallongeville S, Chenouard N, et al. Icy: an open bioimage informatics platform for extended reproducible research. *Nat Methods.* 2012 Jun 28;9(7):690–696. Pubmed PMID: 22743774. doi: [10.1038/nmeth.2075](https://doi.org/10.1038/nmeth.2075)
- [74] Nunez-Iglesias J, Blanch AJ, Looker O, et al. A new Python library to analyse skeleton images confirms malaria parasite remodelling of the red blood cell membrane skeleton. *PeerJ.* 2018 Feb 15;6:e4312. Pubmed PMID: 29472997. doi: [10.7717/peerj.4312](https://doi.org/10.7717/peerj.4312)



Complex Data Analysis in Minutes

Simplify data overload and complexity using artificial intelligence (AI)-driven live-cell imaging and analysis - with no need for labels. Incucyte® AI Cell Health Analysis Software provides a powerful workflow that supports your entire research team. Reduce errors and achieve objective, repeatable results.











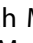











Simplifying Progress



Find Out More About Incucyte® AI Applications

SARTORIUS

Image analysis workflows to reveal the spatial organization of cell nuclei and chromosomes

Ricardo S Randall ^{ar*}, Claire Jourdain ^{br*}, Anna Nowicka ^{cr*}, Kateřina Kaduchová ^{cr*}, Michaela Kubová ^{dr*}, Mohammad A. Ayoub ^{er*}, Veit Schubert ^{er*}, Christophe Tatout ^{fr*}, Isabelle Colas ^{gr*}, Kalyanikrishna ^b, Sophie Desset ^f, Sarah Mermet ^f, Aurélia Boulaflous-Stevens ^f, Ivona Kubalová ^e, Terezie Mandáková ^d, Stefan Heckmann ^e, Martin A. Lysak ^h, Martina Panatta ⁱ, Raffaella Santoro ⁱ, Daniel Schubert ^b, Ales Pecinka ^c, Devin Routh^j, and Célia Baroux ^a

^aDepartment of Plant and Microbial Biology, Zürich-Basel Plant Science Center, University of Zürich, Zürich, Switzerland; ^bInstitute of Biology, Freie Universität Berlin, Germany; ^cCentre of the Region Haná for Biotechnological and Agricultural Research (CRH), Institute of Experimental Botany, v. v. i. (IEB), Olomouc, Czech Republic; ^dCentral European Institute of Technology (CEITEC) and Department of Experimental Biology, Masaryk University, Brno, Czech Republic; ^eLeibniz Institute of Plant Genetics and Crop Plant Research (IPK) Gatersleben, D-06466 Seeland, Germany; ^fInstitut Génétique, Reproduction et Développement (GrED), Université Clermont Auvergne, CNRS, INSERM, 63001 Clermont-Ferrand, France; ^gThe James Hutton Institute, Errol Road, Invergowrie, DD2 5DA, Scotland UK; ^hCentral European Institute of Technology (CEITEC) and National Centre for Biomolecular Research, Masaryk University, Brno, Czech Republic; ⁱDepartment of Molecular Mechanisms of Disease, DMMD, University of Zürich, Zürich, Switzerland; ^jService and Support for Science IT (S3IT), Universität Zürich, Zürich, Switzerland

ABSTRACT

Nucleus, chromatin, and chromosome organization studies heavily rely on fluorescence microscopy imaging to elucidate the distribution and abundance of structural and regulatory components. Three-dimensional (3D) image stacks are a source of quantitative data on signal intensity level and distribution and on the type and shape of distribution patterns in space. Their analysis can lead to novel insights that are otherwise missed in qualitative-only analyses. Quantitative image analysis requires specific software and workflows for image rendering, processing, segmentation, setting measurement points and reference frames and exporting target data before further numerical processing and plotting. These tasks often call for the development of customized computational scripts and require an expertise that is not broadly available to the community of experimental biologists. Yet, the increasing accessibility of high- and super-resolution imaging methods fuels the demand for user-friendly image analysis workflows. Here, we provide a compendium of strategies developed by participants of a training school from the COST action INDEPTH to analyze the spatial distribution of nuclear and chromosomal signals from 3D image stacks, acquired by diffraction-limited confocal microscopy and super-resolution microscopy methods (SIM and STED). While the examples make use of one specific commercial software package, the workflows can easily be adapted to concurrent commercial and open-source software. The aim is to encourage biologists lacking custom-script-based expertise to venture into quantitative image analysis and to better exploit the discovery potential of their images.

Abbreviations: 3D FISH: three-dimensional fluorescence in situ hybridization; 3D: three-dimensional; ASY1: ASYNAPTIC 1; CC: chromocenters; CO: Crossover; DAPI: 4',6-diamidino-2-phenylindole; DMC1: DNA MEIOTIC RECOMBINASE 1; DSB: Double-Strand Break; FISH: fluorescence in situ hybridization; GFP: GREEN FLUORESCENT PROTEIN; HEI10: HUMAN ENHANCER OF INVASION 10; NCO: Non-Crossover; NE: Nuclear Envelope; Oligo-FISH: oligonucleotide fluorescence in situ hybridization; RNPII: RNA Polymerase II; SC: Synaptonemal Complex; SIM: structured illumination microscopy; ZMM (ZIP: MSH4: MSH5 and MER3 proteins); ZYP1: ZIPPER-LIKE PROTEIN 1.

ARTICLE HISTORY

Received 28 June 2022
Revised 27 October 2022
Accepted 31 October 2022



KEYWORDS


Nucleus; chromatin; 3D organization; spatial distribution; image analysis; segmentation; quantification; mitosis; meiosis; chromosome; metaphase; pachytene; crossovers; nuclear speckles; nuclear bodies; RNA Pol II; transcription factories; oligo FISH; STED imaging; SIM

Introduction

Elucidating the spatial organization of eukaryotic genomes, their structural and compositional

dynamics during cellular processes and functional relationship with the nucleus, is a keystone of three-dimensional (3D) genomics. 3D genomics

CONTACT Célia Baroux  cbaroux@botinst.uzh.ch  Department of Plant and Microbial Biology, Zürich-Basel Plant Science Center, University of Zürich, Zürich, Switzerland
*equal contribution

 Supplemental data for this article can be accessed online at <https://doi.org/10.1080/19491034.2022.2144013>

© 2022 The Author(s). Published by Informa UK Limited, trading as Taylor & Francis Group.
This is an Open Access article distributed under the terms of the Creative Commons Attribution License (<http://creativecommons.org/licenses/by/4.0/>), which permits unrestricted use, distribution, and reproduction in any medium, provided the original work is properly cited.

aims to decipher the functional, 3D organizing principles of the chromosomes, chromatin domains and nucleus that contribute to transcription, replication, repair, and recombination. Understanding the 3D genome requires multidisciplinary methods including high-throughput, sequencing-based, molecular profiling techniques, computational simulation-based biophysical and mathematical modeling, and microscopy imaging at high-to-super resolution and in three-dimensions [1,2]. Microscopy followed by image analysis provides the opportunity to measure chromosome and chromatin structures down to the nanoscale, with a few kilobase resolution. This can inform on the genomic interactions *in situ* and the spatial organization of genomic domains in relation to the 3D nuclear space and its functional compartments [3,4].

Venturing into these opportunities to probe for the spatial organization of the genome *in situ* requires dedicated imaging and image analysis procedures, recently captured by the concept of quantitative, data-driven microscopy [1]. Quantitative image analysis for nuclear and chromosomal studies can be implemented at different levels of complexity, depending on the research question and, often, the expertise available. For instance, a simple level consists of scoring structures or patterns on the image based on user-defined classification. This can be applied when the immunolabelled chromatin protein, or FISH-labeled genomic domain, shows a very distinct distribution pattern (e.g. punctuate vs diffuse), varying between treatments or genotypes. In this case, quantifying the relative occurrence of pattern categories by scoring may be sufficient to address the original question. Manual scoring can also be used to quantify a moderate number of labeled regions (e.g., number of FISH signals or nuclear bodies). These categorical, quantitative approaches have the virtue to be accessible to all experimentalists, without sophisticated software. They allow to characterize relatively simple signal distribution patterns, providing, however, a limited number of samples, and double-blind scoring to avoid cognitive biases. Yet, for many images (e.g., from high-throughput imaging), images with multiple

labels, showing complex spatial patterns of signal distribution, with continuous (rather than discrete) variation in signal abundance, or a combination of all, require computationally driven processing approaches for quantitative analyses. A core step required is image segmentation. This process partitions the image based on the signal distribution into digital objects identifying biologically relevant structures. Various image segmentation methods and algorithms exist. These perform differently depending on the signal distribution [5], with deep-learning approaches for automated segmentation tasks at a large scale being continuously developed [6]. Once the image is segmented, multiple features can be extracted from the 3D digital objects, for instance, object number, size and shape; signal intensity and variance per object type, texture of the signal, channel and position in the image; distance relationships, and spatial distribution. Practically, these features are highly relevant to analyze the spatial organization of chromatin, chromosome and nuclear components *in situ*.

The field of chromatin, chromosome and nuclear organization studies would greatly benefit from the broader deployment of image processing-based quantitative analyses [2,3]. Several tools and packages have been developed in the past years based on open-source software, including for the 3D spatial analysis of nuclear organization [7–11]. Yet, a major hurdle for most ‘biology-only’ oriented labs is the lack of computational expertise for customizing the image processing scripts, for large data handling, the lack of template workflows, or a combination thereof. Key concepts, from image acquisition to quantitative data, have been framed in recent years, for applications in cell biology, but also to set good practice and standards in the field [1,12]. Efforts are undertaken to promote education and support in image analysis for scientists dealing with biological images [13]. This resource paper contributes to these efforts by providing a compendium of image analysis workflows for nucleus, chromatin and chromosome studies, taking seven case-studies as examples developed by participants of the training school of the INDEPTH COST action [14].

The workflows are based on a user-friendly, commercial image processing software (Imaris, Bitplane, Switzerland) but are conceptually applicable to concurrent (commercial or open source) software as discussed in this paper. In addition, although they largely borrow examples from plant nuclei and chromosomes, they remain transferable to the study of animal nuclei. Indeed, the organization of the nucleus, including the nuclear envelope, chromatin domains and chromosomes, share common organizing principles in plants and animals [15–18]

The workflows associated with each case study are briefly described below and are illustrated in the related figures. Each workflow is associated with a Supplemental File folder that includes a step-by-step guideline (text); a table summarizing the main step functions and parameters used on the training image; one or two training images per workflow; and, for workflow 1, a video tutorial. Training image datasets are available on the INDEPTH-OMERO repository [13,14].¹

Analyzing the spatial distribution of transcription clusters

In mammals, a radial gradient model of transcription in the nucleus has been proposed [19,20]. In plants, including the *Arabidopsis thaliana* (*Arabidopsis*) plant model, little is known about the spatial, 3D distribution of transcription. Transcriptional activity in the nucleus can be visualized *in situ* by immunolabeling the active isoform of RNA Polymerase II (RNPII). In *Arabidopsis*, super-resolution imaging of RNPII has shown a reticulate pattern throughout the nucleoplasm along which distributed clusters of variable size and intensity exist [21,22].

To resolve the spatial distribution of RNPII signals in *Arabidopsis* nuclei in 3D, we imaged RNPII and DNA using 3D-STED microscopy. To quantify RNPII foci distribution, we designed an image analysis workflow (Figure 1a and Supplemental File 1). Sample preparation and imaging are described elsewhere [23]. Deconvolved STED images are segmented using the Imapris software (Bitplane, Switzerland) to create digital objects corresponding to the nucleus, the nucleolus, the chromocenters and

the RNPII signals (Figure 1b-d, Supplemental File 1 – Video 1). The surface object corresponding to the nucleus is also used to apply a 3D mask to separate the true image from the background signal (compare the framed regions in Figure 1b-c). While the nucleus and nucleolus are segmented based on smoothed, manual contours, heterochromatin is segmented using the supervised automated tool. Chromocenters (CCs) are typically large, brightly stained regions. In *Arabidopsis* nuclei, these are discrete and relatively easy to segment (Figure 1d, inset d1). Super-resolution imaging revealed that additional heterochromatin regions, which we termed nanochromocenters (nanoCC), can also be segmented (Figure 1d, inset d2). RNPII signal shows a complex nuclear distribution in *Arabidopsis* nuclei: rather than being discrete, it spreads unevenly in a reticulated manner with, however, clearly identifiable local clusters [22]. Our aim was to segment the image to discretize RNPII signal and focus on the clusters, considering their variable size, to further analyze their variability in intensity, size and spatial distribution. We applied the growing spot function in an iterative manner and could capture 70–80% of the RNPII signal in spots of variable size (Figure 1e, inset e2). This stepwise segmentation resulted in a digital image composed of objects capturing the nucleus, the nucleolus, the chromocenters and RNPII clusters (Figure 1f). Variables of interest, such as signal intensity per channel, object size and shape and distance between objects (spot-to-spot, spot-to-surface) were exported for each object type and channel.

The high number of variables, object type, channels, image replicates and levels of comparison (such as genotypes and treatment) dramatically increases data complexity. To facilitate data exploration, we built a stand-alone data visualization interface named *DataViz* (<https://github.com/barouxlab/DataViz>) which allows one to interactively plot all, or a subset of, data. This also enables custom variable creation for the normalization of distances and intensity per image (Figure 1g-i, Supplemental File 1 – *Dataviz_guidelines*). Here, we provide a few examples of violin plots (Figure 1g), density distributions (Figure 1h) and scatter plots with

a Workflow 1 (overview)

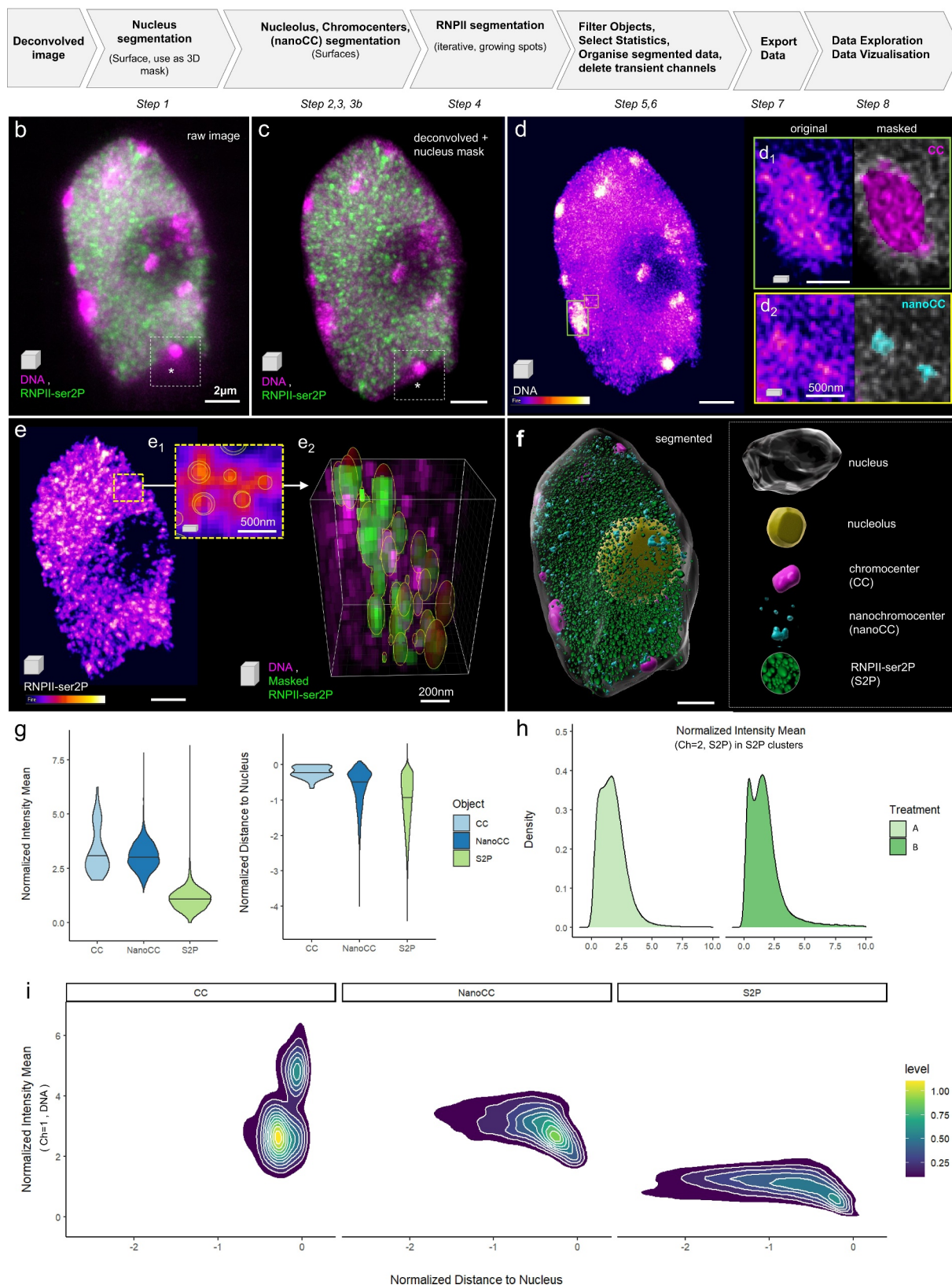


Figure 1. Analysis of the spatial distribution of RNA Pol II clusters in intact nuclei. (a) Overview of the workflow illustrated in b-i; (b) 3D projection of a 3D-STED image reporting on immunolabelled RNA Pol II (isoform phosphorylated on SerP, green, RNPII-ser2P) and DNA (magenta, Hoechst 580CP [26]), raw image; (c) Same image following deconvolution, nucleus contour segmentation and masking; (d) Intensity-coded coloring mode (Fire) of the DNA channel and frames magnified in the insets showing examples of

density contours (Figure 1i). The mean intensity, normalized per nucleus, of the DNA signal shows that the average and range of chromatin compaction in CC and nanoCC is largely similar, while nanoCC occasionally shows a higher compaction (upper tail of the violin plot, Figure 1g). By contrast, and as expected for transcriptionally active regions, chromatin is, on average, 2–3x less condensed in the RNPII-S2P clusters (Figure 1g). Also, plotting the shortest distance of each object to the nucleus surface (Figure 1g, right plot: the negative values indicate distance toward the nucleus interior), confirms the peripheral localization of CC as already described [24,25], an apparent enrichment of the nanoCC toward the periphery (although less pronounced than CC), and spreading of the RNPII-S2P clusters from the periphery toward the nuclear interior (with an apparent decreasing occurrence linked to the presence of the nucleolus). Further, plotting the density distribution of RNPII-S2P signals in the clusters (normalized mean intensity) allows detecting different structures of the RNPII landscape between different treatments (A and B in the example provided Figure 1h). Finally, DataViz enables exploring the relationship between two continuous variables using scatter plots, with or without density contours. In the example provided Figure 1i, we interrogated the relationship between the distance to the nucleus boundary and the mean DNA intensity for each of the nuclear domains segmented as CC, nanoCC and S2P clusters. The plots suggested (i) two categories of CC distinctive mostly by their intensity but slightly different with regard to their peripheral position and

that (ii) nanoCC and transcription clusters closer to the periphery are on average less compact than their counterparts located more toward the nuclear interior. These are only a few examples of the numerous possible plots that collectively contribute to data mining and discovery.

The segmentation process described in detail in the supplemental material corresponds to a user-supervised workflow. The input values (threshold, smoothing factor, or filtering values) are either software-defined values (and depend on image attributes) or customized by the user to best capture the biological objects. The parameters are then saved and re-applied for subsequent image replicate analyses. If the image quality is highly reproducible, it is further possible to apply automated batch-segmentation (following the software provider's instructions). For a trained user, the workflow takes *ca.* 45 min per image or less. Finally, this workflow can be further applied for the analysis of other types of nuclear signals showing punctate distribution similar to that in our example.

Analysis of the spatial distribution of proteins located at the nuclear periphery

To date, the distribution of nuclear envelope (NE)-associated proteins is poorly documented in plants. 3D microscopy-based observations may provide new insights into the organization of chromatin domains at the nuclear periphery at the single-cell level.

In this example, we developed a workflow to quantify the spatial pattern of a protein heterogeneously distributed within the NE (Figure 2a).

chromocenters (CC, d1) and nanochromocenters (nanoCC, d2) in the original channel (left) and after segmentation and pseudo-coloring (right); **(e)** Intensity-coded coloring mode (Fire) of the RNPII-ser2P channel showing a dense distribution of clusters with identifiable intensity peaks, enabling segmentation as adaptive spots (e1, e2), e1: single plane showing the spot contours; e2, 3D segment of the image after segmentation, clusters pseudo-colored in green, DNA in magenta. **(f)** Fully segmented image containing surface (nucleus, nucleolus, CC and nanoCC) and spot objects (RNPII-ser2P, abbreviated S2P). **(g-i)** Data exploration using *DataViz* (github.com/barouxlabs/DataViz, Supplemental File 1- *Dataviz_guidelines*). **(g)**, Violin plots showing a similar DNA density distribution in CC and nanoCC but much lower density in S2P clusters (intensity mean, DNA channel, normalized per image) and a sharp peripheral location of CC as formerly described (Andrey et al., 2010; Fransz et al., 2002), contrasting with the more dispersed distribution of nanoCC and S2P clusters (distance to nucleus surface (0) normalized using the nucleus center of mass as reference); **(h)** Example showing an application of the workflow, to compare the distribution of RNPII cluster intensities between two treatments: A and B. **(i)** Another example illustrating one of the many analyses enabled by the workflow and *DataViz*, with density scatter plots of DNA intensity means in RNPII clusters as a function of their distance to the nucleus surface. Scale bars: b-f, 2 μ m; insets, as indicated.

a Workflow 2 (overview)

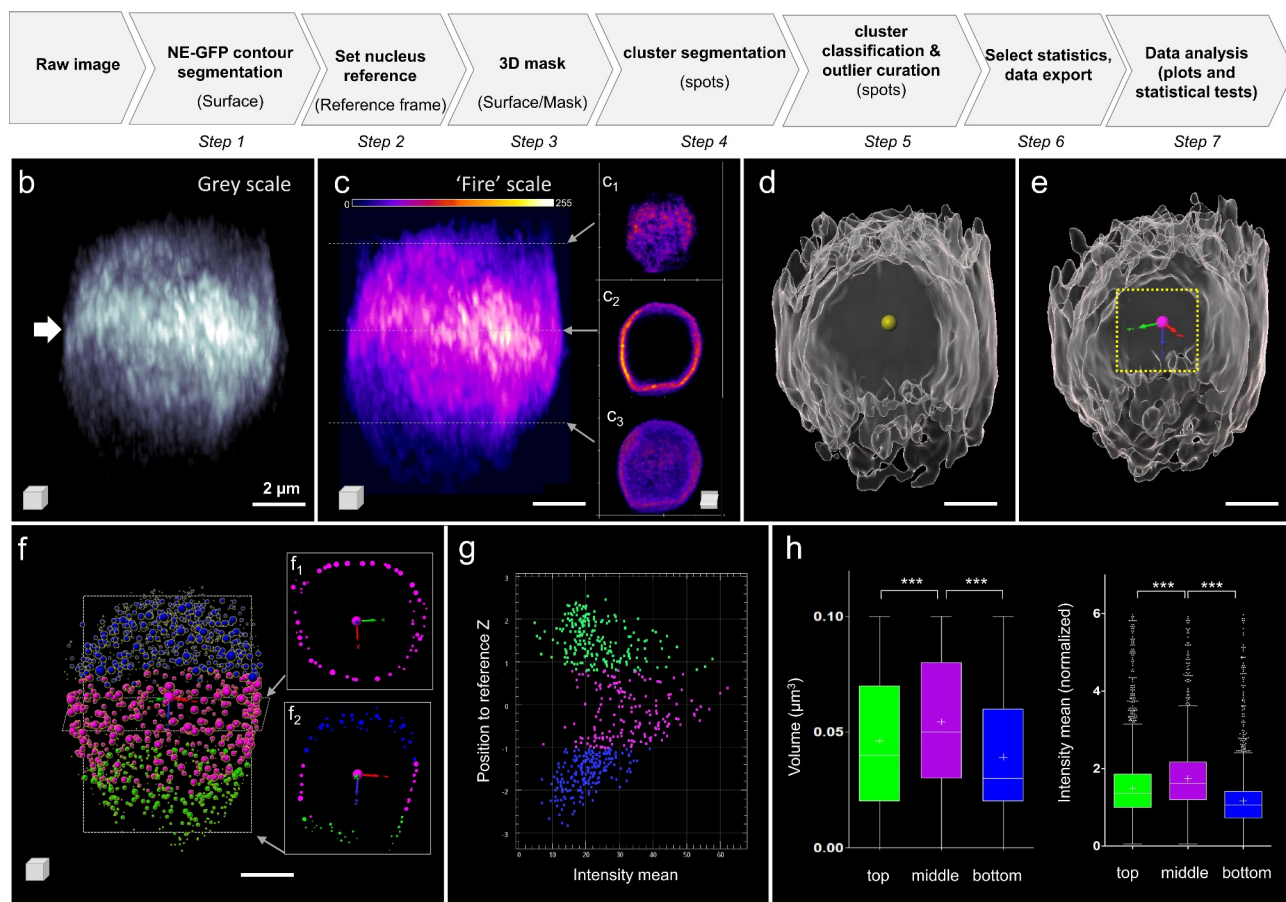


Figure 2. Analysis of the spatial distribution of a fluorescently tagged protein associated with the nuclear envelope. (a) Overview of the Image analysis workflow. Details of the parameters are in supplements. (b) Raw image of NE-GFP (Nuclear Envelope – associated protein fused to GFP) signal in a root nucleus; 3D rendering in gray levels suggests an enrichment of the protein at the equatorial region of the nucleus (white arrow). (c) Same image (3D) as in (b) using a fire color scale for NE-GFP signal intensities display (0–255); c1–c3 insets: cross sections at selected top, middle and bottom planes, respectively. (d) Result of the segmentation of the NE-GFP signal domain as a surface (gray); a spot (yellow) is created at the surface' center-of-mass. (e) A new XYZ coordinate system (reference frame) is docked at the center-of-mass. (f) The NE-GFP signal is segmented as spots of adaptive size ('growing spots') using the channel masked by the surface; spots are classified according to their axial (z) position, the equatorial region is defined $\pm 2 \mu\text{m}$ around the origin. Three spot classes are created located at the top, middle and bottom of the nucleus (blue, magenta, green, respectively). f1, f2 insets: XY and XZ sections. (g) The intensity mean of the spots is plotted as a function of their axial position (z) relative to the new reference frame for the image shown in (b-f). The colors indicate the 'top', 'middle' and 'bottom' classes, respectively. (h) The volume and normalized intensity mean of NE-GFP spots are plotted for each class, for $n = 8$ nuclei images segmented following this workflow. Kruskal-Wallis and Dunn's multiple comparison tests with bottom vs middle and top vs middle indicate statistically significant differences with $P < 0.001$ (***) for both variables. Scale bars: $2 \mu\text{m}$.

We imaged *Arabidopsis* root nuclei expressing a GFP-tagged protein associated with the NE (NE-GFP, *Tatout*, *Mermet*, *Boulaflous-Stevens*, unpublished) from 1 week old seedlings using a confocal microscope equipped with an Airyscan module [27] (Supplemental File 2-Figure 2). The NE-GFP protein is located at the NE and forms clusters of variable size; these clusters appear to be asymmetrically distributed (arrow, Figure 2b). Intensity-based

coloring of the signal confirmed the enrichment of NE-GFP at the equatorial plane of the nucleus, in contrast to that at the top and bottom poles (Figure 2c and insets). The first step in our procedure was to segment the global domain of NE-GFP signal using the 'Surface' function of Imaris (Figure 2d). Subsequently, we created a spot at the center of mass of the segmented NE-GFP surface (yellow spot, Figure 2d) and used it to create a 'Reference

frame' object (Figure 2e). This new XYZ coordinate system at the nucleus' center allows to classify the NE-GFP clusters at a later stage. The NE-GFP clusters are segmented as spots of adaptive size on the NE-GFP domain masked on the surface created at step 1 (Step 3–4, Supplemental File 2). Spots were classified into three categories (top:blue, middle:magenta, bottom:green) according to their axial position in the coordinate system defined at step 2 (Step 5, Figure 2f). The 'middle' class is defined by a region encompassing the origin of this coordinate system from -2 to $+2$ μm along the z-axis. The 'top' and 'bottom' classes capture the spots above and below this equatorial region, respectively. In addition, this step included curation of the segmentation results to (i) keep spots strictly located at the periphery (removing outliers located internally due to surface invaginations) and (ii) to select spots of biologically relevant size (up to 600 nm diameter, ~ 1.1 μm^3 ; detailed procedure in Supplemental File 2). A 2D-plot of the mean intensity of segmented NE-GFP spots according to their axial (x) position in this coordinated system revealed higher signal intensity among spots located at the equatorial plane ('middle' class, Figure 2g). The segmentation of multiple images supported this finding (Figure 2h). Importantly, as fluorescence intensities varied between images, the mean intensity of each spot was normalized, following export, using the mean intensity within the NE-GFP surface for each image (Figure 2h). This analysis revealed that both the volume and mean intensity of NE-GFP clusters in the equatorial plane ('middle' class) are significantly different from that of the clusters located at the polar regions ('top' and 'bottom' classes; Figure 2h, Kruskal-Wallis and Dunn's multiple comparison test with $P < 0.0001$ for all pairs).

In conclusion, this image analysis workflow enables quantification of the spatial heterogeneity of proteins associated with the nuclear envelope. In combination with mutant genetics, this approach enables one to assess the quantitative influence of candidate regulators and that of intrinsic (protein) domains on spatial protein localization.

Analysis of protein distribution on meiotic chromosomes

Meiosis is a special type of cell division occurring during sexual reproduction and enabling genetic recombination. During the first stage of meiosis, prophase I, homologous chromosomes align along their entire length by a protein structure called the synaptonemal complex (SC). This process is essential for crossover (CO) formation in many eukaryotes. Prophase I is itself divided into five substages – leptotene, zygotene, pachytene, diplotene and diakinesis. Each stage can be monitored by immunostaining specific proteins involved in SC formation. The most common targets are ASY1 (ASYNAPTIC 1) and ZYP1 (ZIPPER-LIKE 1) [28]. During prophase I, homologous recombination starts with the formation of SPO11-programmed DNA double-strand breaks (DSB) [29]. These DSBs are subsequently processed and recombinases such as DMC1 (DNA MEIOTIC RECOMBINASE 1) mediate strand invasion, essential for CO formation [30]. In barley, a large number of DSBs are formed [31], but only 13–22 (depending on the cultivar and scoring method) are repaired to crossover (CO), while the rest are repaired as non-crossovers (NCO) [32,33]. What controls the fate of DSB (CO vs NCO) is poorly understood. A current hypothesis involves HEI10 (HUMAN ENHANCER OF INVASION 10), a ZMM class-of-protein in the CO repair pathway, as an early indicator [34].

To elucidate whether HEI10 also contributes to DSB fate designation in barley, one approach is to elucidate the dynamics of HEI10 foci along prophase chromosomes at early, mid, and late stages, and in relation to DMC1 at early prophase. This approach requires 3D imaging of (immunostained) meiotic proteins on prophase chromosomes and the scoring of HEI10 vs DMC1 foci in relation to the prophase stage. We describe here a workflow to process 3D-SIM images to enable the scoring and classification of DMC1 and HEI10 foci depending on their size and intensity.

The workflow (Figure 3a) is illustrated with two images of barley male meiocytes labeled for components of the SC (ASY1, ZYP1), processed DSBs

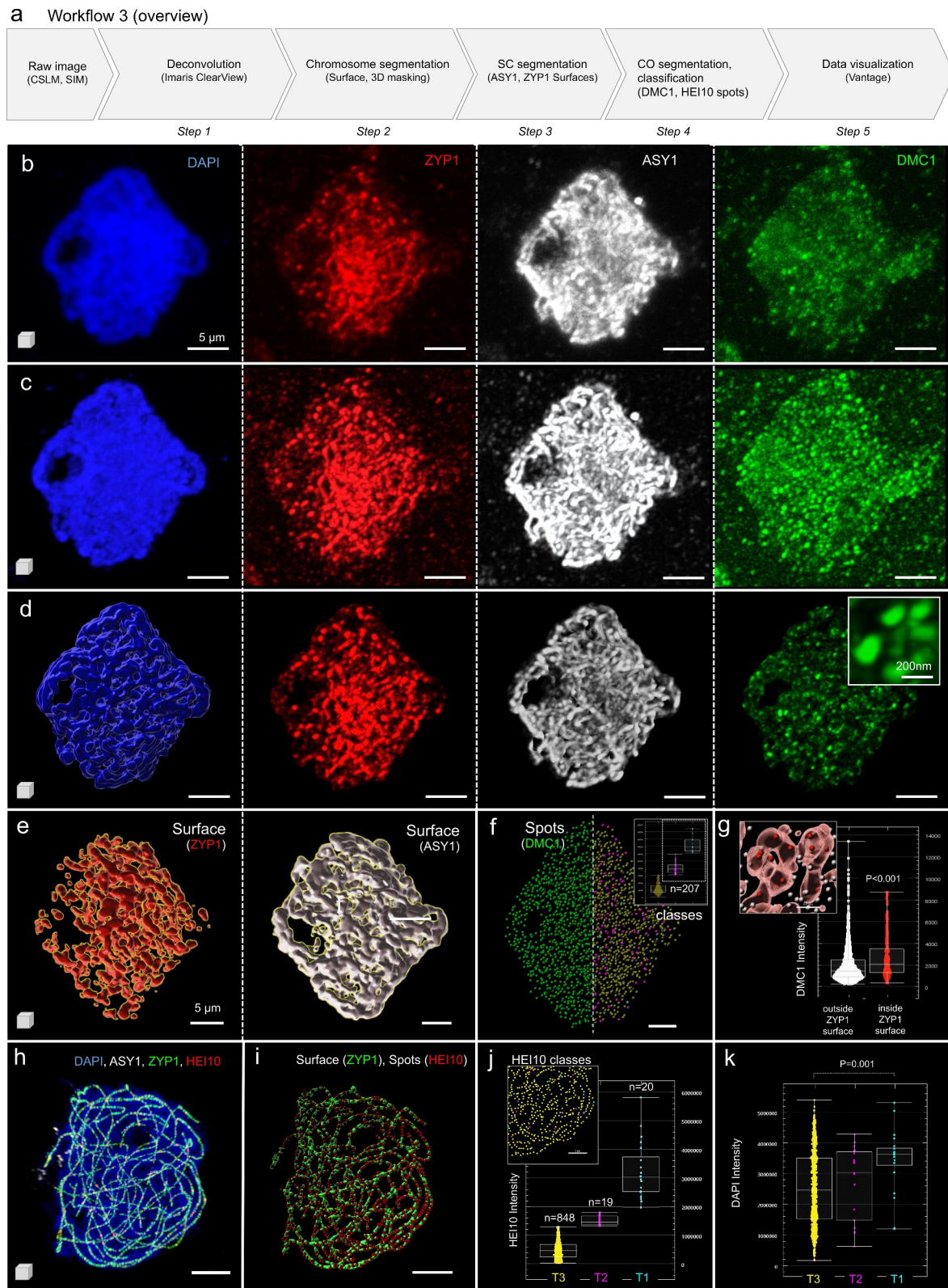


Figure 3. Analysis of crossover distribution in meiocytes. (a) Overview of the image analysis workflow in 5 steps illustrated on two images marking the synaptonemal complex (SC) and crossovers (CO) with different components (provided in Supplemental File 3): image 3a (b-g) represents a barley meiocyte at zygotene stage immunostained for DMC1, ZYP1 and ASY1 and counterstained for DNA using DAPI. The image was acquired by confocal microscopy (ZEISS LSM 710) as described (Colas et al., 2019). Image 3b (h-k) represents a barley meiocyte at the late pachytene stage immunostained for ASY1 (Ch = 2), ZYP1 (Ch = 3) and HEI10 (Ch = 4) and counterstained for DNA using DAPI (Ch = 1). The image was acquired by 3D-SIM as described previously (Hesse et al., 2019). (b) Original image acquired by confocal imaging, the different labeling are indicated.

(DMC1) and recombination intermediates (HEI10). The first image, shown in [Figure 3b-g](#) and provided in Supplemental File 3 – [Image 3a](#), shows a zygotene stage nucleus labeled with ASY1 (white), ZYP1 (red), DMC1 (green) and counterstained with DAPI (blue), was acquired on a confocal microscope (Zeiss LSM 710) as per Colas *et al.* [33]. The second image, shown in [Figure 3h-k](#) and provided in Supplemental File 3 – [Image 3b](#), shows a pachytene stage nucleus labeled with ASY1 (white), ZYP1 (green), HEI10 (red) and counterstained with DAPI (blue), was acquired using 3D-SIM similar as for rye [35]. The aim of both images was to segment HEI10 or DMC1 foci and to analyze their distribution relative to the SC, their size and their intensity. For this, the chromosomes, SC complex and HEI10 or DMC1 foci are segmented separately. The detailed strategies used for filtering and classifying the HEI10 or DMC1 foci are explained in the detailed workflow descriptions (Supplemental Files 3). In brief, the image analysis followed the steps of deconvolution (optional depending on the imaging method), chromosome segmentation, SC segmentation, CO foci segmentation and classification before data export ([Figure 3a](#)).

The effect of deconvolution is shown for the first image acquired by confocal microscopy to reconstruct the image at optical resolution (compare the panels [Figure 3b](#) and [3c](#)). This step is essential for properly estimating the CO diameter later ([Figure 3d](#), DMC1 channel inset). Next, the DNA (DAPI) staining was used to generate a 3D surface of the chromosomes serving as a mask to remove signal noise in the image (compare the panels [Figure 3c](#) and [3d](#)). Note that here, the aim was not to segment the chromosomes very precisely, as the masking

would result in the exclusion of ASY1, ZYP1 and DMC1 foci that do not entirely colocalize with DNA at that meiotic stage. Hence, permissive criteria were preferred in this case. Next, the SC complex was segmented on both the ASY1 and ZYP1 channels, creating two distinct surfaces ([Figure 3e](#), red: surface ZYP1, white: surface ASY1). Finally, DMC1 foci were segmented as spot objects using an estimated seed size of 200 nm ([Figure 3f](#)). The algorithm detects all possible foci with both low and high intensities. Classical studies have so far focused on high-intensity foci, whose abundance falls within a few hundred [31,33]. By contrast, the workflow described here enables one to capture all foci, first, irrespective of their intensity, and to classify them according to intensity, during the creation process ([Figure 3f](#), right panel). In this example, three classes were created ([Figure 3f](#) plot, yellow, magenta and cyan classes). Alternatively, spots can be classified after data export based on normalized signal intensity in a third-party software application (for instance, using DataViz, see Workflow1). In an intensity sum-based classification, we scored 217 DMC1 spots with medium-to-high intensity ([Figure 3f](#) plot, magenta and cyan classes) as previously reported for a similar stage of meiosis [31,33]. The remaining low-intensity spots ([Figure 3f](#) plot, yellow class) may correspond to either immunolabeling noise or unbound proteins. Next, we asked whether DMC1 localization was correlated with the SC. Indeed, following the classification of DMC1 spots in two groups, inside or outside the ZYP1 surface, we found a significant enrichment of DMC1 signal (based on intensity mean) when foci colocalize with ZYP1 ([Figure 3g](#)). This is one of the many

(c) image following deconvolution to resolve the SC and immunostained CO. (d) segmentation of the chromosomes as surface and masking of the ZYP1, ASY1 and DMC1 channels to remove background signal. It allows resolving DMC1 foci at high resolution (inset). (e) SC segmentation using the ZYP1 and ASY1 masked channels (f) DMC1 foci segmentation (left) and classification according to their intensity (right and inset = intensity plot per category), (g) classification of DMC1 foci according to their distance relative to the ZYP1 surface. (h) Original 3d SIM image (image 3b), (i) same image following ZYP1 and HEI10 segmentation, (j) HEI10 spots were classified according to their intensity (T1, T2, T3 on graph and inset); 20 foci were scored (automatic) for the T1 class as described in earlier studies, (k) HEI10 classes differ by the DNA density. Scale bars: 5 μ m except for the inset d, DMC1 channel (200 nm), Plots (f, g, j, k): Imaris Vantage.

examples of correlative analyses that can be carried-out in such segmented images.

The second image (Figure 3h) was analyzed similarly, but deconvolution, chromosome segmentation and masking were omitted in this case. The ZYP1 surface (Figure 3i, green) was used to mask the HEI10 channel to specifically focus on HEI10 foci (Figure 3i, red) colocalizing with ZYP1. HEI10 spots objects were then classified according to their intensity, considering notably the first and next 2% quantile versus the rest to create three classes, T1, T2 and T3, respectively (Figure 3j). This approach was formerly described to analyze CO distribution during meiosis in a fungal species [36]. The surprisingly high number of low-intensity HEI10 foci (T3 class) detected by the segmentation in this late pachytene-stage nucleus suggests the need for further investigation to understand their nature and possible function. To further describe the properties of HEI10 classes, we investigated different relationships and found that in most cells, typically high-intensity HEI10 foci (T1) localize, on average, on chromosome regions with higher DNA compaction (DAPI mean intensity) compared to low-intensity HEI10 foci (T3) (Figure 3k).

This image processing workflow facilitates the scoring of class I CO and NCO foci across multiple images, stages and genotypes, a task largely done manually until now. In addition, segmentation is near-exhaustive and includes low-intensity foci that were discarded from manual scoring in former studies. This raises the question of the dynamics of HEI10 and DMC1 foci formation, with possible intermediate stages represented by low-intensity foci. In addition, it opens the possibility to refine the analysis of CO/NCO spatial organization and their fine-scale structure. For instance, the localization of CO/NCO foci can be measured relatively to the SC components as a function of their intensity, and as a function of local chromatin compaction.

Analysis of nuclear speckle distribution

A distinguishing feature of nuclear topography is the ability to accommodate a variety of subnuclear compartments including nuclear bodies. Nuclear bodies are membraneless compartments

that spatially partition the nuclear environment and are thought to facilitate enzymatic reactions [37,38]. Similar to membrane-bound organelles, they maintain an effective steady-state structure, but likely by different mechanisms [39]. The first-identified and best-characterized plant nuclear bodies are the nucleolus and Cajal bodies. Several other smaller structures have, however, also been identified, including speckles, paraspeckles, coiled bodies and photobodies [40–42]. Unmasking the mechanisms by which cells assemble, maintain and regulate nuclear bodies and speckles, and the environmental and developmental factors contributing to the process, will shed light on their biological functions. For instance, splicing regulator (SR) proteins in plants localize as speckles, the size and shape of which are dependent on cell type, metabolic state and transcriptional activity [41–43].

One way to elucidate the speckle dynamics of nuclear bodies, which are not membrane-bound, is through microscopy imaging and image analysis. This approach enables the analysis of their spatial distribution and their composition relative to other nuclear components and DNA (chromatin) density. In this example, we showcase a simple image analysis workflow for analyzing the distribution of nuclear speckles and bodies. We used two images: Supplemental File 4 – image 4a reports on the nuclear localization of a plant chromatin remodeler: a SWI/SNF subunit (called SSSU here) forming nuclear speckles in leaf nuclei. Supplemental File 4 – image 4b reports on the nuclear localization of a mammalian chromatin protein (here called CP) and of H3K27me3 forming large nuclear bodies in nuclei of mouse naive pluripotent embryonic stem cells [44]. CP is a Baz-related subunit of the ISWI (Imitation SWItch) family remodeling complex factor, interacting with SNF2H, a SWI/SNF related remodeler [45] (Santoro, Panatta, unpublished).

SSSU was found to interact with PWO1 and CRWN1 (Kalyanikrishna, Jourdain, Schubert, unpublished), a set of proteins involved in epigenetic gene regulation and chromatin organization at the nuclear periphery [46]. CRWN1 (CROWDED NUCLEI 1), a nuclear lamina candidate in Arabidopsis, interacts with PWO1 (PROLINE-TRYPTOPHANE-TRYPTOPHANE-PROLINE

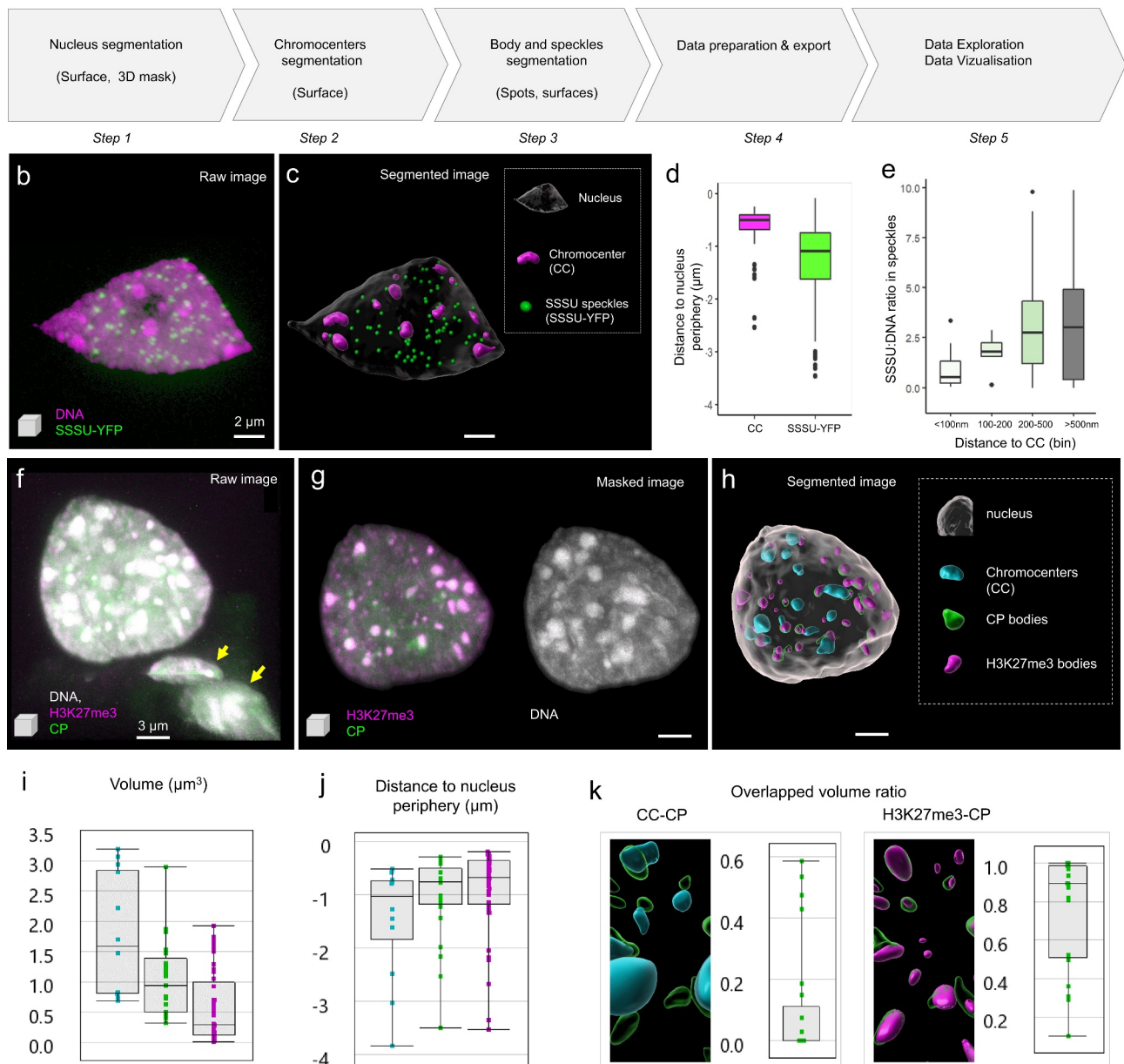
a Workflow 4 (overview)


Figure 4. Analysis of the spatial distribution of nuclear speckles and bodies. (a) Overview of the image analysis workflow, details and training images are provided in Supplemental Files 4. The analysis of two images (Supplemental File 4 – image 4a and 4b) representing plant and animal nuclei are shown in (b-e) and (f-k), respectively. (b) Raw, STED image (3D projection) showing an isolated leaf nucleus stained for DNA (magenta, Hoechst 580CP [26],) and immunostained for SSSU (green). (c) Segmentation result: the nucleus, chromocenters (CC) and the nuclear speckles (SSSU) were segmented as surface objects (legend, right panel). (d) The position of CC and SSSU speckles was plotted relative to the nucleus' periphery defined by the surface's boundary (0 = at the boundary; negative values = toward the interior), $n = 9$ nuclei analyzed. (e) The relative enrichment of SSSU on chromatin was plotted as the SSSU:DNA mean signal intensity ratio for different classes of speckles defined by their distance to CC (in μm). Plots were generated using Dataviz (see Workflow 1) using data from $n = 10$ segmented nuclei. (f) Confocal image (3D projection) of a nucleus from a mouse naïve pluripotent embryonic stem cell stained for DNA (gray, DAPI), immunostained for the chromatin protein under study (CP, green) and H3K27me3 (magenta) forming large nuclear bodies; the arrows show truncated nuclei in the field of view undesirable for downstream analyses and eliminated upon masking at the next step. (g) Same image after 3D masking using the nucleus surface created at step 1. (h) Results of image segmentation: the nucleus, chromocenters (CC) and the nuclear bodies (CP and H3K27me3) were segmented as surface objects (legend, right panel). (i-k) Quantitative analysis of CC and nuclear bodies: volume: (i) distance to the nucleus periphery (j) and overlapping volume ratios (k, left: CC and CP overlap, right: CP and H3K27me3 overlap). Plots were generated using Imaris Vantage. Scale bar: (a-b), 2 μm ; (f-h), 3 μm .

INTERACTOR OF POLYCOMBS1), a plant-specific protein associated with histones and PRC2 (POLYCOMBREPRESSIVE COMPLEX 2) [46]. Due to its possible interaction with CRWN1, we asked whether SSSU is also located preferentially at the nuclear periphery. To answer this question, we tagged SSSU with YFP (YELLOW FLUORESCENT PROTEIN) and imaged nuclei expressing SSSU-YFP using STED microscopy. The image analysis workflow consists of only a few steps (Figure 4a): STED images reporting on the immunolabeled SSSU-YFP and DNA counterstaining (Figure 4b) were segmented for the nucleus, chromocenters (CC) and SSSU-speckles, using the surface tool. For segmentation of the nucleus, smooth, manual contours were used, while for segmenting CCs, automated, parameter-controlled settings were applied. SSSU speckles were segmented as spot objects of ca. 200 nm diameter. Segmentation data of several images were exported and plotted using DataViz (see workflow 1, Supplemental File 1 – [Dataviz_guidelines](#)). SSSU-YFP speckles showed a broad spatial distribution, with no clear preferential enrichment toward the periphery (Figure 4d), in contrast to chromocenters as previously shown [24,25]. We found, however, that SSSU speckles are not uniform: they differ in their relative enrichment (SSSU:DNA ratio), which correlates with the proximity to CC (Figure 4e). Our analysis demonstrates that the nuclear speckles formed by SSSU are not preferentially enriched at the nuclear periphery as would have been expected from their biochemical interaction with CRWN1. The analysis suggests a differential enrichment depending on the proximity to other nuclear bodies, the CC, a relationship whose functional relevance remains to be investigated. This preliminary finding was unexpected and was revealed thanks to the possibility to explore multiple relationships between distance and intensity measurements in DataViz using segmentation data generated using this workflow.

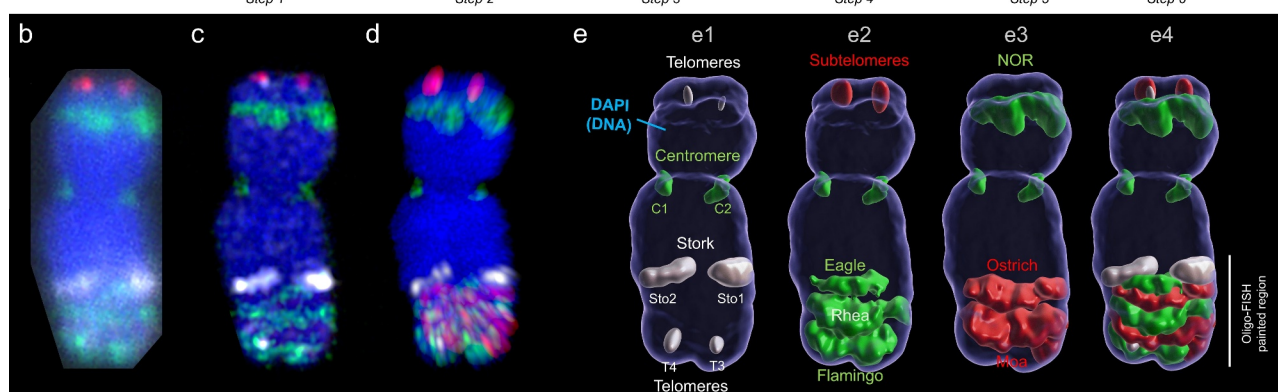
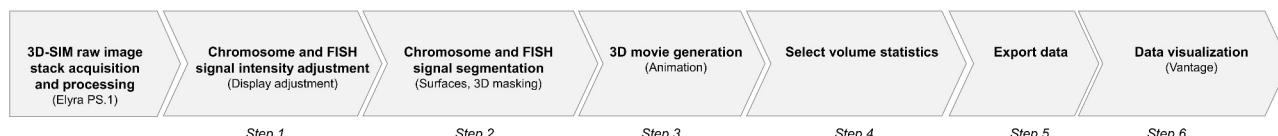
In the second example, we were interested in the CP protein localization relative to the repressive nuclear compartments formed by heterochromatin (chromocenters) and H3K27me3 in nuclei of mouse naive pluripotent embryonic stem cells. Nuclei stained for DNA and immunostained for CP and

H3K27me3 were imaged at high resolution by confocal microscopy (Figure 4f). To analyze the distribution of CP bodies, we segmented the nucleus, the chromocenters (CC), CP and H3K27me3 nuclear bodies, as surfaces of adaptive size (Figure 4g-h). Volume measurements show that CP bodies are smaller than CC but larger than H3K27me3 bodies (Figure 4i, $p < 0.001$, Wilcoxon test) and are similarly distributed toward the periphery compared to CC and H3K27me3 bodies (Figure 4j). The image shows an intricate relationship between CP bodies, CC and H3K27me3 bodies. Measuring the overlapped volume ratio is a useful approach to quantify the fraction of spatially colocalizing bodies (Figure 4k), revealing in our case a frequent overlap of 50% or more of CP bodies with H3K27me3 bodies. Conversely, the overlap with CCs is less frequent and occurs to a lower extent (<20%). This image analysis workflow thus allows one to quantify features of the nuclear body distribution that are otherwise underappreciated with qualitative data alone. Based on this simple workflow, further processing steps can be implemented that would contribute to a refined analysis of the spatial pattern of CP proteins relative to chromatin density and H3K27me3 levels. This can include, for instance, the creation of intensity-based colocalization or ratio channels (not shown).

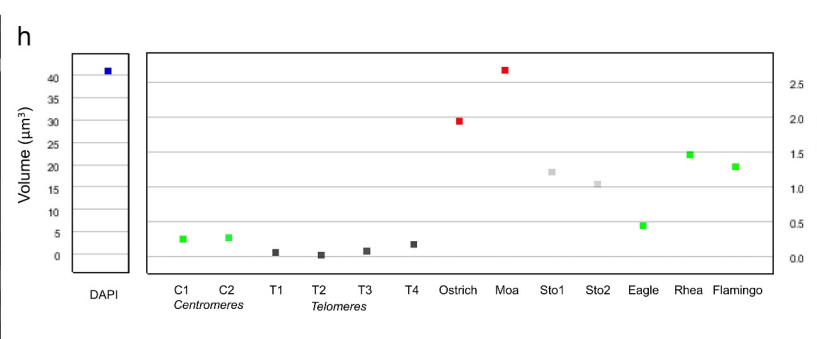
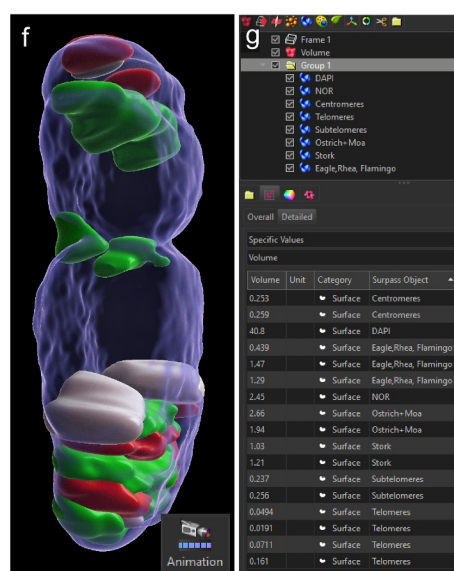
Analysis of the higher-order chromatin organization in mitotic chromosomes

During mitosis, chromosomes reassemble into compact bodies resulting from increased chromatin fiber looping within the chromatids [47]. How sister chromatids resolve into distinct structures and which topological rearrangement contributes to the final organization start being understood. Yet, questions remain concerning the molecular mechanisms and the regulation of this dynamic process [47]. Also, whether the topological arrangement in mitotic chromosomes is conserved during evolution is not well known and is motivating for comparative investigations in less-well-studied models [48].

a Workflow 5 (overview)



b 3D-SIM raw data (Single slice) **c** 3D-SIM processed (Single slice) **d** Signal intensity adjusted (3D rendering) **e** Chromosome and FISH signals segmented



h Data visualization (Vantage)

Figure 5. Analysis of the metaphase chromosome ultrastructure using volume measurement of oligo-FISH labeled regions.

(a) Overview of the image analysis workflow. (b) 3D-SIM raw image slice from a stack containing 30 slices at widefield resolution. (c) 3D-SIM processed image slice showing increased super-resolution. (d) Display adjustment to optimize the visualization of signals with varying intensities. (e) Segmentation results: the chromosome is segmented using the DAPI channel and the generated 3D surface is used as a mask to specifically retain chromosomal FISH signals and exclude the background. The segmentation is presented sequentially for different FISH probe groups (e1-e3), and the result is shown in the merge (e4). e1, telomere, centromere, and Stork probes; e2, Subtelomeres, Eagle, Rhea and Flamingo probes; e3, 45SrDNA (Nucleolus Organizing Region, NOR), Ostrich and Moa probes. The Oligo-FISH probes label the bottom part of chromosome 5HL. (f) Side view of a 3D movie generated via the 'Animation' tool (Supplemental File 5 – video 1). (g) Volume data are read in the 'Statistics' Tab for selected surfaces. (h) Data visualization using the 'Vantage' tool for individual objects (top).

Oligo-FISH combined with spatial super-resolution structured illumination microscopy (3D-SIM) is a useful approach for resolving helical versus non-helical arrangement of chromatin fibers in

chromatids. For instance, this method allowed us to confirm that the chromatids of barley metaphase chromosomes are formed by a helically wound ~400 nm chromatin fiber, the so-called

chromonema [49]. Additionally, by measuring the volume of oligo-FISH painted regions and based on the DNA quantity used for the probes, it was possible to calculate the chromatin compaction. With this approach, different chromatin densities were found along the barley chromosome arm 5 HL. Interstitial arm regions were ~ 1.7 times more compact than regions adjacent to the subtelomeres (34.1 vs. 19.5 Mb/ μm^3 , respectively) [49].

Workflow 5 describes the processing procedure to segment an individual 5 H chromosome and the different FISH signals to obtain quantitative measurements on the degree of chromatin compaction (Figure 5a; Supplemental File 5). In this example, centromeres, 45SrDNA (NOR, nucleolus organizing regions) telomeres, and subtelomeres of somatic metaphase chromosomes were labeled with specific FISH probes as described [49]. In addition, half- and full helical turns of the chromonema were painted by oligo-FISH at the long arm of chromosome 5H (Figure 5, probes were named according to birds: Stork, Eagle, Ostrich, Rhea, Moa, Flamingo) [49]. 3D-SIM raw data image stacks (Figure 5b) were acquired using an Elyra PS.1 microscope system equipped with a 63 \times /1.4 Oil Plan-Apochromat objective, processed with the software ZENBlack (Carl Zeiss GmbH) (Figure 5c) [50] and converted into an Imaris file. DAPI and FISH signal intensities were adjusted for improving the visualization using the 'Display Adjustment' tool (Figure 5d). The DAPI-labeled chromosome was segmented using the surface tool, and the surface was used to mask the image to remove the background signal outside this region of interest. Additional surfaces of the other, differently colored FISH signals were generated (Figure 5e-f, Supplemental File 5 – Video 1). The surface volume data were established (Figure 5g), exported for further analysis by compiling several images, and used to calculate the volumetric density of the different FISH-labeled regions along the chromosome [49]. An example plot for one chromosome is shown in Figure 5h using Vantage.

Analysis of centromere and telomere positioning

Arabidopsis and barley are eukaryotic models contrasting in their 3D interphase chromosome

organization. Arabidopsis has a small genome of about 157 Mbp per haploid DNA content (1C) packed into 5 chromosomes ($2n = 10$), whereas the barley genome is large, with around 5.1 Gbp/1C divided into 7 chromosomes ($2n = 14$) [51,52]. In Arabidopsis, centromeres are distributed relatively equally around the nuclear periphery to which they are attached, while telomeres are associated with nucleoli and each chromosome occupies a discrete territory within the nuclear space [53]. In barley, interphase chromosomes are organized in the so-called Rab1 configuration with the centromeres and telomeres clustered at opposite nuclear poles [52]. While the Rab1 configuration has long been thought to be prevalent among monocot species, recent studies show that it also occurs in dicot species and that variations exist within the same phylogenetic group [54]. In addition, this peculiar organization can occur in a tissue-specific manner, as in rice [55]. To better characterize the occurrence of Rab1 vs. non-Rab1 configurations and their possible intermediates, in different species and tissue types, there is a need to define an image analysis workflow quantifying telomere and centromere distribution in the nuclear space. We present such a workflow (overview Figure 6a) illustrated with two examples, corresponding to studies of chromosome organization in a monocot species (barley, Figure 6b-f) and in a dicot species (*Limnanthes floccosa* subsp. *bellingermaniana*, Figure 6g-j). Details, parameters, and demo images are available in Supplemental Files 6.

A first example is given for barley nuclei (Figure 6b-f). Nuclei extracted from seeds (Figure 6b) were flow-sorted as described [56] and labeled by FISH using fluorescently labeled oligoprobes (Cy3-labeled *CEREBA*-centromeric repeat; [57] and Cy5-labeled Arabidopsis-type telomeric repeats [58]). Z-stack images were acquired with an epifluorescence microscope connected with a spinning disk (Andor, Oxford Instruments, UK). Centromeric and telomeric FISH signals and the DNA counterstain (DAPI) were pseudo-colored in magenta, yellow, and gray, respectively. Two types of seed nuclei are shown (Type I, Type II, Figure 6c). Images are first

a Workflow 6 (overview)

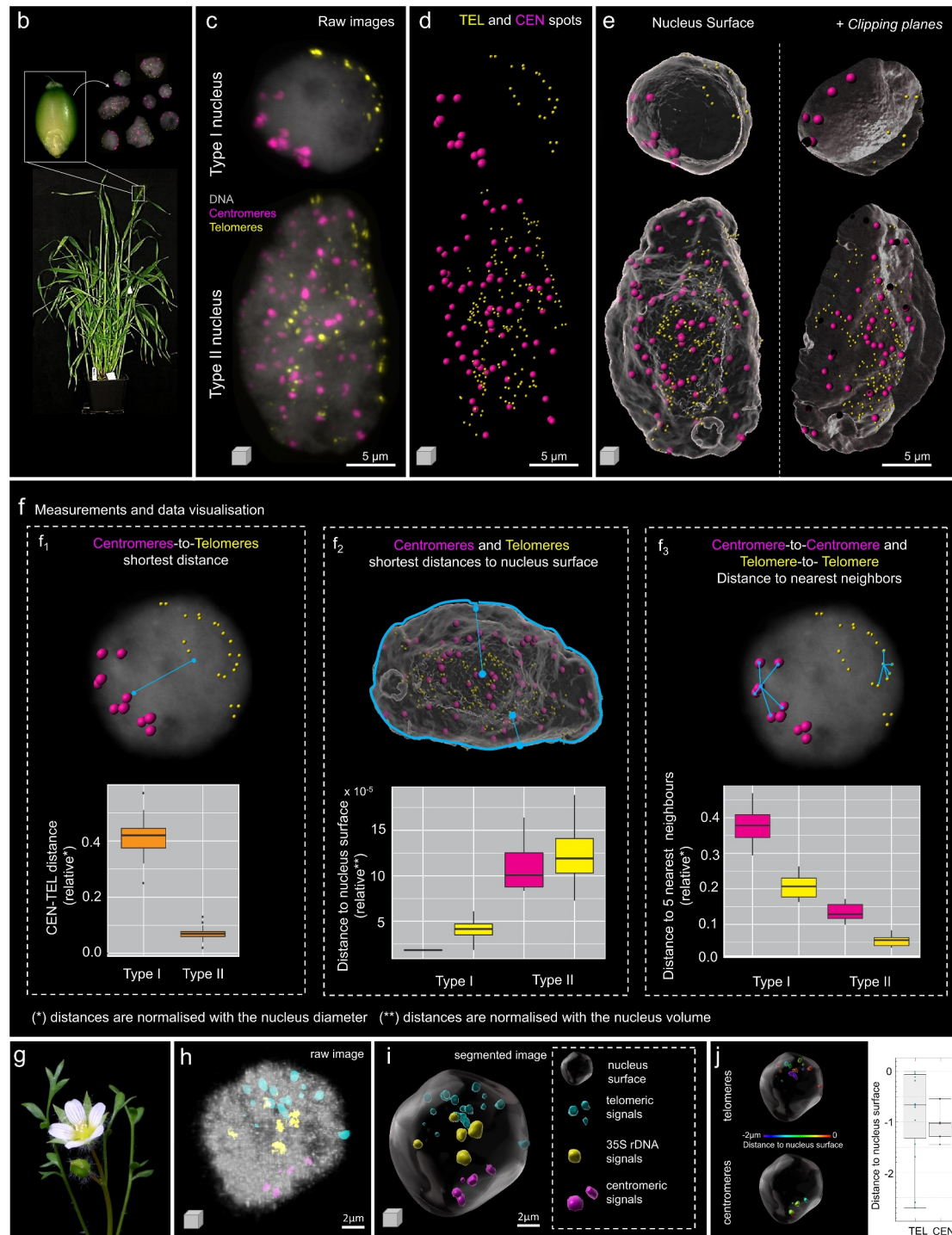
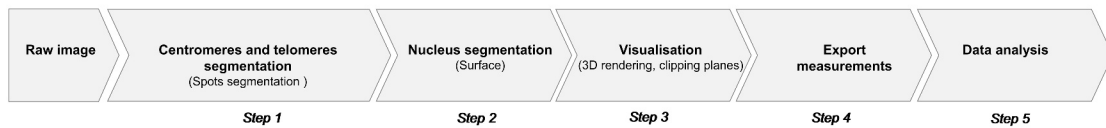


Figure 6. Analysis of centromere and telomere positioning in the interphase nucleus (continued). (a) Workflow overview showing the main steps to process the 3D image and identify centromeres and telomeres and their position in an interphase nucleus. The workflow is illustrated with seed nuclei from barley (a-f) and leaf nuclei from *Limnanthes* (g-i). (b) Barley plant, seeds and isolated nuclei stained by FISH for centromere and telomeric repeats (see main text for details). (c) Raw images (3D projections) of type I and type II nuclei showing centromeric (magenta) and telomeric (yellow) FISH probes signals, counterstained for DNA (DAPI, gray). (d) Telomeric (TEL) and centromeric (CEN) signals were segmented as spots. (e) 3D rendering together with nucleus surfaces (gray)

segmented on the channels reporting on FISH signals to create spot objects corresponding to centromeres (CEN) and telomeres (TEL), (Figure 6d) using the automated tool. The spot diameter is adjusted to the average size of FISH foci (ca 300 nm). The nuclear surface is rendered using a low smoothing factor (Figure 6e). For a better visualization of the spot distribution inside the nucleus, the surface is set to transparent or can be digitally sectioned using a clipping plane (Figure 6e). This segmentation and 3D visualization approach allowed us to realize that the seed nuclei population was composed of two categories of nuclei. In type I nuclei, centromeric and telomeric spots are grouped to opposite sides of the nucleus, reflecting Rab1-like features. In type II nuclei, they distribute in the whole 3D nuclear space, which corresponds to a non-Rab1 configuration. To support this observation by quantitative measurements, we exported three types of distance measurements (Figure 6f): (i) shortest distance between centromeric and telomeric spots (Figure 6f₁), (ii) shortest distance of centromeres and telomeres to the surface, corresponding to the nucleus border (Figure 6f₂), and (iii) average distance to top five neighboring spots for each group (centromeres, telomeres, Figure 6f₃). Because distances depend on the nucleus size, we normalized them using the nucleus diameter (graphs shown in Figure 6f express relative distances). The quantitative analysis shown in Figure 6f based on ca. 20 nuclei supported a contrasted spatial distribution of telomeres and centromeres in the two categories, with notably clear segregation of telomere and centromere groups in Type I nuclei (f1), located closely to the nuclear surface (f2). We

also noticed a shorter distance between telomeres and centromeres in Type II nuclei, which was unexpected. Because this type of nuclei is frequently highly endoreduplicated, this led us to investigate further the relationship between ploidy and chromosomal organization (Nowicka, Pecinka et al., submitted).

A second example is shown using nuclei from *L. floccosa* subsp. *bellingermana* (Figure 6g-j). Nuclei extraction from different types of tissue, FISH protocol and imaging were previously described by [54,59–61]. A similar procedure was applied to segment the nucleus based on DAPI staining (gray) and FISH signal reporting on the telomeres (cyan), centromeres (magenta) and 35S rDNA loci (yellow) (Figure 6h-i). In this example, centromeres and telomeres clearly showed clustering toward the nuclear periphery as shown with a median distance of spots around 0.6 μm (TEL) to 1 μm (CEN) in a nucleus of ca. 12 μm diameter (Figure 6j). We used this workflow for the analysis of nuclear organization in Crucifer genomes [54], in seven diploid species with up to 26-fold variation in genome size. This allowed to unveil species-specific patterns in nuclear organization [54].

For a trained user, the workflow takes approximately 20 minutes or less per image. This workflow can be used to compare the spatial distribution of chromosomes at interphase using centromeres and telomeres as references. Distance measurements across image replicates offer the possibility to detect quantitative differences invisible to the eye, between tissue types and cell types and to characterize potential mutant phenotypes in genetic analyses.

following segmentation, whole nuclei (left) or clipped (right), exposing the CEN and TEL signals in the interior of the nucleus. (f) The distribution of telomeres and centromeres is described according to three measurements derived from spot-to-spot or spot-to-surface statistics: shortest distance between centromeres and telomeres (f1), shortest distance of centromeres to the nucleus surface and shortest distance of telomeres to the nucleus surface (f2), inter-centromere and inter-telomere distances computed as the average distance to the nearest 5 neighbor spots of the same category (f3). In blue, schematic representation of the measured distance. Distances were exported and normalized to the nucleus diameter (f1, f3) or nucleus volume (f2) and plotted using the ggplot GUI online tool (<https://shiny.gmw.rug.nl/ggplotgui/>). The lower and upper hinges of the boxplots correspond to the first and third quartiles of the data, respectively, the black lines within the boxes mark the median. Five to ten nuclei were used for each measurement. Black spots beyond the whiskers represent outliers. (g-j) Illustration of the workflow on a *Limnanthes* leaf nucleus, (g) *Limnanthes floccosa* subsp. *bellingermana*, (h) Raw image (3D projection) of a nucleus stained for centromeric repeats (magenta), telomeric repeats (cyan) and rDNA repeats (yellow) by FISH, counterstained for DNA (DAPI, gray), imaged by confocal laser scanning microscopy, (i) 3D nucleus following segmentation of FISH signals and DNA as surfaces. (j) Distance of the different segmented groups relative to the nucleus surface were plotted in Imaris Vantage; images showing a distance-coded coloring are shown for centromeres (CEN) and telomeres (TEL).

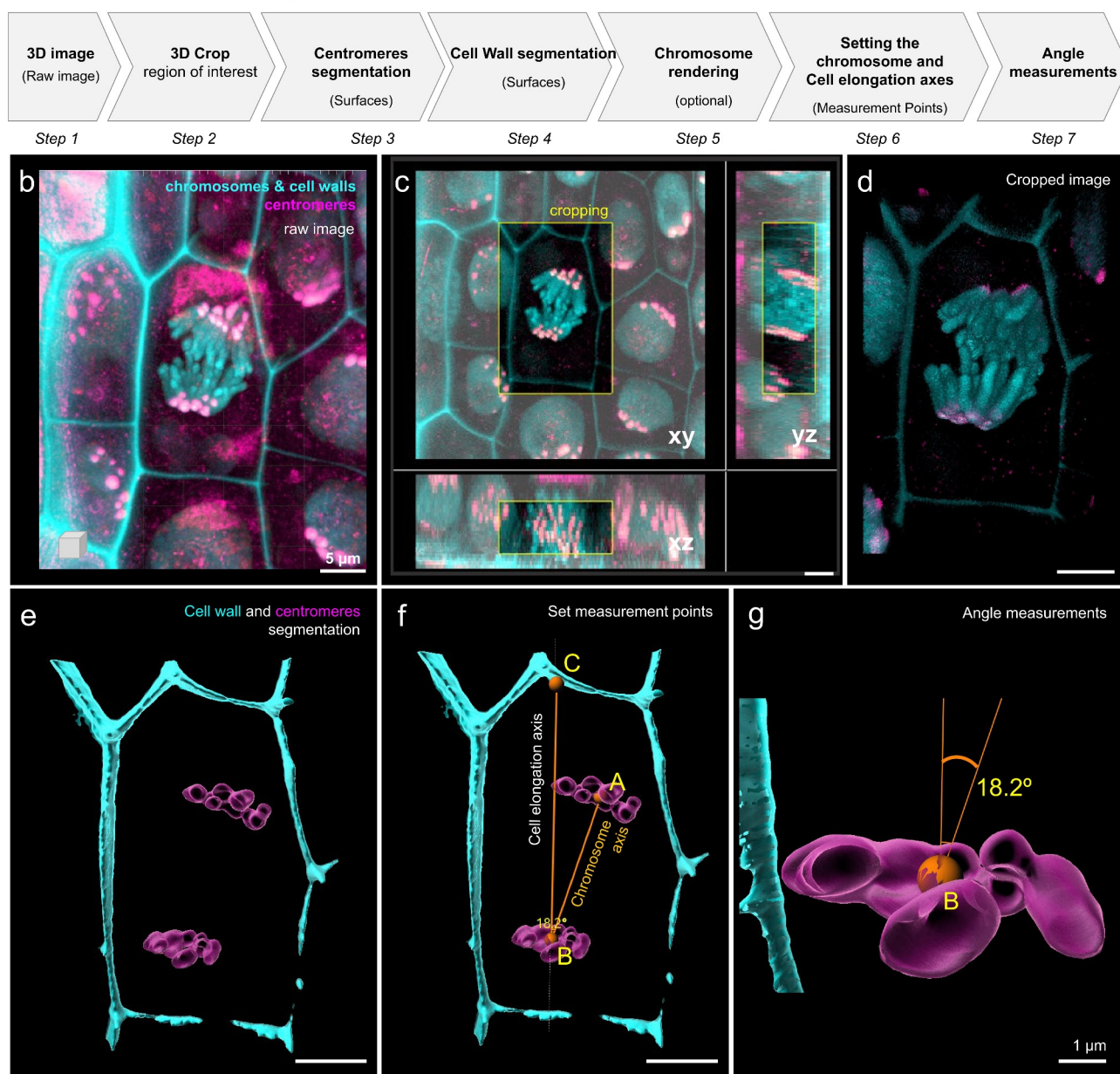
a Workflow 7 (overview)

Figure 7. Division angle measurement using surface-rendered cellular structures in living barley root cells. (next page).

(a) Workflow overview showing the sequence of tasks to process a raw picture up to the setting of measurement lines within the 3D cell space. (b) Confocal imaging of barley root tissue from a young seedling expressing CFP-H2B marking the chromosomes (cyan) and RFP-CenH3 marking the centromeres (magenta). In addition, cell wall autofluorescence upon UV excitation was used to mark the cell's boundaries (cyan). The image is a partial projection from a z-stack. (c) 3D cropping of the image to select a region of interest containing a dividing cell in mitotic anaphase (yellow frame). Orthogonal projections are shown in xy, yz and xz. (d) The cropped image is rendered in 3D using the 'blend' mode. (e) 'Surface' rendering of segmented centromeres (magenta) and the cell wall (cyan). (f) Setting of 'Measurement points' and their connective lines. AB defines the axis along which chromosomes are pulled (orthogonal to the chromosome plates), BC defines the cell's elongation axis. (g) Detailed visualization of the lower metaphase plate and angle formed between both axes defined by AB and BC measurement lines. The angle is measured in 3D by Imaris. Scale bars: b-f, 5 μ m; g, 1 μ m.

Analysis of mitotic chromosome orientation during division

Mitosis is the process by which organisms increase the number of cells. In plants, the highest number of mitotically active cells can be found in the root and shoot apical meristems (RAM and SAM, respectively) [62]. We focused the analysis on chromosome organization and orientation in living barley roots. Both cell division orientation and cell elongation contribute to the oriented growth of the root. Changes in the mitotic division orientation affect root shape and anatomy [63]. In *Vicia faba*, chromosome positioning correlates with the cell division plane and ultimately cell shape [64]. Notably, it was speculated that cell size could be a limiting factor forcing the spindle axis to be tilted, deviating slightly from the main axis of cell and organ elongation. Analyzing the orientation of mitotic chromosomes during cell division is thus relevant to understand this intricate relationship.

We designed a 3D microscopic image analysis workflow described in Figure 7a and detailed in Supplemental Files 7 containing a protocol and troubleshooting tips. We used barley chromatin and centromere fluorescent marker lines (FMLs) expressing translational fusions of histone H2B with CYAN FLUORESCENT PROTEIN (CFP-H2B) and -CENTROMERIC HISTONE H3 with RED FLUORESCENT PROTEIN (RFP-CENH3), respectively (Kaduchová, Pecinka et al., in preparation). Z-stack images were acquired using a Leica TCS SP8 STED3X confocal microscope equipped with a Leica Application Suite X (LAS-X) software version 3.5.5 with a Leica Lightning module (Leica, Buffalo Grove, IL, USA) (Leica Microsystems, Wetzlar, Germany). In addition, we took advantage of the fact that barley cell walls have an autofluorescence detectable in CFP emission spectra [65], allowing simultaneous visualization of chromosomes, centromeres, and cell walls. Centromere signals were pseudo-colored in magenta, chromatin with cell walls in cyan. The raw image (Figure 7b) presenting several cells in the root was cropped around one cell showing chromosomes at anaphase (Figure 7c). Centromeres were segmented with the ‘spots’ tool

(Figure 7d). Chromosomes and cell walls were segmented using the ‘surface’ tool (Figure 7e). Using the tool ‘Measurement point’, we created spots (connected by a measurement line) at key positions, providing information on the cell elongation axis (A-B), on the pulling axis of the chromosomes (A'-B) and a reference axis (B-C) (Figure 7f, see Supplemental File 7 for detailed explanation), which allowed for angle measurements (Figure 7g).

For a trained user, the workflow takes approximately 30 min per image. This workflow will allow one to measure the relationship between the orientation of the spindle axis during division and cell shape (elongation) and its variation between tissue and cell types. In addition, the possibility to measure this relationship opens the possibility to quantify the effect of genetic or environmental factors with large or subtle effects on the cell division axis.

Conclusive remarks

We present here a set of seven image analysis workflows enabling the quantitative study of the spatial organization of chromosomes and chromatin components. The workflows cover applications for studies at interphase (workflows 1, 2, 4, 6), mitosis (workflow 5, 7) or meiosis (workflow 3). Workflows 1, 2 and 4 demonstrated the possibility to discover spatial distribution patterns, taking as examples transcription clusters, nuclear bodies and speckles and nuclear envelope-associated proteins. Such patterns were revealed thanks to the exploration of possible relationships between distance and intensity measurements among the different objects of the segmented images. Workflow 6, exploring genome organization at interphase, illustrates the quantitative power of image segmentation to precisely measure the spatial positioning in the nuclear space and the clustering of telomeres and centromeres. These features describe different types of 3D genome organization depending on cell type and species. The interest in performing image analysis for chromosome studies was further illustrated with workflows 3 and 5 focusing on condensed

chromosomes at meiosis or mitosis, respectively. Workflow 1 demonstrates the usefulness of image segmentation for quantifying the number and distribution of crossover components on meiotic chromosomes and revealing the possible enrichment in relation to the synaptonemal complex and that of chromosomal regions. Workflow 5 shows that volumetric measurements of FISH signals enable determining chromatin density (compaction) in different genomic regions. Finally, workflow 7 proposes an approach to measure the angles between chromosome and cell elongation axes and to investigate the relationship between cell division orientation and chromosomal positioning.

Image segmentation delivers a wealth of information related to signal intensity, distribution pattern (texture), shape, size and distance relationships between segmented objects [1]. Thus, images become associated with many variables and entry types, generating big data. Those can either be explored in a non-hypothesis-driven way using multidimensional data analysis (Bagheri et al., 2022) or in a hypothesis-driven manner following a careful choice of data for export. Even when exporting a selective number of image descriptors, the analysis of replicate image datasets, in different conditions (treatments or genotypes), labeled for multiple components, quickly generates a large numerical dataset. Versatile data visualization interfaces become handy at this stage. Here, we provided some examples among the numerous available solutions. We developed a customized Shiny-based (shiny.rstudio.com/) data visualization interface, DataViz, for processing (normalizing, filtering), exploring and plotting intensity, morphology and distance measurement data exported from segmented images. Normalization of intensity or distance measurements per image is important for considering variations that may arise between images during sample preparation, imaging or image acquisition [1,12]. The examples provided here propose different strategies depending on the image analysis question. Versatile data visualization greatly facilitates the explorative work, which in turn has the potential to seed discoveries, revealing

unexpected patterns or relationships and driving further analyses or experiments.

Although these workflows were developed to analyze nuclei and chromosome organization mostly in plant cells, these are conceptually applicable to nuclei of other species. An example is shown in workflow 4 with the analysis of nuclear bodies in mouse embryonic stem cells. In addition, these image analysis workflows are expected to inspire cell biologists beyond the study of the nucleus and its constituents. For instance, transposed at the cellular scale, workflow 1 or 4 could be applied to analyze the spatial distribution of vesicles or cytoplasmic bodies within a cell, using cell segmentation modules to create the initial surface object (see, for instance, but not exhaustive, references [66–68]).

Finally, while based on a particular (commercial) software piece, the concept of these workflows is expected to be transferable to other concurrent software offering similar image analysis tools (Supplementary File 8 – Table 1). One example is the 3D ImageJ Suite [8,10] popularized by the NEUBIAS COST action [8] which also offers a set of Fiji-based plugins for analyzing the spatial distribution of nuclear signals.

The increasing number of user-friendly platforms and the growing performance of segmentation algorithms greatly facilitate image analysis. Yet, this progress should not elude the need to reflect on the pertinence of the segmentation applied relative to the image features extracted by the process – and that will ultimately be interpreted in a biological context. Segmentation is influenced by the image quality, and specific metrics have been proposed to control for it [69]. In addition, when establishing a segmentation pipeline for the first time, several thresholds relative, for instance, to signal intensity, contrast and seed size must be adjusted that influence object detection. These thresholds influence the results in terms of the number, size, shape and texture of objects (discussed in [1,3]). In a semi-automated, user-guided segmentation such as proposed here, how to decide on a specific threshold or cutoff values can be difficult (of note, this type of decision is similar to those met in

bioinformatics analyses to select sequencing reads based on their quality, replication and cutoff levels). Threshold values must be justified with sufficient criteria to be reproduced and understood by peer users. Alternatively, and when image quality is relatively homogeneous in a dataset, it is possible to use values automatically proposed by the algorithm as those are usually derived from image-based statistical parameters. We address this issue and propose solutions for each workflow in their detailed description (supplemental files 1–7). Yet, the rapid emergence of machine-learning (ML) based segmentation algorithms is expected to ease the application of optimal segmentation parameters, although an initial investment is required to train the algorithm with ground-truth images (discussed in [1,12]). Eventually, and perhaps most importantly, the image analysis becomes only relevant when two or more biological conditions are compared. Sample preparation and image analysis done in the same conditions and by the same user, ideally in a blind analysis design, will average possible technical and cognitive biases throughout the datasets. This will, in turn, allow us to draw relevant conclusions relative to the type and the order of magnitude of changes correlated with a treatment, a genotype or cell type, for a given spatial pattern describing nuclear, chromatin or chromosome organization.

The compendium of workflows presented here, with its illustrations, training images and detailed guidelines, aims at inspiring experimentalists in the field of chromatin, chromosome and nucleus organization studies, with no or little expertise in image processing. This effort responds to the rapid development of microscopy imaging techniques and the needs of a wider community to have well documented and conceptually accessible image analysis tools [13]. Ultimately, this allows to exploit image data to an unprecedented level of analysis.

Note

1. <https://omero.bio.fsu.edu/webclient/userdata/?experimenter=-1> folder IDP 3008_Randall-Baroux2022

Acknowledgments

We acknowledge the microscopy imaging facilities of the University of Zürich (Jana Doehner, Urs Ziegler; ZMB), of the CEITEC at the Masaryk University (CELLIM, supported by the MEYS CR project no. LM2018129), and of the Auvergne Bioimaging platform (CLIC microscopy facility). The authors acknowledge the ‘INDEPTH’ COST Action CA16212 for funding of the Training School during which the workflows were developed, Peter Majer and Michael Mahler (Bitplane AG) for suggestions during the training school.

Disclosure statement

No potential conflict of interest was reported by the author(s).

Author contribution

The work was conceived by CB; carried out and conceptually refined by CB, RSR, DR, CJ, AN, KK, MK, MAA, VS, CT, IC, K, MP, IK, AS, SM, and SD; supervised by CB, CT, VS, ML, SH, RS, DS, and AP; and written by CB, RSR, CJ, AN, KK, MK, MAA, VS, CT, and IC. All authors read and revised the manuscript.

Funding

This work was funded by grants from the Swiss National Science Foundation [310030_185186 and IZCOZ0_198171 to CB, 310030_201268 to RS]; the Velux Stiftung (project 1107 to CB); the Ricola foundation (to CB); the ERC Grant Shuffle (Project ID: 669182) and Biotechnology and Biological Sciences Research Council (BB/T008636/1) to IC; the Deutsche Forschungsgemeinschaft to VS (Schu 762/11-1); the UZH-FUB Global Strategy and Partnerships Funding Scheme (grant to K); the Deutsche Akademische Austauschdienst Dienst (grant to K); the International Max Planck Research School for Biology and Computation (project IMPRS-BAC to CJ); the Czech Science Foundation (project 18-20134Sto MAL, 21-02929S to AP); the Operational Programme Research, Development and Education – “Project Internal Grant Agency of Masaryk University” (No. CZ.02.2.69/0.0/0.0/19_073/0016943 to MAL and MK) and ‘Plants as a tool for sustainable global development’ (No. CZ.02.1.01/0.0/0.0/16_019/0000827 to KK and AP); the German Federal Ministry of Education and Research (BMBF) in frame of the grant HERBY (FKZ-031B0188 to SH); the Purkyně fellowship to AP; the European Research Council (H2020 European Research Council ERC-AdG -787074-NucleolusChromatin to R.S.); CT, AS, SM and SD are supported by CNRS, INSERM, Université Clermont Auvergne (UCA), Agence Nationale de la Recherche (project grants 16-IDEX-0001 CAP 20-25 CIR1 and CIR3).

ORCID

Ricardo S Randall  <http://orcid.org/0000-0002-2778-519X>
 Claire Jourdain  <http://orcid.org/0000-0002-3568-580X>
 Anna Nowicka  <http://orcid.org/0000-0002-5762-3482>
 Kateřina Kaduchová  <http://orcid.org/0000-0001-9259-5942>
 Michaela Kubová  <http://orcid.org/0000-0003-3474-7324>
 Mohammad A. Ayoub  <http://orcid.org/0000-0001-9371-3277>
 Veit Schubert  <http://orcid.org/0000-0002-3072-0485>
 Christophe Tatout  <http://orcid.org/0000-0001-5215-2338>
 Isabelle Colas  <http://orcid.org/0000-0001-6980-9906>
 Kalyanikrishna  <http://orcid.org/0000-0002-8026-246X>
 Sophie Desset  <http://orcid.org/0000-0002-4897-4977>
 Sarah Mermet  <http://orcid.org/0000-0001-6839-3224>
 Aurélia Boulafloous-Stevens  <http://orcid.org/0000-0003-1378-2569>
 Ivona Kubalová  <http://orcid.org/0000-0002-5673-9715>
 Terezie Mandáková  <http://orcid.org/0000-0001-6485-0563>
 Stefan Heckmann  <http://orcid.org/0000-0002-0189-8428>
 Martin A. Lysak  <http://orcid.org/0000-0003-0318-4194>
 Martina Panatta  <http://orcid.org/0000-0002-8180-8380>
 Raffaella Santoro  <http://orcid.org/0000-0001-9894-2896>
 Daniel Schubert  <http://orcid.org/0000-0003-2390-0733>
 Ales Pecinka  <http://orcid.org/0000-0001-9277-1766>
 Célia Baroux  <http://orcid.org/0000-0001-6307-2229>

References

- [1] Bagheri N, Carpenter AE, Lundberg E, et al. The new era of quantitative cell imaging-challenges and opportunities. *Mol Cell*. 2022;82:241–247.
- [2] Jerkovic I, Cavalli G. Understanding 3D genome organization by multidisciplinary methods. *Nat Rev Mol Cell Biol*. 2021;22:511–528.
- [3] Dumur T, Duncan S, Graumann K, et al. Probing the 3D architecture of the plant nucleus with microscopy approaches: challenges and solutions. *Nucleus*. 2019;10(1):181–212.
- [4] Boettiger A, Murphy S. Advances in chromatin imaging at kilobase-scale resolution. *Trends Genet*. 2020;36:273–287.
- [5] Dar AS, Padha D. Medical image segmentation: a review of recent techniques, advancements and a comprehensive comparison. *Int J Comput Sci Eng*. 2019;7:114–124.
- [6] Lucas AM, Ryder PV, Li B, et al. Open-source deep-learning software for bioimage segmentation. *Mol Biol Cell*. 2021;32:823–829.
- [7] Shivanandan A, Radenovic A, Sbalzarini IF. MosaicIA: an ImageJ/Fiji plugin for spatial pattern and interaction analysis. *BMC Bioinformatics*. 2013;14:349.
- [8] Boudier T. Fiji 3D image suite. 2020. <https://imagej.net/media/plugins/3d-imagej-suite/neubias-3dsuite.pdf>
- [9] Boudier T, Andrey P. Spatial statistics 2D/3D. 2012. https://imagejdocu.list.lu/plugin/analysis/spatial_statistics_2d_3d/start
- [10] Ollion J, Cochenne J, Loll F, et al. TANGO: a generic tool for high-throughput 3D image analysis for studying nuclear organization. *Bioinformatics*. 2013;29:1840–1841.
- [11] Arpon J, Gaudin V, Andrey P. A method for testing random spatial models on nuclear object distributions. *Methods Mol Biol*. 2018;1675:493–507.
- [12] Caicedo JC, Cooper S, Heigwer F, et al. Data-analysis strategies for image-based cell profiling. *Nat Methods*. 2017;14:849–863.
- [13] Jamali N, Dobson ETA, Eliceiri KW, et al. BioImage Analysis Survey: community experiences and needs for the future. *Biological Imaging*. 2020;1:e4.
- [14] Tatout C, Mougeot G, Parry G, et al. The INDEPTH (Impact of nuclear domains on gene expression and plant traits) academy – a community resource for plant science. *J Exp Bot*. 2022;73:1926–1933.
- [15] van Driel R, Franz P. Nuclear architecture and genome functioning in plants and animals: what can we learn from both? *Exp Cell Res*. 2004;296:86–90.
- [16] Dong P, Tu X, Liang Z, et al. Plant and animal chromatin three-dimensional organization: similar structures but different functions. *J Exp Bot*. 2020;71:5119–5128.
- [17] Andrey P, Kiêu K, Kress C, et al. Statistical analysis of 3D images detects regular spatial distributions of centromeres and chromocenters in animal and plant nuclei. *PLoS Comput Biol*. 2010;6:e1000853.
- [18] Bishop J, Swan H, Valente F, et al. The plant nuclear envelope and its role in gene transcription. *Front Plant Sci*. 2021;12:674209.
- [19] Cremer M, Schmid VJ, Kraus F, et al. Initial high-resolution microscopic mapping of active and inactive regulatory sequences proves non-random 3D arrangements in chromatin domain clusters. *Epigenetics Chromatin*. 2017;10:39.
- [20] Girelli G, Custodio J, Kallas T, et al. GPSeq reveals the radial organization of chromatin in the cell nucleus. *Nat Biotechnol*. 2020;38:1184–1193.
- [21] Schubert V. RNA polymerase II forms transcription networks in rye and Arabidopsis nuclei and its amount increases with endopolyploidy. *Cytogenet Genome Res*. 2014;143:69–77.
- [22] Schubert V, Weissbart K. Abundance and distribution of RNA polymerase II in Arabidopsis interphase nuclei. *J Exp Bot*. 2015;66:1687–1698.
- [23] Ashenafi MS, Baroux C. Automated 3D gene position analysis using a customized imaris plugin: xTFISHInsideNucleus. *Methods Mol Biol*. 2018;1675:591–613.
- [24] Andrey P, Kieu K, Kress C, et al. Statistical analysis of 3D images detects regular spatial distributions of

- centromeres and chromocenters in animal and plant nuclei. *PLoS Comput Biol.* **2010**;6:e1000853.
- [25] Fransz P, De Jong JH, Lysak M, et al. Interphase chromosomes in *Arabidopsis* are organized as well defined chromocenters from which euchromatin loops emanate. *Proc Natl Acad Sci U S A.* **2002**;99:14584–14589.
- [26] Bucevicius J, Keller-Findeisen J, Gilat T, et al. Rhodamine-Hoechst positional isomers for highly efficient staining of heterochromatin. *Chem Sci.* **2019**;10:1962–1970.
- [27] Huff J. The Airyscan detector from ZEISS: confocal imaging with improved signal-to-noise ratio and super-resolution. *Nat Methods.* **2015**;12:i–ii.
- [28] Orr JN, Lewandowska D, Waugh R, et al. Chromosome synapsis and recombination in cereals. *Annu Plant Rev Online.* 1–26. doi:10.1002/9781119312994.apr0710.
- [29] Keeney S. Spo11 and the formation of DNA double-strand breaks in meiosis. *Genome Dyn Stab.* **2008**;2:81–123.
- [30] Bishop DK. RecA homologs Dmc1 and Rad51 interact to form multiple nuclear complexes prior to meiotic chromosome synapsis. *Cell.* **1994**;79:1081–1092.
- [31] Higgins JD, Perry RM, Barakate A, et al. Spatiotemporal asymmetry of the meiotic program underlies the predominantly distal distribution of meiotic crossovers in barley. *Plant Cell.* **2012**;24:4096–4109.
- [32] Barakate A, Higgins JD, Vivera S, et al. The synaptonemal complex protein ZYP1 is required for imposition of meiotic crossovers in barley. *Plant Cell.* **2014**;26:729–740.
- [33] Colas I, Barakate A, Macaulay M, et al. desynaptic5 carries a spontaneous semi-dominant mutation affecting Disrupted Meiotic cDNA 1 in barley. *J Exp Bot.* **2019**;70:2683–2698.
- [34] Serra H, Lambing C, Griffin CH, et al. Massive crossover elevation via combination of HEI10 and recq4a recq4b during *Arabidopsis* meiosis. *Proc Natl Acad Sci U S A.* **2018**;115:2437–2442.
- [35] Hesse S, Zelkowski M, Mikhailova EI, et al. Ultrastructure and dynamics of synaptonemal complex components during meiotic pairing and synapsis of standard (A) and Accessory (B) rye chromosomes. *Front Plant Sci.* **2019**;10:773.
- [36] De Muyt A, Zhang L, Piolot T, et al. E3 ligase Hei10: a multifaceted structure-based signaling molecule with roles within and beyond meiosis. *Genes Dev.* **2014**;28:1111–1123.
- [37] Matera AG, Izaguire-Sierra M, Praveen K, et al. Nuclear bodies: random aggregates of sticky proteins or crucibles of macromolecular assembly? *Dev Cell.* **2009**;17:639–647.
- [38] Stanek D, Fox AH. Nuclear bodies: news insights into structure and function. *Curr Opin Cell Biol.* **2017**;46:94–101.
- [39] Mao YS, Zhang B, Spector DL. Biogenesis and function of nuclear bodies. *Trends Genet.* **2011**;27:295–306.
- [40] Ali GS, Golovkin M, Reddy AS. Nuclear localization and in vivo dynamics of a plant-specific serine/arginine-rich protein. *Plant J.* **2003**;36:883–893.
- [41] Docquier S, Tillemans V, Deltour R, et al. Nuclear bodies and compartmentalization of pre-mRNA splicing factors in higher plants. *Chromosoma.* **2004**;112:255–266.
- [42] Reddy AS, Day IS, Gohring J, et al. Localization and dynamics of nuclear speckles in plants. *Plant Physiol.* **2012**;158:67–77.
- [43] Lorkovic ZJ, Hilscher J, Barta A. Use of fluorescent protein tags to study nuclear organization of the spliceosomal machinery in transiently transformed living plant cells. *Mol Biol Cell.* **2004**;15:3233–3243.
- [44] Tosolini M, Brochard V, Adenot P, et al. Contrasting epigenetic states of heterochromatin in the different types of mouse pluripotent stem cells. *Sci Rep.* **2018**;8:5776.
- [45] Gioacchini N, Peterson CL. Chromatin remodeling: a complex affair. *EMBO Rep.* **2017**;18:1673–1674.
- [46] Mikulski P, Hohenstatt ML, Farrona S, et al. The chromatin-associated protein PWO1 interacts with plant nuclear lamin-like components to regulate nuclear size. *Plant Cell.* **2019**;31:1141–1154.
- [47] Batty P, Gerlich DW. Mitotic chromosome mechanics: how cells segregate their genome. *Trends Cell Biol.* **2019**;29:717–726.
- [48] Beseda T, Capal P, Kubalova I, et al. Mitotic chromosome organization: general rules meet species-specific variability. *Comput Struct Biotechnol J.* **2020**;18:1311–1319.
- [49] Kubalová I, Câmara AS, Cápál P, et al. Helical metaphase chromatid coiling is conserved. *bioRxiv.* **2021**;2021:460607.
- [50] Weisshart K, Fuchs J, Schubert V. Structured illumination microscopy (SIM) and photoactivated localization microscopy (PALM) to analyze the abundance and distribution of RNA Polymerase II molecules on flow-sorted *Arabidopsis* nuclei. *Bio-protocol.* **2016**;6:e1725.
- [51] Bennett MD, Leitch IJ, Price HJ, et al. Comparisons with *Caenorhabditis* (approximately 100 Mb) and *Drosophila* (approximately 175 Mb) using flow cytometry show genome size in *Arabidopsis* to be approximately 157 Mb and thus approximately 25% larger than the *Arabidopsis* genome initiative estimate of approximately 125 Mb. *Ann Bot.* **2003**;91:547–557.
- [52] Mascher M, Gundlach H, Himmelbach A, et al. A chromosome conformation capture ordered sequence of the barley genome. *Nature.* **2017**;544:427–433.
- [53] Pecinka A, Schubert V, Meister A, et al. Chromosome territory arrangement and homologous pairing in nuclei of *Arabidopsis thaliana* are predominantly random except for NOR-bearing chromosomes. *Chromosoma.* **2004**;113:258–269.
- [54] Shan W, Kubova M, Mandakova T, et al. Nuclear organization in crucifer genomes: nucleolus-associated

- telomere clustering is not a universal interphase configuration in Brassicaceae. *Plant J.* **2021**;108:528–540.
- [55] Santos AP, Shaw P. Interphase chromosomes and the Rab1 configuration: does genome size matter? *J Microsc.* **2004**;214:201–206.
- [56] Nowicka A, Kovacik M, Tokarz B, et al. Dynamics of endoreduplication in developing barley seeds. *J Exp Bot.* **2021**;72:268–282.
- [57] Hudakova S, Michalek W, Presting GG, et al. Sequence organization of barley centromeres. *Nucleic Acids Res.* **2001**;29:5029–5035.
- [58] Richards EJ, Ausubel FM. Isolation of a higher eukaryotic telomere from *Arabidopsis thaliana*. *Cell.* **1988**;53:127–136.
- [59] Hurel A, Phillips D, Vrielynck N, et al. A cytological approach to studying meiotic recombination and chromosome dynamics in *Arabidopsis thaliana* male meiocytes in three dimensions. *Plant J.* **2018**;95:385–396.
- [60] Mandakova T, Lysak MA. Chromosome preparation for cytogenetic analyses in *Arabidopsis*. *Curr Protoc Plant Biol.* **2016**;1:43–51.
- [61] Mandakova T, Lysak MA. Painting of *Arabidopsis* chromosomes with chromosome-specific BAC clones. *Curr Protoc Plant Biol.* **2016**;1:359–371.
- [62] Kirschner GK, Stahl Y, Von Korff M, et al. Unique and conserved features of the barley root meristem. *Front Plant Sci.* **2017**;8:1240.
- [63] Van Norman JM. Asymmetry and cell polarity in root development. *Dev Biol.* **2016**;419:165–174.
- [64] Oud JL, Nanninga N. Cell shape, chromosome orientation and the position of the plane of division in *Vicia faba* root cortex cells. *J Cell Sci.* **1992**;103:847–855.
- [65] Donaldson L. Autofluorescence in plants. *Molecules.* **2020**;25:2393.
- [66] Mendocilla Sato E, Baroux C. Analysis of 3D cellular organization of fixed plant tissues using a user-guided platform for image segmentation. *Bio-protocol.* **2017**;7:e2355.
- [67] Ota R, Ide T, Michiue T. A rapid segmentation method of cell boundary for developing embryos using machine learning with a personal computer. *Dev Growth Differ.* **2021**;63(8):406–416.
- [68] Kesler B, Li G, Thiemicke A, et al. Automated cell boundary and 3D nuclear segmentation of cells in suspension. *Sci Rep.* **2019**;9:10237.
- [69] Bray MA, Fraser AN, Hasaka TP, et al. Workflow and metrics for image quality control in large-scale high-content screens. *J Biomol Screen.* **2012**;17:266–274.

Keywords or phrases:

Live-cell analysis, phenotypic screening, Artificial intelligence (AI), cell health, cytotoxicity, cell growth, cell cycle, mitochondrial membrane potential

Cell-based phenotypic screening with Incucyte® Live-Cell Analysis Systems

Gillian Lovell¹, Jasmine Trigg¹, John Rauch², Nicola Bevan¹

1. Sartorius UK, Royston, Hertfordshire

2. Sartorius NA, Ann Arbor, MI

Correspondence

Email: AskAScientist@sartorius.com

Introduction

Phenotypic screening – the measurement of a defined output in cells exposed to a large number of chemical compounds – is a vital tool in drug discovery, enabling scientists to rapidly identify potential drugs early in the discovery pipeline.¹ Live-cell imaging provides vastly more biological information than a single endpoint readout², since images reveal insight into growth and morphology changes of cells which are maintained within a physiologically relevant environment. Here we describe the application of Incucyte® Live-Cell Analysis Systems to derive insights into a library of 880 FDA-approved drugs by integrating data from label-free image analysis with quantification of fluorescent reporters.

Assay Principle

To perform the screening assay, A549 adenocarcinoma cells were seeded into 11 x 96-well microplates and once adhered, treated with a 1:1000 dilution of all compounds from the FDA-Approved Drugs Screening Library (Cayman Chemical #23538) supplied at 10 mM in DMSO (final concentration of all compounds 10 μ M). Microplates were placed into Incucyte® Live-Cell Analysis Systems where phase contrast and fluorescence images were acquired and analyzed using integrated software

To extract maximal information from each assay fluorescence readouts were multiplexed. In an Incucyte® SX5, A549 cells expressing the Incucyte® Cell Cycle Green/Orange reporter were combined with Incucyte® Annexin V NIR Dye; A549 cells expressing the nuclear marker Incucyte® Nuclight NIR Lentivirus were multiplexed with Incucyte® Caspase 3/7 Dye and Incucyte® Mitochondrial Membrane Potential (MMP) Dye. In an Incucyte® S3, A549 cells expressing the Incucyte® Kinase Akt Green/Red biosensor were used. In total, this screen was comprised of three runs wherein 11 x 96-well microplates of cells were treated with 80 test compounds per plate, and images were acquired every 2 hours for 4 days resulting in over 150,000 images.

Incucyte® Live-Cell Imaging

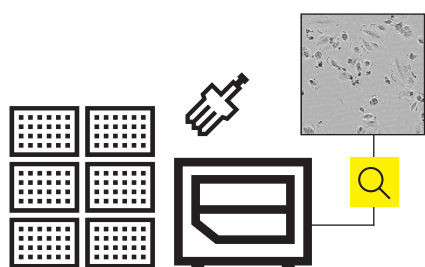
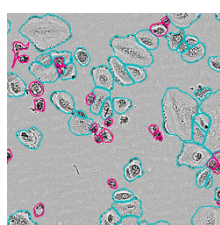
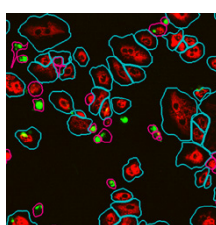


Image Analysis



Label-free



Fluorescence

Insight

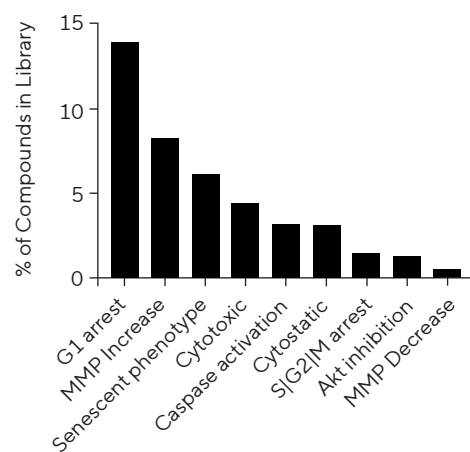


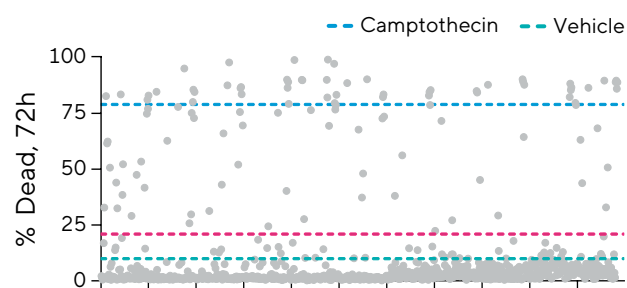
Figure 1: Phenotypic screening using Incucyte® Live-Cell Analysis Systems provides insight into compound mechanisms of action.

Data Analysis and Initial Hit Identification

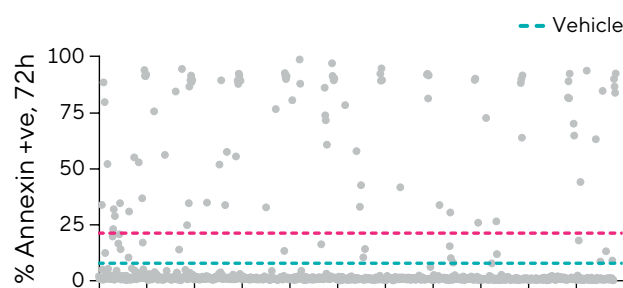
To achieve an overview of compound effects, an endpoint analysis was performed using each readout. Controls were included (vehicle, DMSO 0.1% and camptothecin, 10 μ M) to delineate the assay window and ensure assay robustness. Figure 2 displays scatter plots with each point representing a single concentration of each test compound with dashed lines indicating the mean values of the vehicle and appropriate controls. This visualization highlights the different ways in which drugs can affect cells – for example while a large number induce G1 arrest, many fewer are cytotoxic. Reporting multiple readouts can enable insight into the complexities of drug interactions with cells.

Appropriate time points were chosen based on the kinetic response of each readout. For example, time courses of % death showed maximal response between 48 and 72 hours while mitochondrial membrane and Akt kinase perturbation occurs within 12 hours. Cytotoxicity was quantified across all assay plates using Incucyte® AI Cell Health Analysis Software Module which segments cells and automatically performs label-free live|dead classification. Camptothecin was included as a positive control for cytotoxicity on every assay plate and induced an average of 79% cell death per image at 72 hours post treatment. Within the compound library, 39 out of 880 compounds induced greater than 50% cell death.

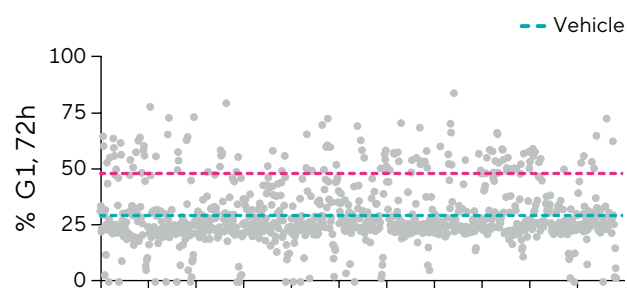
Cytotoxicity: AI Cell Health



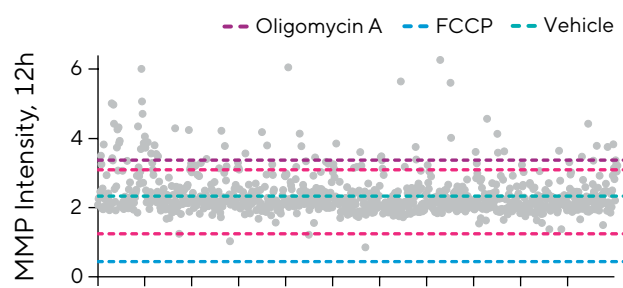
Apoptosis (Annexin V)



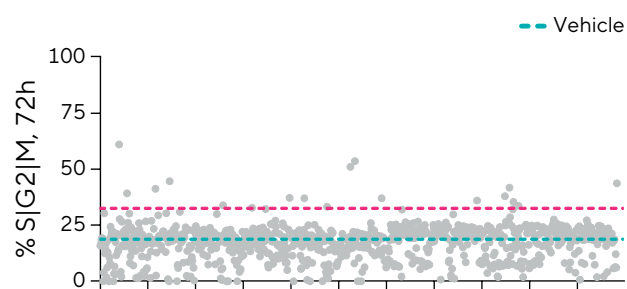
Cell Cycle Arrest (G1)



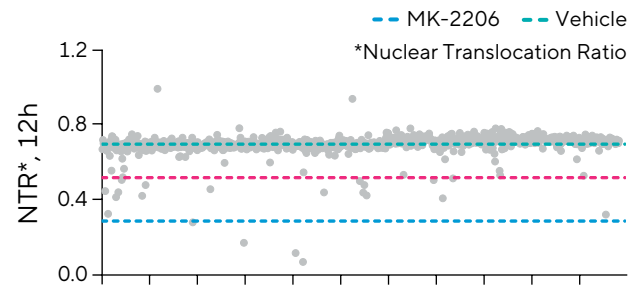
Mitochondrial Membrane Potential



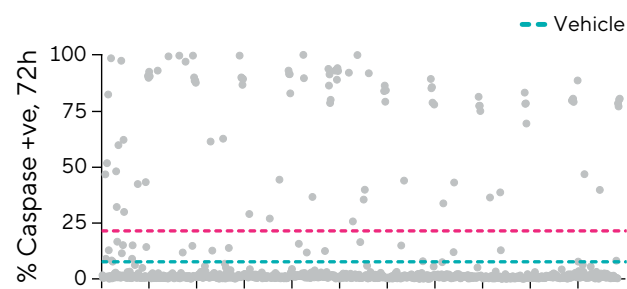
Cell Cycle Arrest (S|G2|M)



Akt Activity



Caspase Activating



Cell Enlargement >1800 μ m²

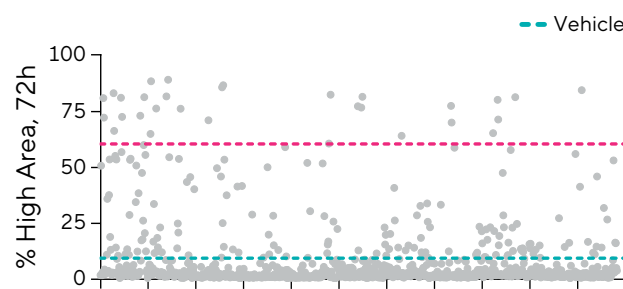


Figure 2: Scatter plots display endpoint analyses used to identify hits based on individual readouts at 72h. Teal line indicates the mean vehicle control values and magenta line denotes mean of vehicle ± 3 standard deviations. Control compounds are denoted in blue and purple.

Cells expressing the Incucyte® Cell Cycle reporter display green fluorescence in S|G2|M and orange fluorescence in G1 stage of the cell cycle. The percentage of cells in each stage were quantified by classifying the fluorescence within the live cell population only, since dead cells exit the cell cycle and can skew the data. Of the compounds within the library, 122 induced an increase in %G1 cells that exceeded the vehicle mean +3 standard deviations (~50% cells in G1) while only 13 induced a similar increase in %S|G2|M.

Mitochondrial stress was evaluated using the Incucyte® Mitochondrial Membrane Potential (MMP) Assay. Changes in MMP alter the fluorescence intensity with control compound Oligomycin A inducing hyperpolarization (increase in Orange Mean Intensity within the cell boundary), while control compound FCCP induces depolarization (decrease in Orange Mean Intensity). 73 compounds from the library induced hyperpolarization while only 3 induced significant depolarization.

Activity of the kinase Akt was measured using cells expressing the Incucyte® Kinase Akt reporter. Basic fluorescence segmentation was used to identify the nucleus (red fluorescence, nuclear-restricted) and the localization of Akt substrate (green fluorescence) which translocates from the cytoplasm to the nucleus upon inhibition of Akt. The overlapping fluorescence masks are used to automatically quantify a Nuclear Translocation Ratio. In total 40 compounds from the library reduced the Nuclear Translocation Ratio below the vehicle mean -3 standard deviations.

Cell Growth and Cytotoxicity

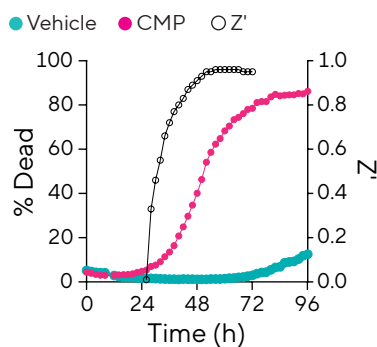
Positive control compound camptothecin induced cell death with the percentage of dead cells increasing from around 24 hours post treatment, reaching a plateau after 72 hours (Figure 3A). In negative control (vehicle) wells, a minimal level of death is observed until 72 hours when cells become overconfluent and begin to lose viability.

These controls were used to calculate Z' - a recognized measure of assay quality in which values >0.4 indicate robust results suitable for single-shot screening assays- and highlighted strong separation between positive and negative control values between 48 and 72 hours. Microplate views display percent dead cells vs time for every well and enable rapid, simple visualization of compound cytotoxicity. Figure 3B displays kinetic responses over 72 hours for all 80 test compounds on Plate 11 (gray, columns 2-11) and shows that 7 compounds on this plate induce cell death.

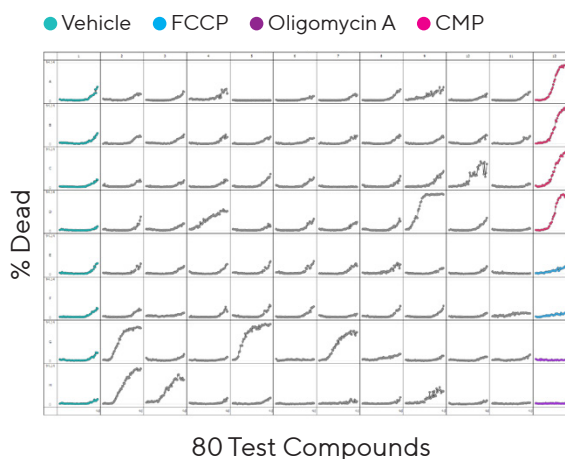
The compounds included in this screening assay possess a wide variety of mechanisms of action, and cellular response can be grouped into phenotypes by examining the correlation between cell growth and viability. Figure 3C displays the quantification of confluence (cell growth) and live cells (viability) at 3 days post-treatment with each point representing a single compound within the screen. Compounds which show results in the top right area of the plot (teal box) display high viability and high confluence, indicating that the cells grow normally and are unperturbed. Those compounds with results in the bottom left area of the plot (magenta box) display low viability and low confluence, indicating cytotoxic mechanisms of action. A cytostatic mechanism is indicated in compounds which sit in the top middle area since the viability of cells is high - meaning the compound has not induced cell death - while the confluence is distinctly lower than the non-perturbing compounds - meaning that the cell growth has been inhibited.

To examine the efficacy of the most potent cytotoxic compounds, a cell death assay was performed in a 384-well microplate using concentration ranges of camptothecin and the 11 compounds with highest % death at 72 hours. Figure 4A displays the label-free % Dead cells vs time for each concentration range (1 nM - 10 μ M; 1:3 serial dilution) and provides an overview of drug efficacy. While concentration dependence is observed for many of the compounds, both Panobinostat and Bortezomib induced a high level of cell death even at the lowest concentration of 1 nM.

A. % Dead Cells and Z' vs Time



B. % Dead Cells vs Time (All Cell Health)



C. Live Cells vs Confluence

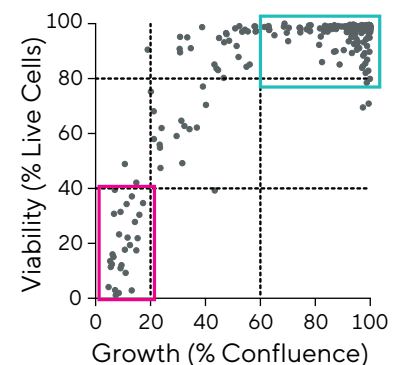
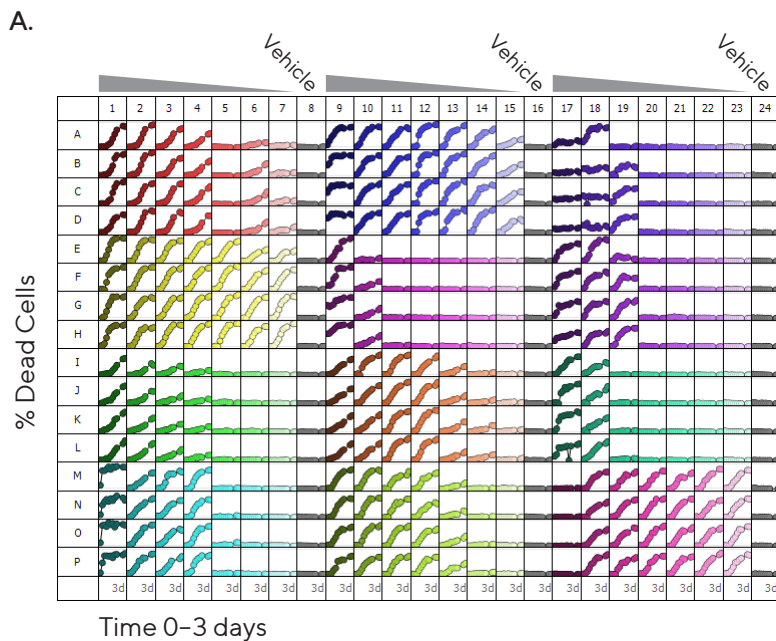


Figure 3: Data patterns indicate compound effect on cell growth and viability. Time course (A) displays % dead cells for vehicle and camptothecin; Z' value reaches a maximal value between 48 and 72h. Plate view (B) shows an overview of % dead cells over time for all wells of Plate 11. Scatter plot (C) shows correlation between cell growth and viability at 72h.



B.

Compound	Target	LogEC ₅₀
Camptothecin	Topoisomerase I	-7.1
Topotecan	Topoisomerase I	-5.7
Daunorubicin	Topoisomerase II	-6.8
Mitoxantrone	Topoisomerase II	-7.0
Idarubicin	Topoisomerase II	-7.9
Ceritinib	Kinase-ALK	-6.1
Vandetanib	Kinase-multiple	-5.3
LY2835219	Kinase-CDK 4/6	-6.0
Afatinib	Kinase-ErbB family	-5.7
MLN9708	20s Proteasome	-6.8
Bortezomib	20s Proteasome	N/C
Panobinostat	Histone deacetylase	N/C

C.

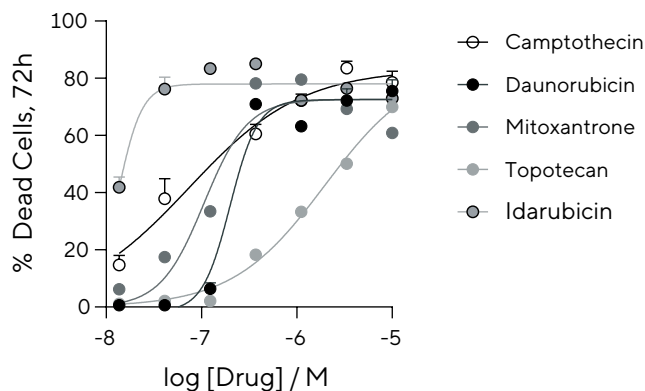


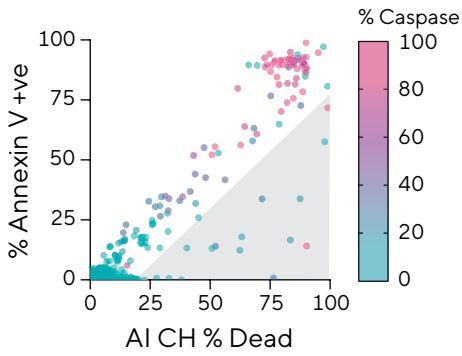
Figure 4: Efficacy of the 11 most toxic compounds is determined using Incucyte® AI Cell Health Analysis. Plate view displays % Dead cells versus time (A), and calculated compound efficacy was calculated (B). Concentration response curves are shown for topoisomerase I and II inhibitors (C).

Log EC₅₀ values for each tested compound are shown in Table 4B along with the mechanisms of action which included topoisomerase inhibitors, kinase inhibitors, and 20s Proteasome inhibitors. Figure 4C overlays the concentration response curves of the topoisomerase I and II inhibitors which reveals that the most potent is Idarubicin, and the least potent is Topotecan.

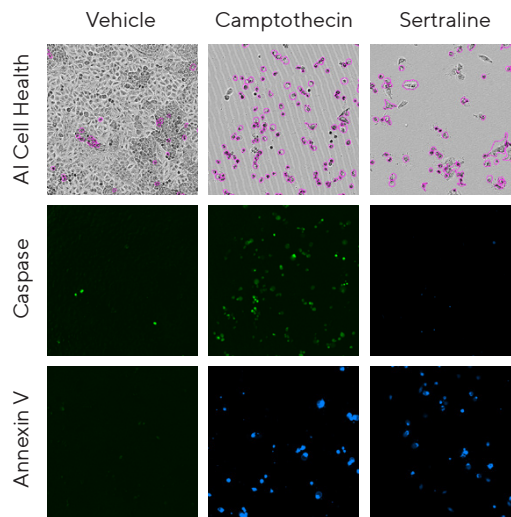
Cell death can occur via several mechanisms including necrosis and apoptosis – and within these are sub-types such as caspase-dependent versus caspase-independent apoptosis.³ To elicit more information on these mechanisms of cell death we included Incucyte® Annexin V Dye (high fluorescence indicates apoptosis) and Incucyte® Caspase 3/7 Dye (high fluorescence indicates caspase-dependent apoptosis). Figure 5A displays the correlation between total cell death (x axis, AI CH % Dead), apoptosis (y axis, % Annexin V positive) and caspase dependence (colour scale from teal to magenta, % Caspase positive). The scatter plot shows

a high correlation between total cell death and Annexin V ($R^2 = 0.95$) with only 2 % of compounds diverging from this relationship (17 out of 880 compounds). Although many apoptotic compounds are caspase-positive, Sertraline appears to act via caspase-independent pathways. Images (5B) and bar graph (5C) show quantification of using Incucyte® AI Cell Health (top row), Incucyte®Caspase 3/7 Dye (middle row) and Incucyte®Annexin V Dye (bottom row) response at 3 days post treatment. Untreated cells show high confluence with a small number of dead cells within the image, and low fluorescence response from both Incucyte® Caspase 3/7 and Annexin V Dyes. Camptothecin, a topoisomerase II inhibitor, shows a high level of cell death across all readouts indicating caspase-dependent apoptosis. Sertraline induces apoptotic cell death as indicated by AI Cell Health analysis and Incucyte® Annexin V response. However, within the dead cells the Incucyte® Caspase 3/7 intensity was low, indicating a caspase-independent apoptotic pathway.

A. Cell Death Mechanisms



B. Fluorescent Apoptosis Reagents



C. Quantification of Reagent Response

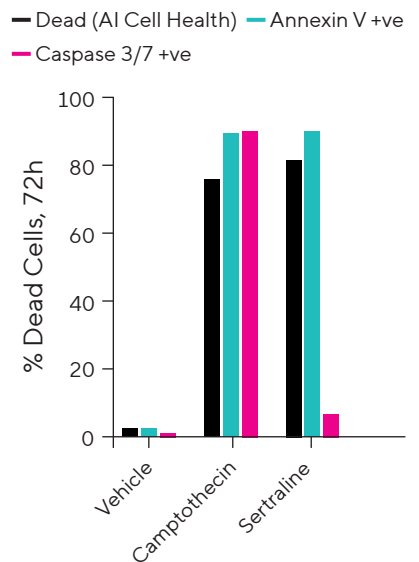


Figure 5: Cell death mechanisms can be elucidated by combining label-free analysis with fluorescence reagents. Annexin V positive and Caspase 3/7 positive cells were identified by performing fluorescence classification. Scatter plot (A) correlates (AI Cell Health % Dead) and apoptosis (% Annexin V positive) and colour scale highlights caspase activating compounds (% Caspase 3/7 positive). Images (B) display AI Cell Health dead cell classification (magenta outline, top row), caspase 3/7 activity (green fluorescence, middle) and Annexin V binding (Near IR fluorescence, bottom row). Bar graph (C) indicates quantification of these responses at 72h.

Cell Cycle Arrest

To explore the effect of compounds on cell cycle progression cells expressing the Incucyte® Cell Cycle Lentivirus were used. For quantification, an initial AI Cell Health analysis was performed and subsequently the live cell population was classified according to green and orange fluorescence intensity to identify cells in S|G2|M and G1 respectively. By excluding dead cells from this analysis the data is focused solely on live cells which are still within the cycle.

The endpoint analysis in Figure 2 shows that while numerous compounds arrest the cycle in G1, very few arrest in S|G2|M. Further examination of the kinetic response provides additional insight into individual compound effects. Figure 6 shows the cells in G1 (orange) and S|G2|M (green) for untreated (vehicle) cells, as well as cells in the presence of Mycophenolic acid or Flumazenil.

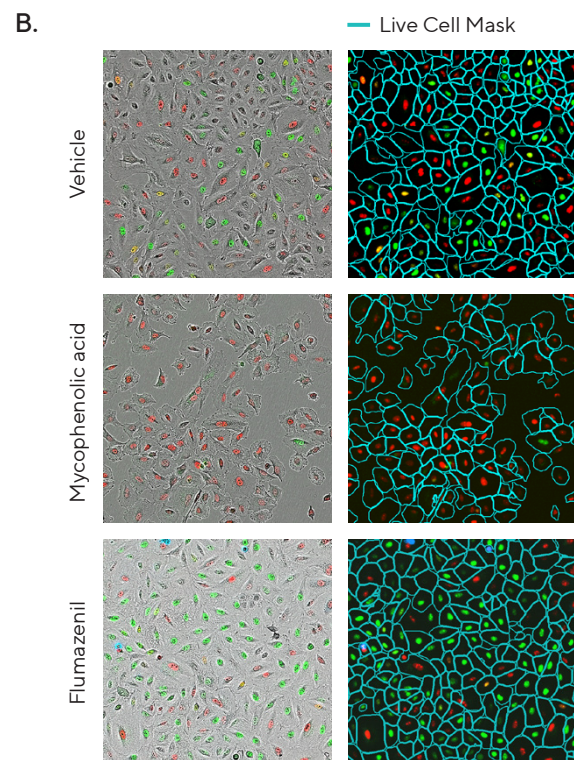
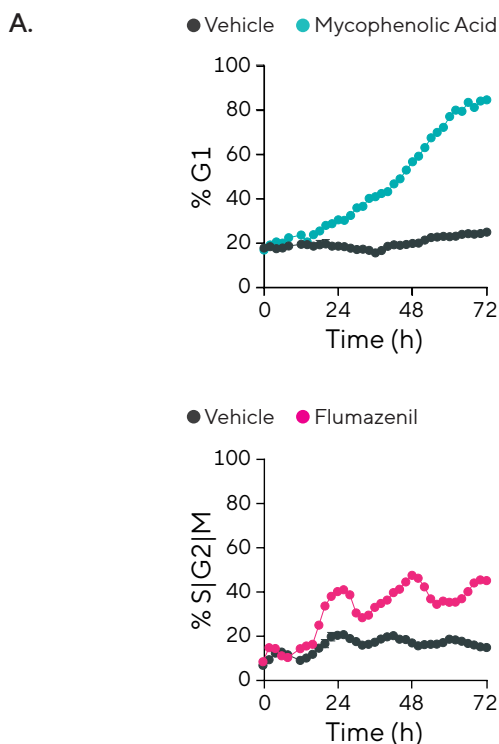


Figure 6: Cell cycle arrest is induced by a subset of compounds. Time courses (A) show the effect of Mycophenolic acid on %G1 (top) and that of Flumazenil on %S|G2|M (bottom). Images (B) show healthy cell morphology in phase contrast and fluorescence within the live cell population (teal segmentation).

Mycophenolic acid inhibits nucleotide synthesis (occurring in S phase), causing the cells to accumulate in G1. Figure 6A shows that in the presence of mycophenolic acid, the % G1 cells (orange) increases between 24 and 72 hours. Flumazenil is an antagonist of GABA_A receptors which lie upstream of several signaling pathways relating to cell growth. Figure 6A demonstrates that in the presence of Flumazenil an increase in the % S|G2|M cells is observed. Unlike Mycophenolic acid which induces a sustained increase over time in % G1, the presence of flumazenil induces an elevated % S|G2|M population which oscillates over time. This oscillation is observed when cells are treated with compounds which elongate mitosis and cause the cells to divide almost synchronously, creating peaks and troughs in the cell cycle populations.

Mitochondrial Membrane Potential

Mitochondrial stress is an early indicator of cell perturbation⁴, therefore the Incucyte® MMP Orange Dye was used to measure the effect of the compounds on mitochondrial membrane potential. The time course in Figure 7A quantifies MMP intensity within all segmented cells over time and shows that control compounds FCCP and Oligomycin A induce membrane depolarization and hyperpolarization, respectively. Cefdinir – a cephalosporin-based antibiotic – is shown to induce rapid hyperpolarization to a greater extent than Oligomycin A. Busulfan – a DNA alkylating agent – causes membrane depolarization almost as strongly as FCCP however the kinetic plot indicates that the depolarization process occurs more slowly.

Images (Figure 7B) show the fluorescence within the cell boundaries at 12 hours post-treatment with teal mask indicating live cells and magenta indicating dead cells. Depolarization results in loss of fluorescence intensity while hyperpolarization yields an increase in fluorescence intensity relative to vehicle, with little change in cell morphology in both cases. At this early timepoint (12h) minimal cell death is observed, and the scatter plot (Figure 7C) reveals little correlation between mitochondrial membrane polarization at 12 hours and eventual cell death at 72 hours.

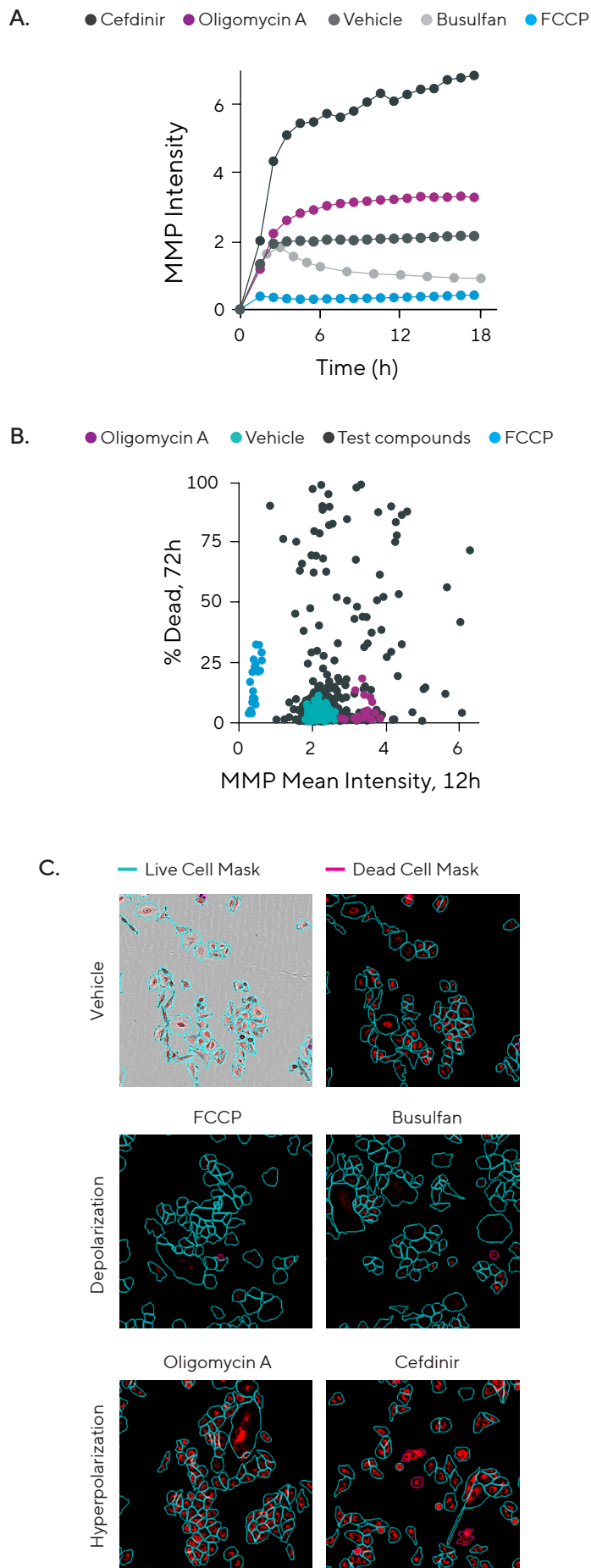


Figure 7: Perturbance of cellular mitochondrial membrane potential (MMP). Time course of MMP intensity (A) highlights depolarization (loss of intensity relative to vehicle) and hyperpolarization (increased intensity relative to vehicle). Images (B) show fluorescence within the cell boundaries at 12h. Scatter plot (C) correlates MMP at 12h with cell death at 72h.

Akt Kinase Inhibition

Kinase signaling is a critical regulator of cell proliferation, metabolism, and apoptosis.⁵ To identify potential kinase inhibitors within the compound library, cells expressing the Incucyte® Kinase Akt biosensor were used and kinase activity was quantified by measuring the nuclear localization of the fluorescent Akt substrate (Nuclear Translocation Ratio, NTR).

Cells with inhibited Akt activity display a reduced NTR value and the initial hit scatter plot in Figure 2 shows that 20 out of 880 total compounds decrease the NTR beyond 3 standard deviations below the mean vehicle value. However, cell morphology analysis reveals that some of these compounds induce cell rounding, meaning that the localization of the fluorescent Akt substrate between the nucleus and cytoplasm cannot be robustly determined. Cell rounding forces all the green fluorescence to overlap with the nucleus (red fluorescence). To identify Akt inhibitors more accurately the NTR value was plotted against cell eccentricity – a measure of cell elongation which decreases as cells become rounded.

Figure 8A shows a correlation between eccentricity and NTR (black diagonal line) of cells treated with vehicle or test compounds; a separate control assay was performed using specific Akt inhibitor MK2206 and the result is included in blue. Compounds which induce a decreased NTR without rounding (gray shaded area) are “true” hits since the fluorescence localization can be accurately measured.

Figure 8B displays an example of true Akt inhibition (AZD 9291) and cell rounding (Auranofin). AZD 9291 treatment causes the green fluorescent Akt substrate to localize within the nucleus (indicated by the red outline) and the NTR is reduced, however the cells have a similar eccentricity value to vehicle. Auranofin treated cells experience a reduction in NTR however since the eccentricity also drops and cells visibly round up, this compound is discarded as a hit.

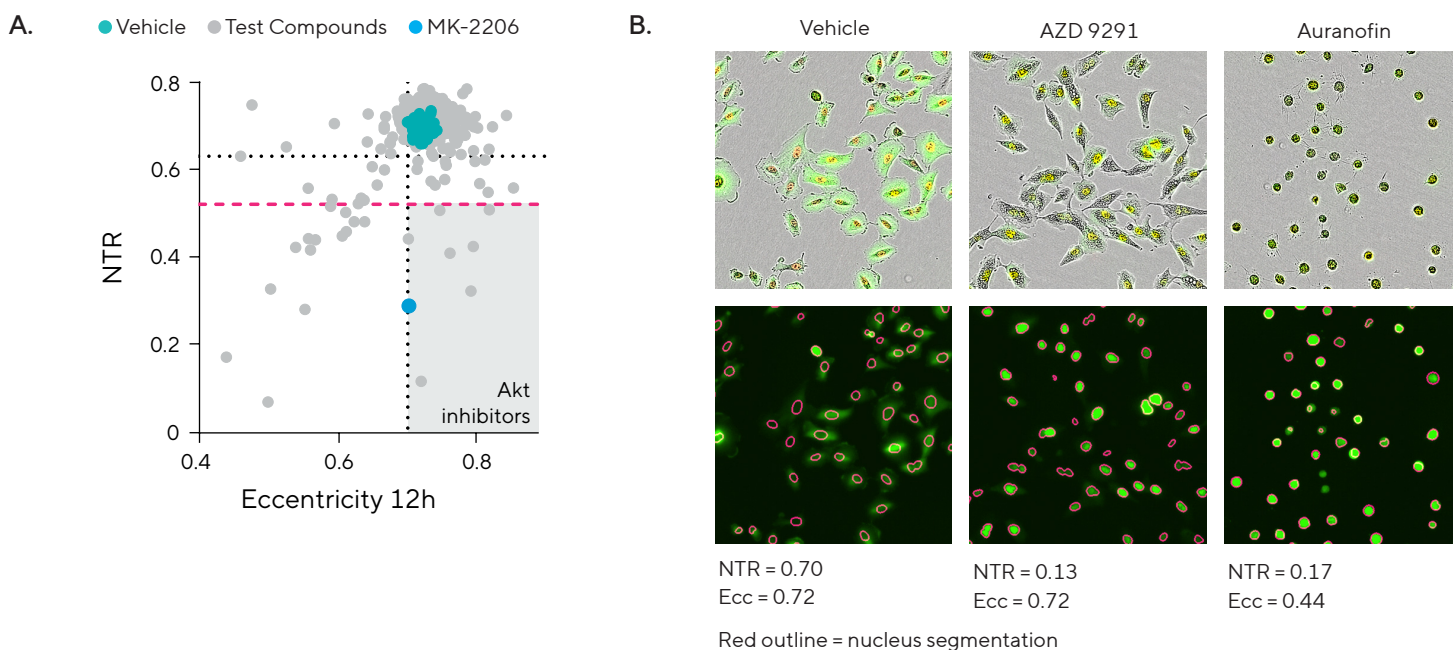


Figure 8: Inhibition of Akt kinase activity. Scatter plot (A) relating Nuclear Translocation Ratio (NTR) to eccentricity (Ecc) indicates positive hits for Akt inhibitors. Images (B) compare true inhibition by AZD 9291 to false positive Auranofin.

Summary and Conclusion

Incucyte® Live-Cell Analysis Systems were used to perform phenotypic screening of an 880-compound library. An overview of compound activity was obtained using endpoint analysis of images capturing multiple readouts including label-free cell death analysis, fluorescent apoptosis and mitochondrial membrane potential reagents, and fluorescent reporters measuring cell cycle stage and Akt kinase activity.

Kinetic information gained by repeated image acquisition within a physiologically relevant environment added insight into the dynamic changes which are often overlooked using end-point analysis alone. Additionally, by combining multiple readouts compound mechanisms were elucidated and misleading results were discarded. These data are reinforced with cell images throughout the time course that demonstrate any morphological changes yielding highly robust and insightful data.

References

1. Opportunities and challenges in phenotypic drug discovery: an industry perspective. Moffat, John G, et al. 2017, *Nature Reviews Drug Discovery*, Vol. 16, pp. 531 - 543.
2. Live-cell imaging: The cell's perspective. Cole, Richard. 5, 2014, *Cell Adhesion and Migration*, Vol. 8, pp. 452 - 459.
3. Cell Death in the Origin and Treatment of Cancer. Strasser, Andreas and Vaux, David L. 2020, *Molecular Cell*, Vol. 78, pp. 1045 - 1054.
4. Systemic effects of mitochondrial stress. Bar-Ziv, Raz, Bolas, Theodore and Dillin, Andrew. 6, 2020, *EMBO Reports*, Vol. 21, p. e50094.
5. AKT as a Therapeutic Target for Cancer. Song, Mengqui, et al. 6, 2019, *Cancer Research*, Vol. 79, pp. 1019 - 1031.

North America

Sartorius Corporation
300 West Morgan Road
Ann Arbor, Michigan 48108
USA
Phone +1 734 769 1600
Email: orders.US07@sartorius.com

Europe

Sartorius UK Ltd.
Longmead Business Centre
Blenheim Road
Epsom
Surrey, KT19 9QQ
United Kingdom
Phone +44 1763 227400
Email: euorders.UK03@sartorius.com

Asia Pacific

Sartorius Japan K.K.
4th Floor, Daiwa Shinagawa North Bldg.
1-8-11, Kita-Shinagawa 1-chome
Shinagawa-Ku
Tokyo 140-0001
Japan
Phone +81 3 6478 5202
Email: orders.US07@sartorius.com

 **For further information, visit**
www.sartorius.com



Contact us

Editorial Department

Senior Editor

Tristan Free

Tristan.Free@tandf.co.uk

Business Development and Support

Commercial Director

Evelina Rubio Hakansson

Evelina.RubioHakansson@tandf.co.uk

This supplement is brought to you by *BioTechniques* in association with

SARTORIUS